# LARGE DEFORMATION BEHAVIOR OF CAST A356 ALUMINUM ALLOY UNDER UNIAXIAL TENSION, COMPRESSION AND V-BENDING

# LARGE DEFORMATION BEHAVIOR OF CAST A356 ALUMINUM ALLOY UNDER UNIAXIAL TENSION, COMPRESSION AND V-BENDING

By

MAHMOUD M. MARZOUK, B.Sc.

A Thesis

Submitted to the School of Graduate Studies

in Partial Fulfillment of the Requirements

for the Degree

Master of Applied Sciences

McMaster University

MASTER OF APPLIED SCIENCE (2012) McMaster University

Mechanical Engineering Department Hamilton, Ontario

TITLE Large Deformation Behavior of Cast A356 Aluminum Alloy under Uniaxial Tension, Compression and V-Bending

AUTHOR Mahmoud M. Marzouk, B.Sc. (Cairo University, Egypt)

SUPERVISORS Dr. Mukesh K. Jain

Dr. Sumanth Shankar

NUMBER OF PAGES (155, xxii)

# Abstract

This work is an experimental approach to understand the effect of the microstructure on large strain deformation behavior of A356 alloy (with various additions of titanium and strontium) under tensile, compressive and V-bend loading conditions. The studies were carried out on unmodified and Sr-modified A356 Al alloy, where Sr was added to refine the morphology of the eutectic Si phase particles. The two variants were then used to study the effect of size and shape of inclusions within the material on the deformation behavior under uniaxial tension, compression and V-bending conditions. The alloy with a modified and refined eutectic Si phase particles showed significant improvement in ductility and bendability, whereas the differences in compression were not appreciable. In addition to Sr addition, Ti was also added as a grain refiner to the alloys at three different levels to obtain microstructures with different grain sizes. The results in the form of full field strain maps show that the larger grained alloy exhibits extensive strain inhomogeneity whereas the grain refined alloy shows a more homogenous loading pattern.

## Acknowledgements

Special thanks are due to both of my supervisors, Dr. Mukesh Jain and Dr. Sumanth Shankar. I sincerely appreciate their continuous guidance, patience and support throughout the preparation of this dissertation.

Also, I would like to thank Dr. Mike Bruhis for his valuable and much appreciated experimental work insights and guidance. Thanks are also due to Dr. Xiaochun Zeng for his help in the preparation of the cast alloy used for the experimental work.

I would like to thank the Mechanical Engineering machine shop technicians, Ron Lodewyks, Jim McLaren, JP Talon and Mark MacKenzie, for all their help in specimen preparation and machining. I would like to thank Ed McCaffery, Doug Culley, Steve Koprich and Chris Butcher for their help, guidance and insights with metallography and microscopy.

Thanks are also due to all my colleagues in the Metal Forming Laboratory research group, Ganesh Govindasamy, Hadi Noori and Dhanashree Aole, for several valuable discussions and insightful suggestions.

I would also like to thank the Light Metal Casting Research Centre research group individuals, Manickaraj Jeyakumar and Abbas khalaf, for their occasional assistance with the lab facilties.

At the end, I would like to thank my parents for their understanding, patience and continuous support throughout my work at McMaster University.

# Table of Contents

# List of Figures

# List of Tables

# Chapter 1 Introduction

Significant attention is being given to aluminum alloys in the automotive manufacturing sector. The increasing need for vehicle weight reduction to lower fuel consumption and better emission standards are the main driving forces of this trend. Aluminum alloys exhibit higher strength to weight ratio compared to many ferrous and non-ferrous alloys, great castability, good formability and are extensively recycled in practice. The work presented in this thesis focuses on the commercially important A356 Al cast alloy.

## 1.1 A356 Aluminum Cast Alloy Background

A356 aluminum cast alloy is one of the derivatives of the 3xx.x class of aluminum alloy, where the 3xx.x is from the family of Al-Si-Mg casting alloys. The A356 is one of the most versatile aluminum alloys; this alloy is extensively used in the automotive and aerospace sectors. The A356 castings offer an appealing strength to weight ratio. In addition, the great castabilitiy, good weldability and pressure tightness are other attributes that give the A356 cast alloy a vast array of industrial and commercial applications. The A356 alloy also has the benefit of being heat treatable, facilitating the control of the mechanical properties of the alloy (for example, strength and ductility). Typical applications of the A356 cast alloy is automotive transmission casings, aircraft pump parts, water cooled cylinder blocks, aircraft structures, nuclear energy installations, etc. Figure 1-1 shows commercial products manufactured used A356 cast alloy, engine cylinder head, water pump, alternator motor cases and vehicle manual transmission casing.

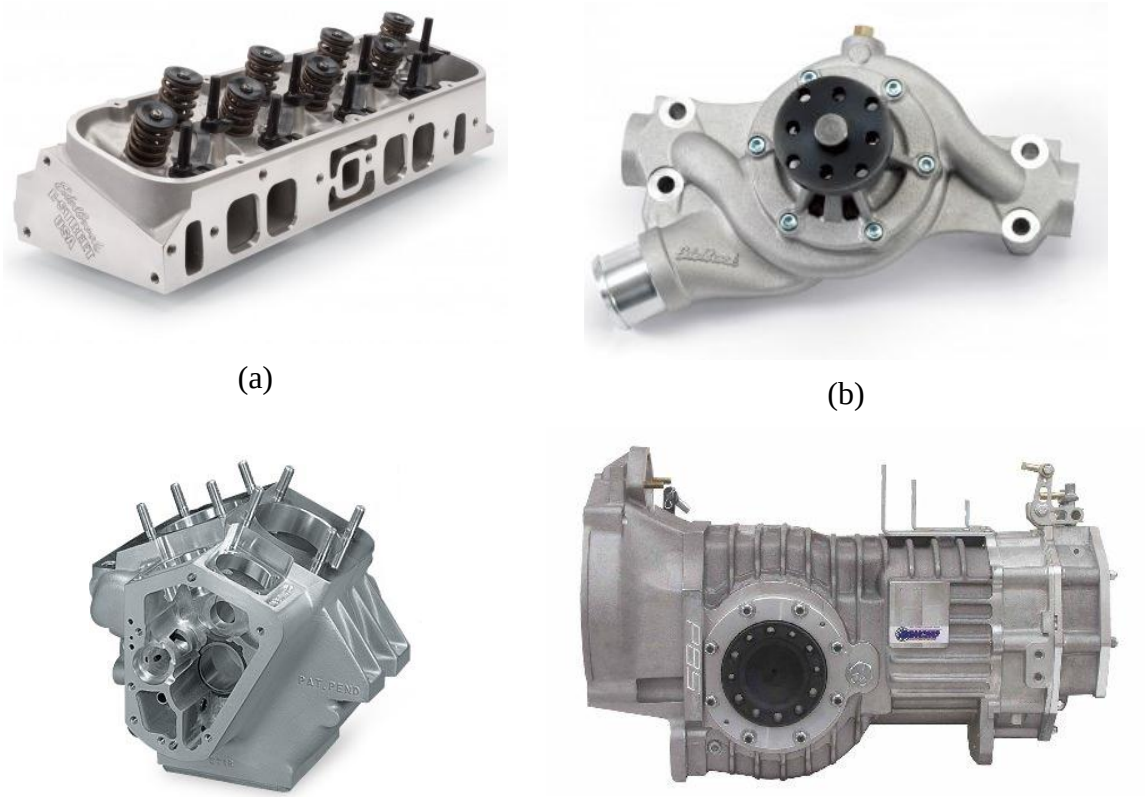

(a) (b)

(c) (d)

Figure 1-1. Typical A356 aluminum cast alloy commercial products and applications [1], [2], [3].

The A356 has been extensively studied in the past. Therefore, a review of the literature is presented first. The chapter is arranged as follows.

- A356 cast alloy – role of different constituent elements on the heat treatment, microstructure and deformation characteristics (section 1.1).
- Strain measurement techniques for analyzing deformation inhomogeneity in the microstructure (section 1.2).
- Role of the microstructure in strain localization and damage development during deformation (section 1.3).

### 1.1.1 Overview

As mentioned earlier, alloy A356 is from the Al-Si-Mg family. The alloy typically consists of aluminum rich dendritic cells, silicon particles in the interdendritic regions, porosity and minor intermetallic phases [4]. Table 1-1 shows the typical wt% range of different alloying elements that are typically used for the alloy.

Table 1-1. Composition of A356 aluminum casting alloys according Aluminum Association designation. [5] [6] [7] [8]

| Si | Fe | Cu | Mn | Mg | Zn | Ti | Al |
|---|---|---|---|---|---|---|---|
| 6.5-7.5 | 0.0-0.20 | 0.1-0.20 | 0.05-0.10 | 0.25-0.45 | 0.05-0.10 | 0.0-0.20 | Bal. |

Table 1-2. Typical mechanical properties of cast A356-T6 aluminum alloys. [5]

| Ultimate tensile strength (MPa) | 0.2% offset yield Strength (MPa) | Elongation in 50 mm, % |
|---|---|---|
| 262 | 193 | 5 |

### 1.1.2 Role of Constituents

- Silicon

Figure 1-2 shows the Al-Si phase diagram, where the eutectic point of the alloy is at 12.2 wt% Si at $577^0$C. The A356 cast alloy is a hypoeutectic alloy with a 6.5-7.5wt% Si. The addition of Si to aluminum alloys has various casting benefits without adding to porosity [9]. Si tremendously alters the cast fluidity improving the feeding and die filling characteristics, and enhances the hot tear resistance [5] [10] (see Figure 1-3 (a)). Si enhances both, macro and micro-hardness values (see Figure 1-3 (b) and (c)). The increase in the macro-hardness is due to the increase in the solidification cooling rate. The increase in micro-hardness values is due to the existence of the $Mg_2Si$, a phase that forms in the Al matrix during heat treating (i.e., during artificial aging and incubation).

On the other hand, Si has an adverse effect on the impact toughness of the material (see Figure 1-3 (d)).

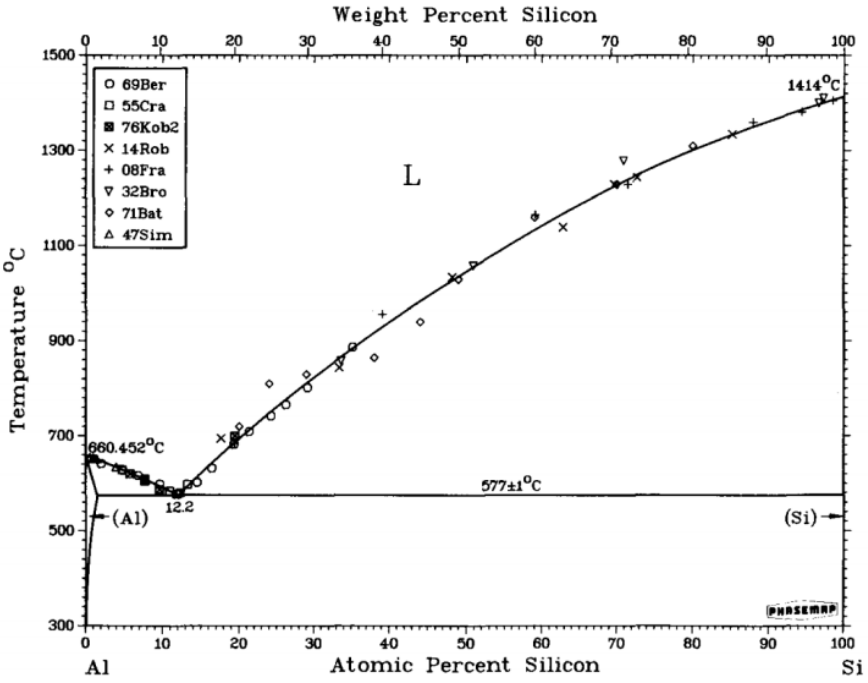


Figure 1-2. Al-Si binary phase diagram [11].

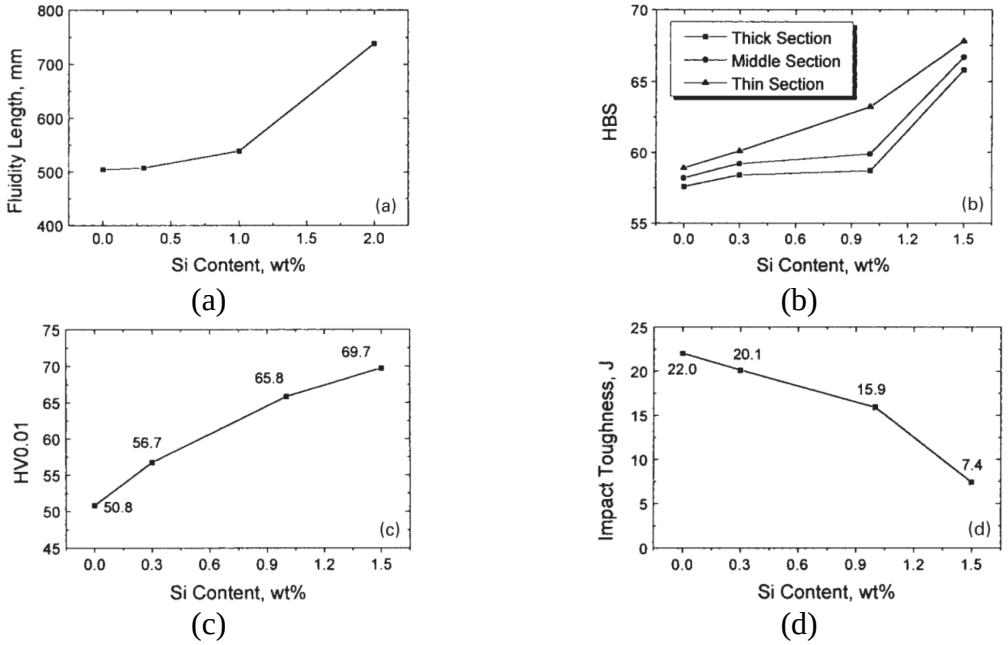


Figure 1-3. Effect of Si on (a) fluidity of the melt, (b) Brinell hardness number (HBS), (c) Vickers Pyramid Number (HV), and (d) impact toughness [10].

- Titanium

The main contribution of Ti addition to the aluminum alloy constituents is the refinement of the primary Al phase, subsequently refining the grain structure [12] [13] [14] by initiating copious nucleation sites in the Al phase at the liquidus temperature. Grain refinement leads to the formation of a wide-spread equiaxed grain structure with a finer average grain size [14]. Often boron is combined with Ti in minimal amounts to enhance the grain refining effect. Figure 1-4 shows that the effect of the grain refiners Ti and B soon saturates at around 0.045 Ti wt%, and further addition of the refiner becomes redundant beyond this amount. The effect Ti on other microstructure aspects such as porosity, dendritic structure and second phase particles has not been reported.

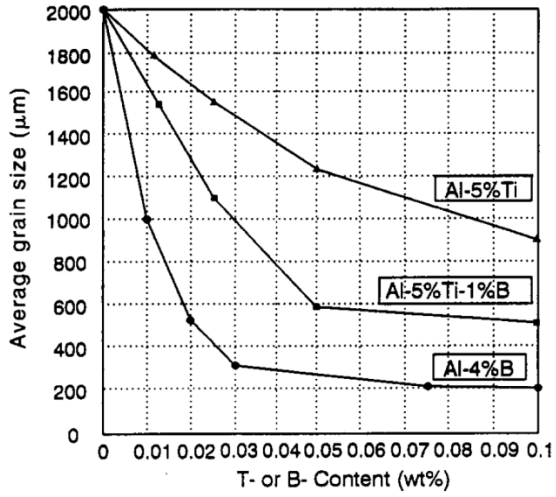


Figure 1-4. Grain refinement of A356 alloy with Al-Ti, Al-5Ti-B and Al-B master alloys [15].

- Strontium

First application of Sr to improve the mechanical properties dates back to 1921 where Pacz [16] added impurities to the alloy such as strontium fluoride and found that the mechanical properties were extensively enhanced. Small additions of Sr (as small as 50-

200 ppm) modify the morphology of the eutectic Si phase particles from flaky eutectic Si phase particles to a more fibrous form of particles [17]. The change of the morphology of the second phase particles reduces the stress concentration consequently enhancing the mechanical properties. Figure 1-5 and Figure 1-6 show the difference between the unmodified and Sr-modified forms of A356, respectively in as-cast and heat treated conditions. Sr has also shown to contribute to the increase in porosity content within the cast due to reasons such as change in the viscosity and surface tension of the solidifying liquid. This results in increased nucleation of porosity in the interdendritic region during solidification as shown by the work done by Emadi et al. [18]. Also the addition of Sr to the alloy results in an increased levels of hydrogen dissolved in the alloy when compared to the unmodified alloy and this leads to increased size of average porosity [19].

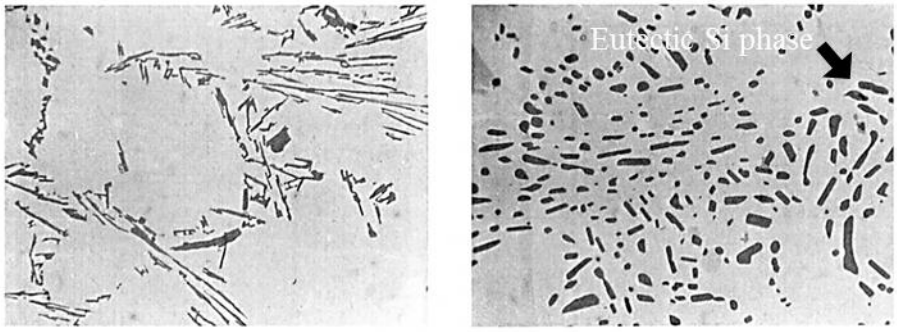


(a) (b)

Figure 1-5. Unmodified A356 (a) as-cast and (b) heat treated conditions [8].

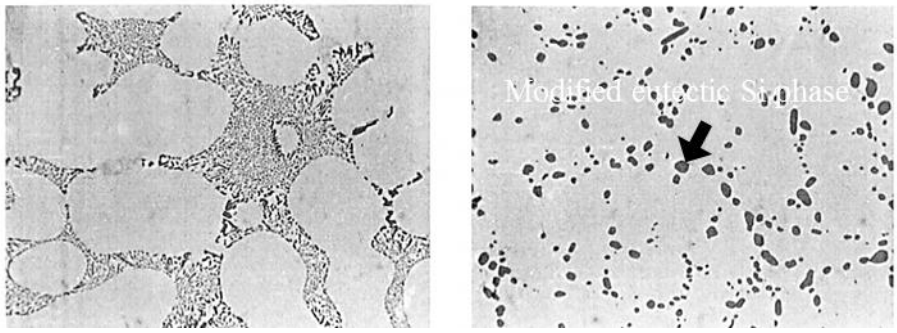


(a) (b)

Figure 1-6. Sr-modified A356 (a) as-cast and (b) heat treated conditions [8].

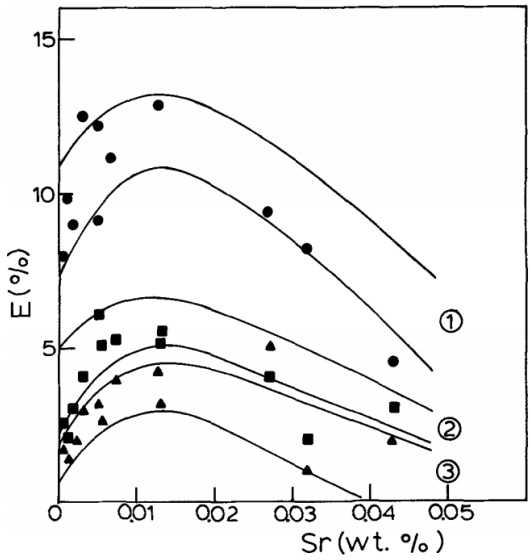


Figure 1-7. Effect of Sr content on the elongation of A356 alloy at three different cooling levels, (1) $1.5^{o}Cs^{-1}$, (2) $0.5^{o}Cs^{-1}$ and (3) $0.08^{o}Cs^{-1}$ [8].

- Magnesium

Figure 1-8 shows a phase diagram of the Al-Si-Mg system showing the different phases that form at different levels of Mg. The addition of Mg to Al-Si alloys is essentially to enhance the heat-treatment process through precipitation strengthening mechanism that results in $Mg_2Si$ phase within the Al matrix [5]. The effect of magnesium addition on ultimate tensile strength (UTS), yield strength (YS), elongation (E) and microhardness (VHN) of the Al phase on A356 alloy is shown in Figure 1-9 [20]. The results show that Mg addition has no effect on the elongation and the micro-harness which contradict the fact that $Mg_2Si$ phase formation increases the hardness of the Al-matrix. Thus, the increase in Mg should show an increase in micro-hardness. However, UTS and YS of the alloy continue to increase with increasing amounts of Mg.

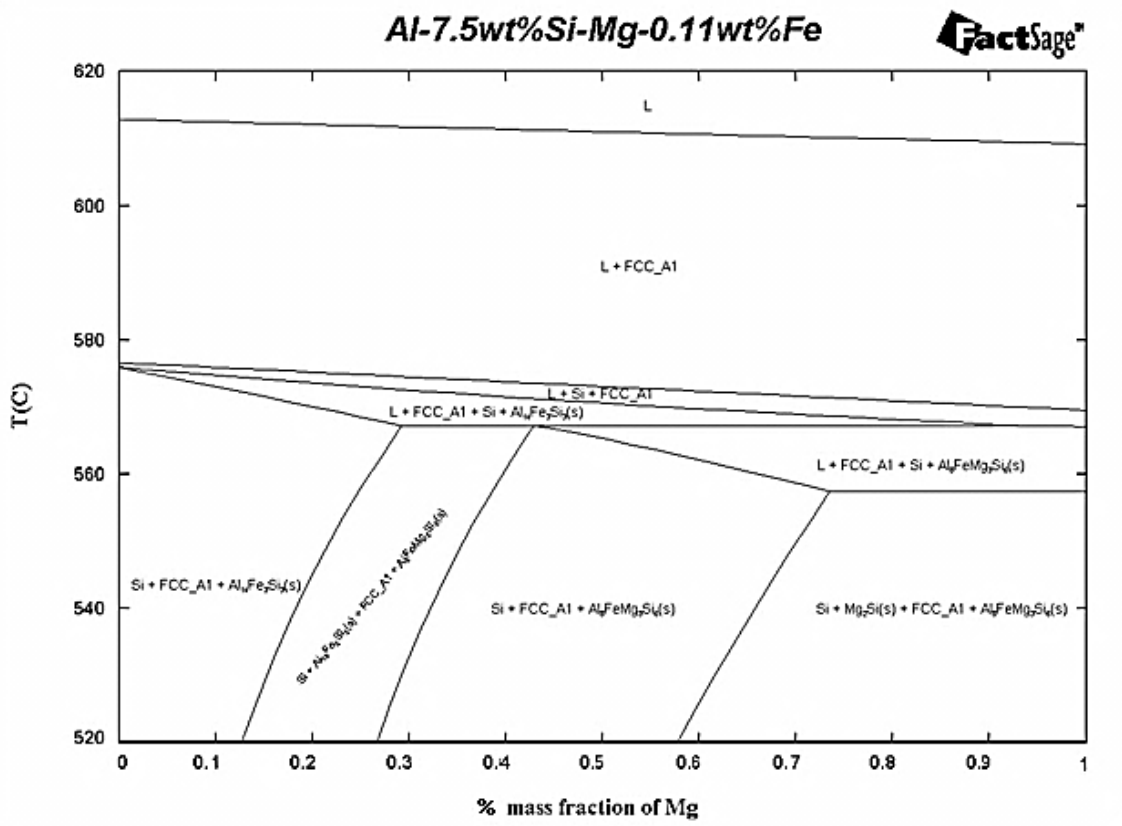


Figure 1-8. The effect of Mg on the phase diagram of Al-Si-Mg cast alloy developed using FactSage software [21].

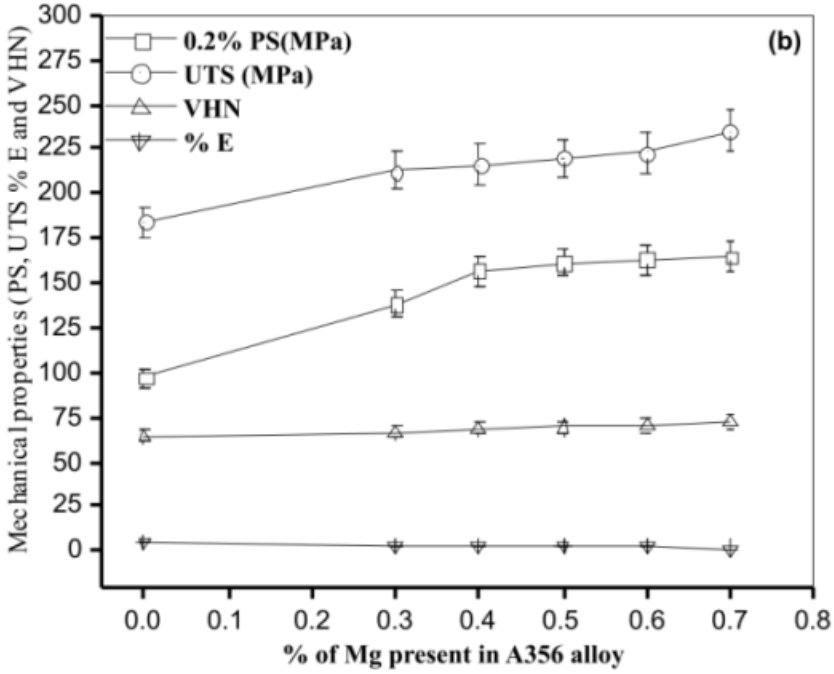


Figure 1-9. Effect of Mg on the mechanical properties of A356 aluminum alloy [20].

### 1.1.3 Effect of Solidification Cooling Rate

Delaying the solidification cooling of the cast enhances grain growth [22]. Figure 1-10 shows experimental data for average grain size versus the cooling rate during solidification for unmodified and Sr-modified A356 alloys. The log grain size decreases linearly with the increased cooling rate. Slow cooling rate has an adverse effect on the elongation of the alloy [8] (see Figure 1-7). Figure 1-11 shows the effect of the cooling rate on the dendritic arm spacing, the figure shows that the increase in the cooling rate refines the Al-matrix dendritic arm spacing (DAS) [23].

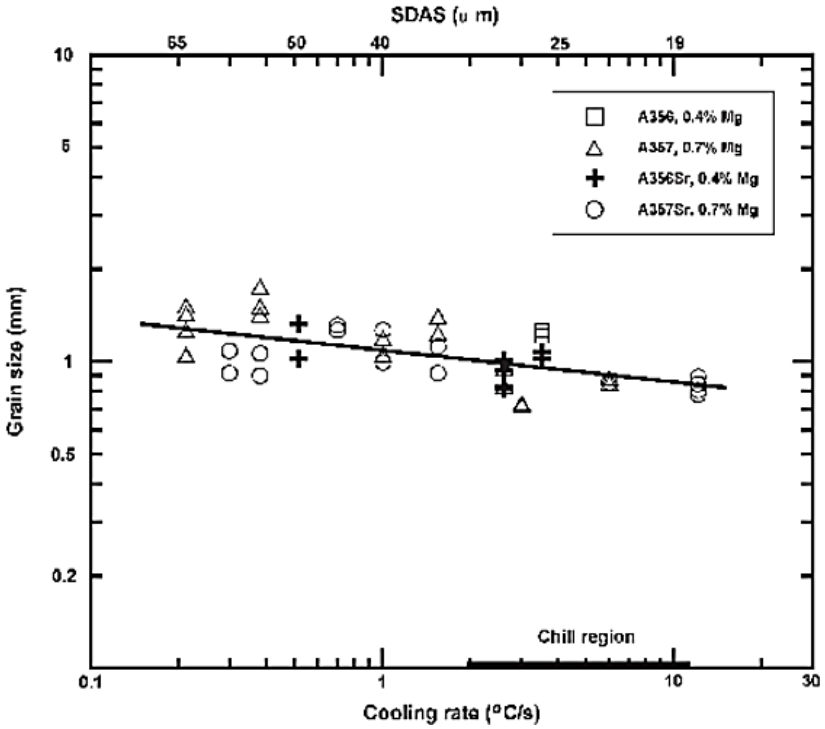


Figure 1-10. Effect of solidification cooling rate on the average grain size of unmodified and Sr-modified A356 [24].

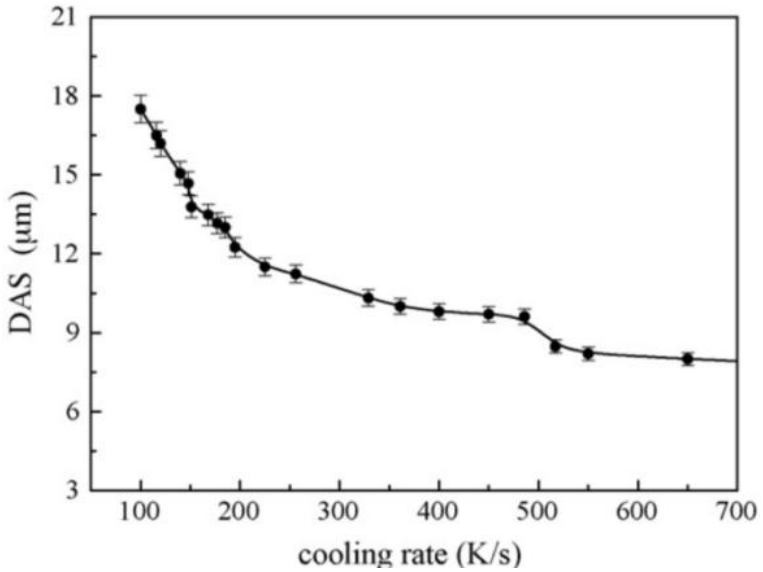


Figure 1-11. Effect of cooling rate on the dendritic arm spacing (DAS) on A356 aluminum alloy [23].

### 1.1.4 Heat Treatment

A useful aspect of A356 is that it is heat treatable in the cast condition enhancing its mechanical properties through precipitation strengthening mechanisms. Various heat treatment processes can be applied the Al-Si-Mg alloy, but the T6 temper is the most common in practice. A T6 temper consists of four main processes: solution treatment, quenching, natural aging and artificial aging (see Figure 1-12). A T4 temper is similar to where artificial aging is eliminated resulting in a more ductile material.

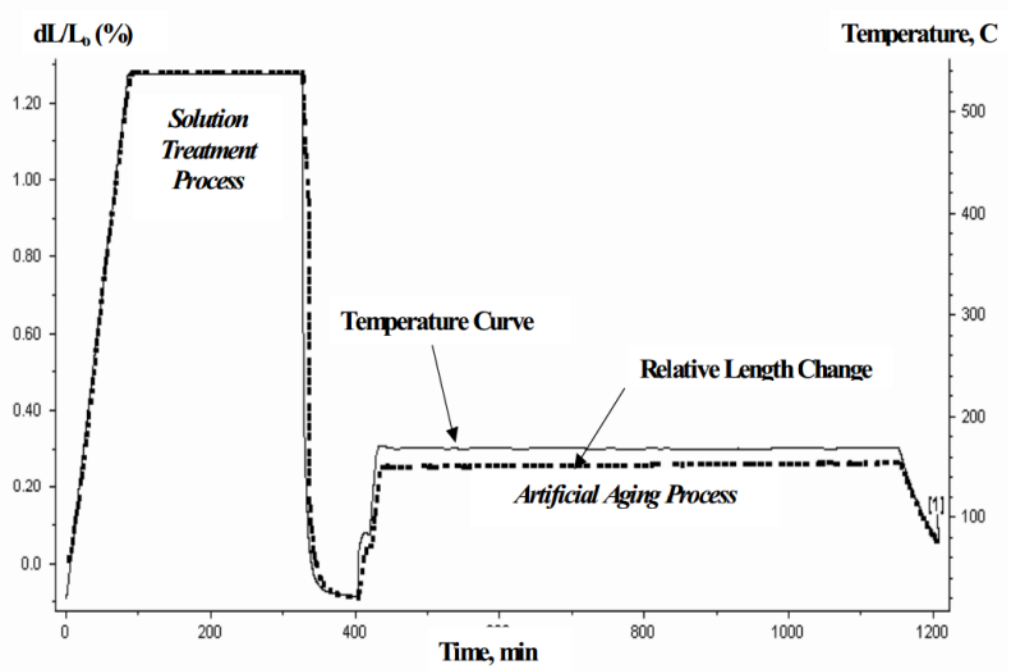


Figure 1-12. Typical T6 heat treatment cycle used for A356 cast alloy [25].

- Solution Heat Treatment

Solution heat treatment is the process of developing a supersaturated solid solution prior to cooling and aging, which is carried out by heating the alloy to sufficient temperature that allows both, Mg and Si, to dissolve in the Al α-matrix [26]. It is recommended to perform the solution heat treatment for A356 alloy at a temperature of $540^0$C [27] [28] [29]. The processes that take place during solution treatment are: the dissolution of Mg and Si in the Al α-matrix, homogenization of the casting and the spheroidization and coarsening of the morphology of the eutectic silicon. Figure 1-13 shows the stages that the eutectic silicon goes through during solution treatment for unmodified and Sr-modified compositions. Clearly, Sr addition modifies the eutectic Si phase particles subsequent spherodization and particle coarsening processes. Figure 1-14 shows the effect of solution time on the eutectic Si phase particles in sand and permanent mold

castings. The results show that solution time enhances the average size of the particles as the particles coarsen [30]. Solution treatment has a refining effect on the particles. The difference between sizes of particles in the sand and permanent mold is due to the melt experiences a higher cooling rate in the permanent mold. Figure 1-14 shows that solution time increases the particle size and decreases the number of particles and particle aspect ratio.

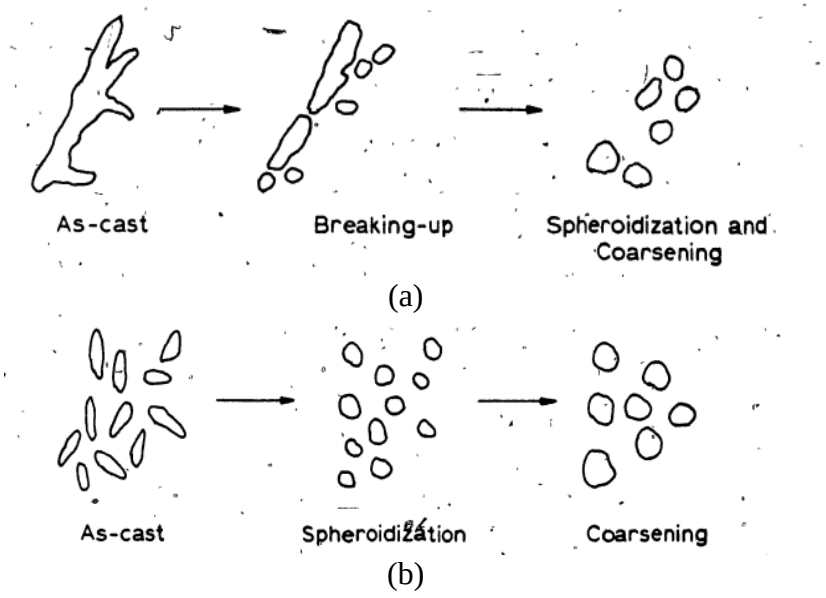


Figure 1-13. A schematic showing particle morphology development during solution treatment, (a) unmodified and (b) Sr-modified [31].

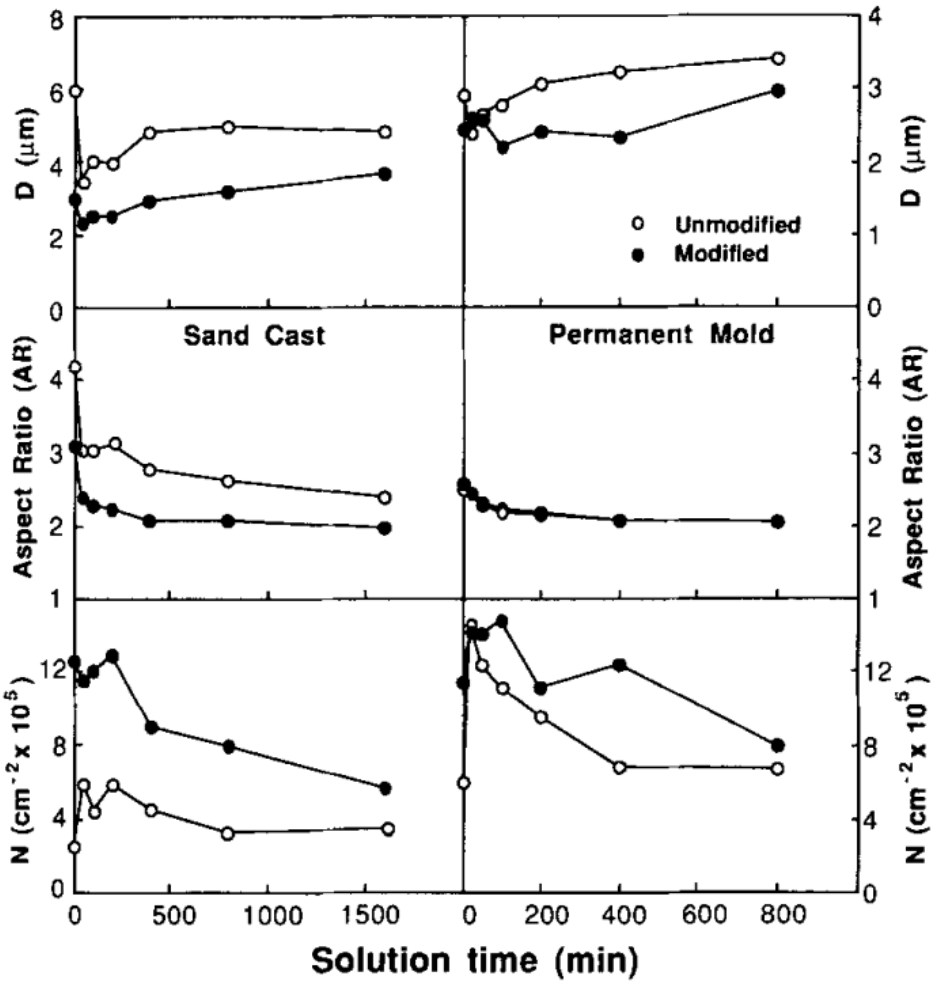


Figure 1-14. Effect of solution time on eutectic Si phase particles (size, aspect ratio and number) for sand and permanent mold casting [30].

- Quenching

The quenching from solution heat treatment temperature is used to attain the supersaturated solid solution at room temperature. Rapid quenching could lead to cast distortion [32] and increase residual stresses within the cast [33], whereas slow quenching would initiate the precipitation hardening as the cast quenches and affect the effectiveness of the aging process [33]. The delay time between solution treatment and quenching must be kept to a minimum according to ASTM standards [29]. It is highly

recommended not to exceed a delay time of 10s when quenching A356 cast alloy, whether cast in a sand mold or a permanent mold. It is common practice to use hot water as a quenching medium [30] even though quenching using cold water and air are used as well.

- Incubation

Incubation (natural aging) is the precipitation mechanisms that take place at room temperature [34]. When subjecting the cast to a T6 temper, the incubation is an unavoidable process [35]. The incubation process seems to have an adverse effect on the strength of the material, yield and ultimate strength, but enhances the elongation of the cast [36].

- Artificial Aging

Artificial aging is an iso-thermal process where the material is heated to an elevated temperature to enhance to formation of the $Mg_2Si$ phase within the Al matrix. This phase enhances the ultimate and yield strength of the material, whereas it has adverse effects on the alloy ductility (see Figure 1-15) [25]. Figure 1-15 shows the effect of the artificial aging temperature on the mechanical properties of A356, where the typical artificial aging temperature is around 155-170 $^0$C [25].

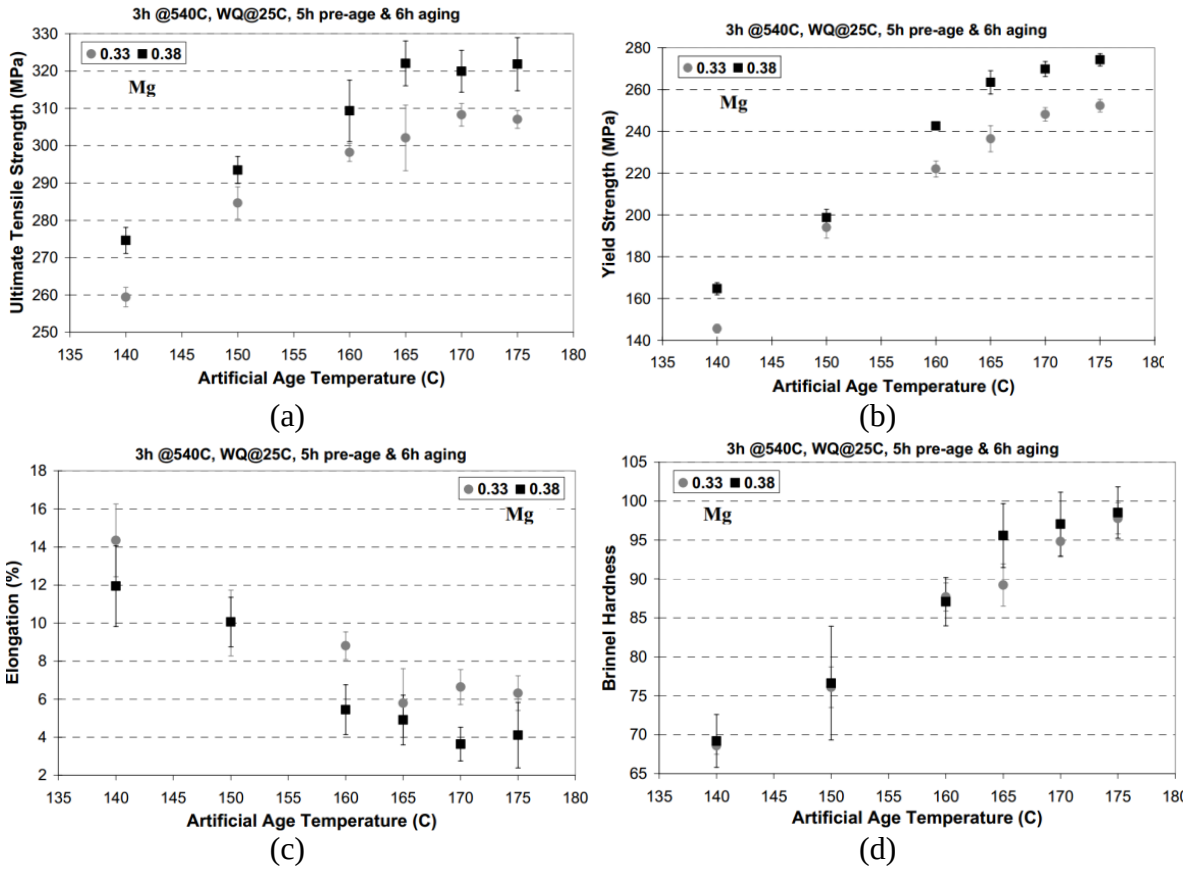


Figure 1-15. Effect of artificial aging temperature on (a) UTS, (b) YS, (c) elongation, and (d) Brinell hardness on the A356 alloy [25].

### 1.1.5 Deformation Behavior of A356

This section briefly summaries the work carried out on A356 cast alloy and is still a work in progress. Most of the work has been carried out in the literature on the A356 alloy is subjected to a T6 temper. The typical tensile and compressive stress strain curves for an A356-T6 alloy subjected are shown in Figure 1-16 [37]. The curves show that the alloy exhibits high strength and relatively low elongation when subjected to a T6 temper. The strength of the alloy is expected to decrease and the elongation increase if the alloy is subjected to a T4 temper.

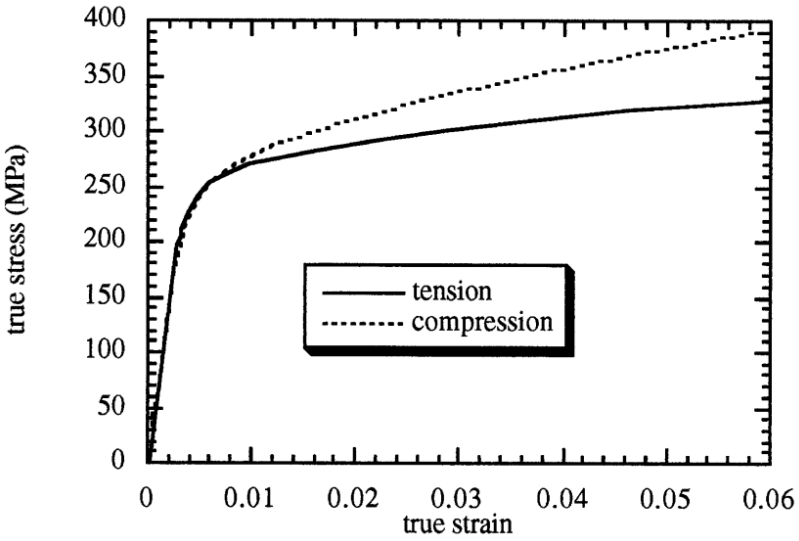


Figure 1-16. True stress strain curves for A356-T6 subjected to uniaxial tensile and compressive loading conditions [37].

A comparative study between the unmodified and Sr-modified A356-T6 was carried out to characterize the differences between both alloys when deformed plastically [24]. The shape of the eutectic Si phase particles plays an important role in the deformation behavior of the alloy. Larger elongated particles in the unmodified alloy tends to increase the yield strength of the material, but has an adverse effect on the total elongation when compared to the smaller, more round particles in the Sr-modified counterpart (see Figure 1-17). Another study on unmodified and Sr-modified A356-T6 alloy that focused on the effect of the dendritic arm spacing (DAS) was carried out [38]. The results show that DAS has a negligible effect on the elongation of the alloy (see Figure 1-18), but the results confirmed that Sr-modification enhances the elongation as seen in Figure 1-17.

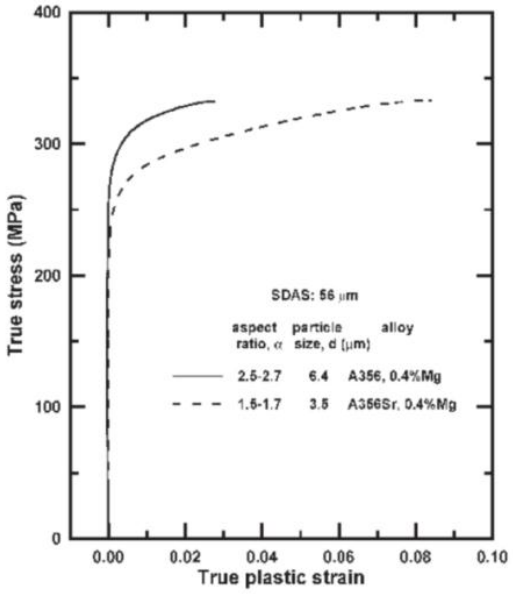


Figure 1-17. Comparison between the stress-plastic strain curves of the unmodified and Sr-modified A356 alloys subjects to T6 temper [24].

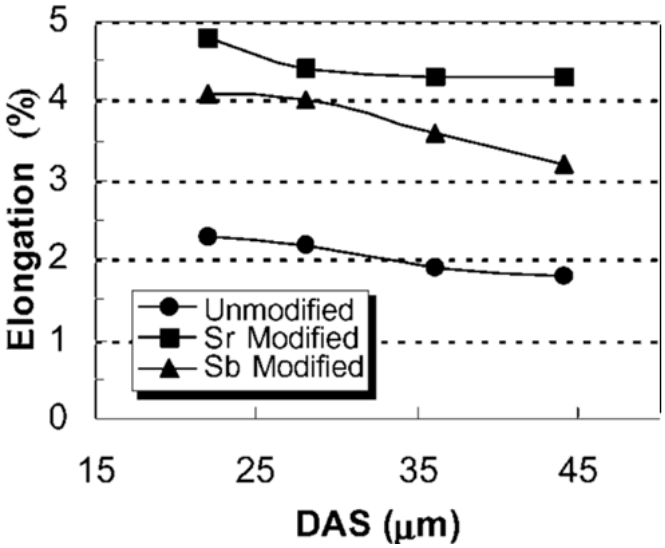


Figure 1-18. Effect of DAS on the elongation of A356-T6 [38].

Dighe et al. [4] have carried out work on the damage evolution on Sr-modified A356-T6 in tension, compression and torsion loading. The authors used an interrupted testing strategy to understand the progression of damage as the specimens deforms to fracture. The authors conclude that during tensile testing the eutectic Si phase particles show both mechanisms of damage, particle cracking and particle dechoesion from the matrix.

However, under compression and torsion loading the only damage mechanism observed was due to the cracking of the eutectic Si phase particles. They also observed that crack orientations within the particles are perpendicular to the loading direction, parallel to the loading direction and in a random manner in tensile, compressive and torsion loading, respectively. The crack particles in the different loading conditions are shown in Figure 1-19.

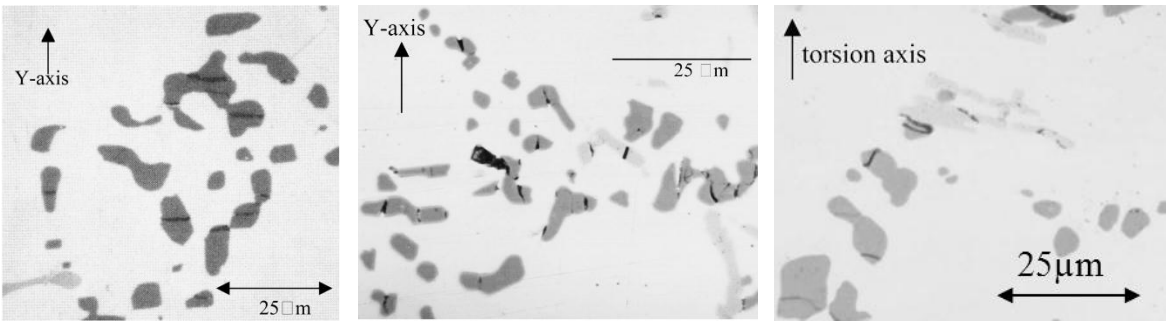


(a) (b) (c)

Figure 1-19. Fractured eutectic Si phase particles after deformation, (a) tensile, (b) compressive and (c) torsional loadings [4].

Figure 1-20 shows actual microstructural data coupled with FE simulation for eutectic Si phase particles in A356 subjected to tensile loading [39]. The results show that strain localization develops around the phase particles, which consequently contribute to damage and specimen fracture. The results incorporate variables such as size, shape and orientation of the particles. There has been no reported experimental work done on A356 that has analyzed the development of microstructure-scale deformation inhomogeneity at the eutectic Si phase scale. Such results would be valuable and would contribute to a deeper understanding of the damage process that occurs due to the intersection of particles and grains level deformation. There is virtually a complete lack of any studies

dealing with the effect of shape and size of eutectic Si phase particles on the bendability of the cast A356 alloy.

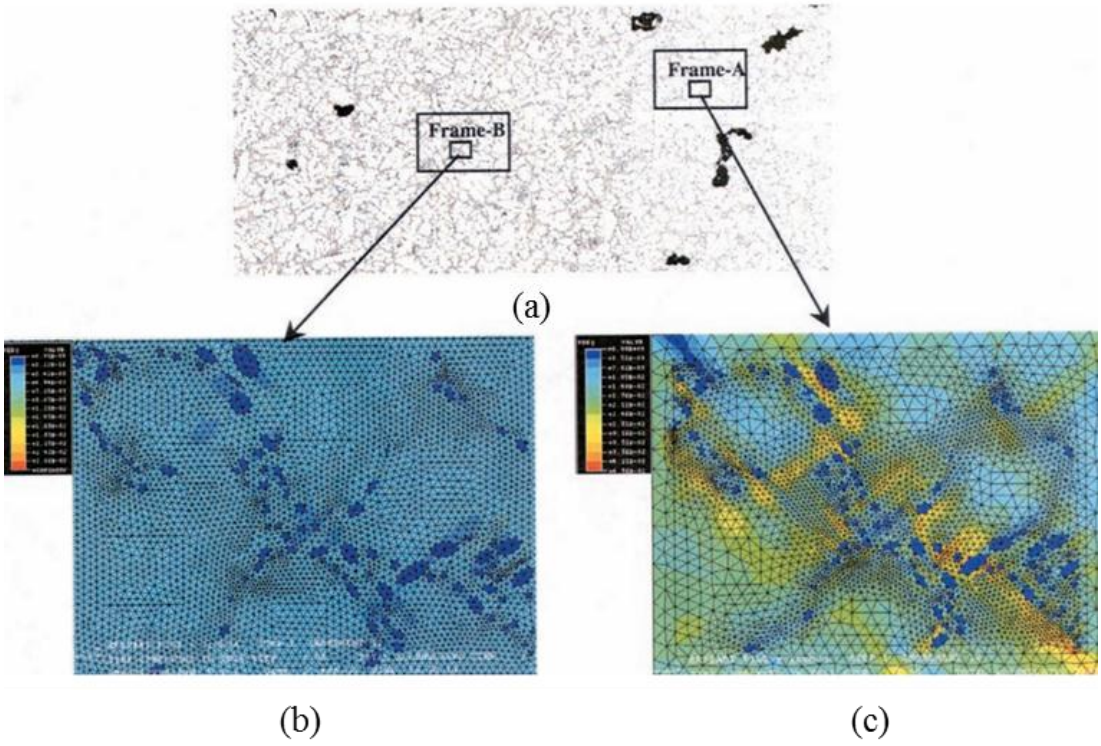


Figure 1-20. Equivalent plastic strains distributions around Si particles, (a) micrograph of specimen, and (b) and (c) FE simulation of plastic strains in regions B and A, respectively within the microstructure based model (a) under tensile loading [39].

The closest bendability work was carried by Friedman et al. [40], where the authors studied the bendability of two heat-treatable wrought Al-Si-Mg alloys and compared their performance with a non heat-treatable Al-Mg alloy. The authors claim that the failure of the alloys is strongly relating to the surface roughening that takes place due to bending. The authors note that surface roughening intensifies with a decrease in the bend radius regarding the state of the alloy (as-received or heat treated). Figure 1-21 shows the intergrannular nature of the crack of an AA6111 bend specimen tested by the authors.

The authors also noted that the heat treated specimens are significantly superior in bending compared to the as-received material.

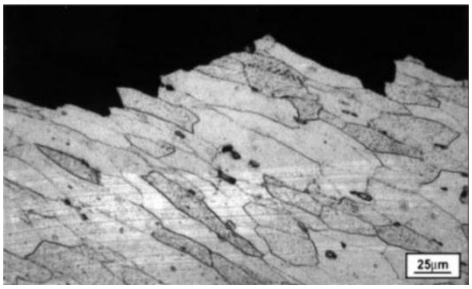


Figure 1-21. Micrograph revealing the intergrannular nature of fracture on the outer most surface of an A6111 bend specimen [40].

The study of A356-T6 alloy being subjected to different types of loadings such as fatigue and impact resistance (toughness evaluation) have been studied throughout the literature. Such loading conditions are not intended to be within the scope of the presented thesis. No studies have been reported in the literature that utilize full field strain measuring techniques to help understand the effect of grain structure on the deformation process in cast structures. Full field strain measuring techniques would provide with providing a further understanding of strain localization and inhomogeneity and to correlate it to microstructural aspects. The full field strain measuring techniques are elaborated in the upcoming section. The literature does supply strain maps based on FE simulations around eutectic Si phase particles [39]. However, the literature lacks the support of experimental data to back such simulations.

## 1.2 Strain Measurement Techniques

Comprehending the deformation process of any material is crucial to predicting the behavior of the material and life of a part in a given application. Development and

localization of strain leads to part failure. In this section the different methods of surface strain mapping is elucidated. Three typical methods of strain mapping are reviewed: direct grid method, digital image correlation and Moiré interferometry methods. The focus is mainly on the first two types. At the end of this section a comparison of the different techniques is offered, depicting advantages and limitations of each method.

### 1.2.1 Direct Grid Method

Direct grid method is an optical technique that utilizes a periodic grid pattern applied on the surface of specimens to be tested for full field strain evaluation. The technique utilizes an undeformed image of the tested specimen surface and a post-test image. This technique is not a real-time approach for strain measurements and only supplies strain maps (full field strain) based on initial and final images.

### 1.2.2 Digital Image Correlation Method (DIC)

The DIC method is an accurate displacement and strain measurement technique which employs image tracking and registration. The application of a random pattern applied to the specimen surface prior to testing [41] (see typical pattern in Figure 1-22). A series of images are recorded in real-time while the specimen is subject to plastic loading. The images are then utilized for a full field analysis of surface deformation or strain evaluation. Figure 1-23 shows typical two and three dimensional configurations of the DIC method, where one or more CCD camera(s) are utilized to record the surface deformation. A diffuse light source is recommended for adequate image contrast and to avoid excessive brightness and reflections, which can lead to loss of data. Consequently

the recorded images are transferred to a computer that processes the series of images using a dedicated DIC analysis software to construct a full field surface deformation map for the tested specimen.

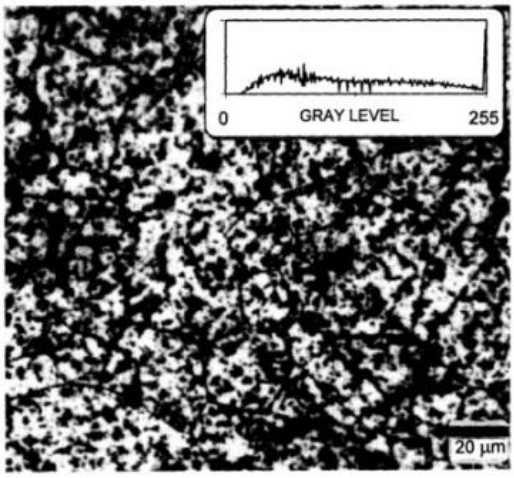


Figure 1-22. Typical speckle pattern applied to specimen surface for DIC method [41].

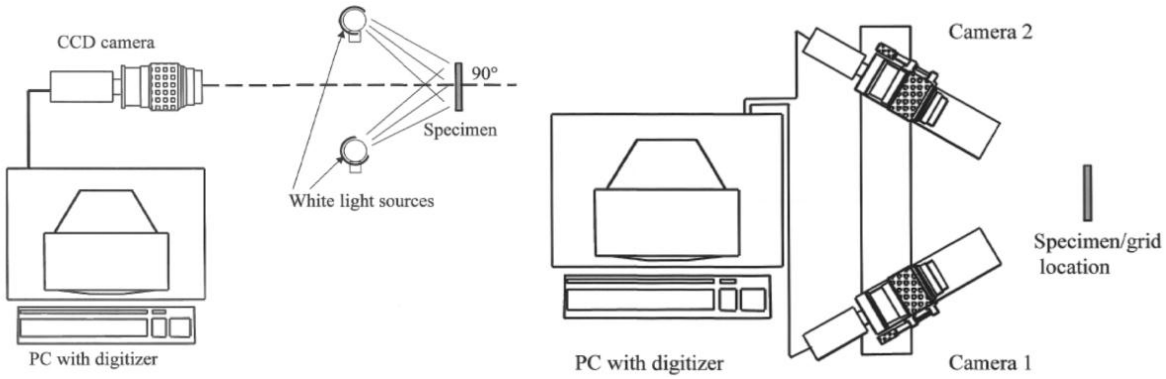


Figure 1-23. Schematic of a typical configuration utilized for DIC method, (a) two-dimensional and (b) three-dimensional configurations [42].

DIC method has various applications, from simple assessment of material deformation response to elastic and plastic loading to finite element model verification and validation. Some typical applications are as follows:

- Coupling DIC with optical microscopy

This technique proved the capability to detect strain inhomogeneity in neighboring grains in ferritic steel tensile specimen [43]. This work shows the capability of implantation of the DIC technique to understand the effect of the microstructure on strain localization in the A356 alloy.

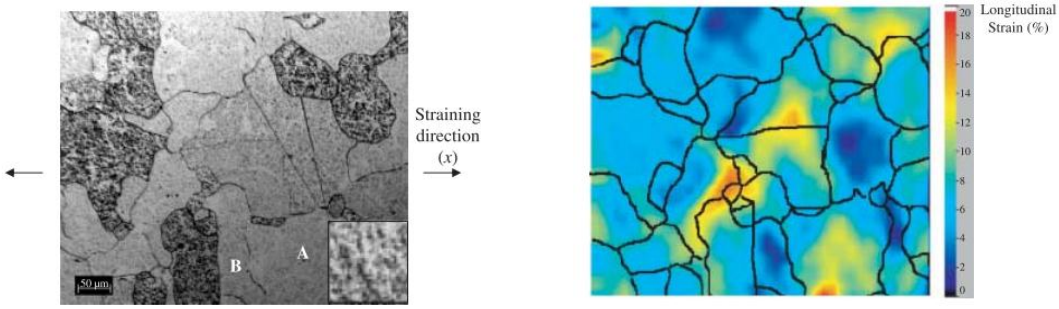


(a) (b)

Figure 1-24. Strain mapping using micrographs of deformed ferritic steel tensile specimen, (a) initial micrograph and (b) strain map of deformed specimen [43].

- Coupling DIC with FE models

DIC methods are really useful to validate results from FE models and simulations. A comparison of a FE model and DIC-based experimental results was carried out on AA6111-T4 when subjected to uniaxial tension [44]. Figure 1-25 shows the results in the form of strain maps developed by the model and experimental results. The results showed good agreement in strain distribution and strain localization characteristic prior to fracture.

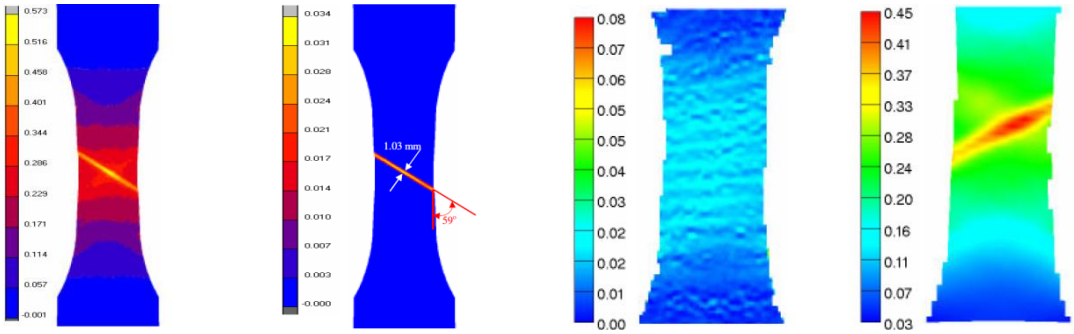


(a) (b) (c) (d)

Figure 1-25. Strain mapping of uniaxial tensile specimen revealing necking, (a) and (b) FE model, and (c) and (d) experimental results from DIC techniques [44].

These applications of the DIC method are few of the many existing in the literature indicating the reliability of the data, resolution and ease of implementation of the technique in a user-friendly software.

### 1.2.3 Moiré Interferometry Method

In-plane displacement fields can be measured using Moiré interferometry, and the results are presented in the form of interference fringe patterns or contour maps [45]. In the conventional method, a grid is applied to the specimen surface followed by specimen deformation. The Moiré interferometry method utilizes an undeformed master grid (analyzer grating lines) that is superimposed on the deformed specimen pattern producing Moiré interferometry fringes [46] [47]. Figure 1-26 shows a schematic diagram of a shadow Moiré interferometry setup. The setup comprises a light source, an environmental chamber where the specimen is tested, a reference grating (master grid) between the specimen and a video camera used to capture the resulting fringes as the specimen deforms [48]. Figure 1-27 shows the fringes developed for in-plane (u,v) displacement fields in thermal loading setup [49]. Moiré Interferometry is a full field technique with a very high sensitivity for in-plane displacements (could assess deformation in the nano-

scale using microscopic Moiré interferometry) [45]. This technique is real-time, works well with large or small displacements and exhibits a high signal to noise ratio. One of the drawbacks of this method is that it does not work well in out-of-plane deformation such as bending.

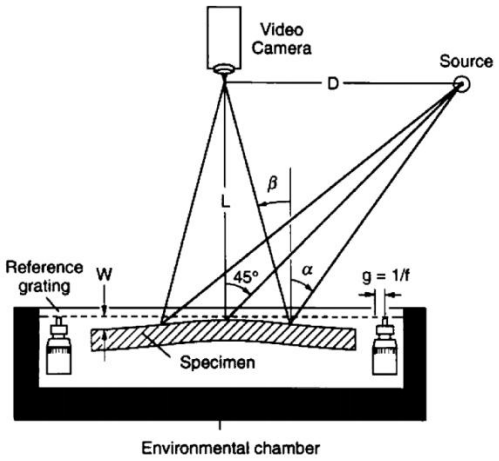


Figure 1-26. Schematic diagram of real-time shadow setup [48].

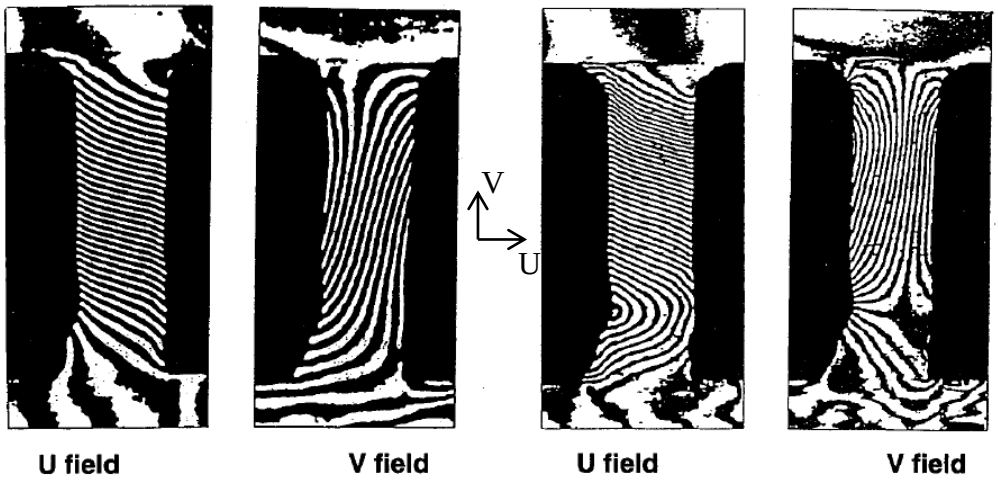


(a) (b)

Figure 1-27. U and V displacement fields induced by (a) initial thermal loading, and (b) four subsequent thermal cycles from -40 $C^o$ to 125 $C^o$ [49].

### 1.2.4 Comparison of Strain Mapping Techniques

Table 1-3 shows a comparison of the different techniques depicted in the previous sub-sections. One important difference between the direct grid method and DIC is that the latter is based on real-time acquisition (or in-situ testing), whereas the grid method is a post-deformation technique. Thus DIC enables a better understanding of how deformation progresses and what microstructural features may be responsible for flow localization, if the images are acquired at large magnifications. For this reason the direct grid method was disregarded. As for Moiré interferometry, the method is applicable at much smaller strains compared to the DIC method. Since the objective of the project is study the material deformation at large plastic strains, the use of Moiré interferometry was not considered. DIC method was therefore selected as the most suitable strain measurement method in the present work.

Table 1-3. Comparison between the different methods of strain mappings [50]

| Characteristics | Direct Grid Method | Digital Image Correlation | Moiré Interferometry |
|---|---|---|---|
| Physical Basis | Direct measurement | Amplitude (image contrast figures) | Frequency (spatial cross-line) |
| Data Acquisition | Post-mortem | In-situ or post-mortem (for small strains) | Real time in-situ or post-deformation |
| Strain Mapping | Differentiation of grid lines or crossing point locations | Direct numerical differentiation of displacement data | Digitalization of fringe patterns |
| Acquisition Hardware | No specialized hardware | Moderately demanding | Intensive |
| Processing Software | Minimal software | Intensive | Elaborate |
| Displacement Values | Absolute | Absolute | Relative, some uncertainty |
| Surface Quality | Smooth | Diffusive, as-received | Highly reflective, smooth |
| Surface Decoration Requirement | High quality cross-line or speckle grid | Random or ordered intrinsic or artificial features | High quality cross-line grating |
| Deformation Range | Medium to large strains | Small or medium | Small |
| Field of View | Wide field, limited only by the area of the grid | Wide field, limited only by the specific image formation system | Narrow to wide field, depends upon specific method |
| Resolution | Medium (depending on grid pitch) | High, depending on the surface and resolution of imaging equipment | High, depending on grating pitch) |
| Data Storage Requirement | Small | Large | Moderate |

## 1.3 Role of Microstructure in Strain Localization and Damage Development during Deformation

In this section, deformation studies from the literature that focus on strain localization and damage development carried out on various alloys are briefly reviewed. The review is focused on the role of grain and particle microstructure in deformation progression and strain localization.

### 1.3.1 Polycrystalline Structures

The plastic deformation of a material is strongly affected by grain orientations, grain boundaries and their vicinity [51]. It has been established that the study of grain boundaries could provide valuable information regarding the type and extensiveness of deformation [52]. The grain boundaries restrict the motion of dislocations as the material deforms plastically, which explains Hall-Petch relation where the yield strength is enhanced with grain-refinement [53]. Several studies provide an understanding of the grain interactions and the reason behind the development of inhomogeneous deformation using full field strain mapping techniques. It is also really important to understand grain scale heterogeneities as they may present structural instability and onset of fracture [54].

One relevant work was carried out on a coarse-grained Al-0.5%Mg multicrystal which focused on the study of grain deformation during plastically loading of a flat uniaxial tensile specimen [55]. Through the correlation of digital images of the surface of the tensile specimen, they were able to evaluate the in-plane plastic strains. The local crystallographic orientations were evaluated for the underformed specimen and after 5,

12 and 15% plastic strains with the aid of electron backscattered diffraction (EBSD) analysis. The authors found that material experiences extensive inhomogeneous plastic deformation, both intergranular and intragranular. They concluded that the material does not comply with polycrystalline plasticity models such as the well-known Taylor and Sach's models and that the material deforms heterogeneously in order to facilitate the slip transmission across grain boundaries. Figure 1-28 shows the slip-plane traces around various grain boundaries. The traces run from one grain to the neighboring grain continuously and often changing the orientation of the plane at the grain boundary. On the other hand, some slip-planes are discontinued at the grain boundary, as shown in Figure 1-28 (b,d). The slip is typically more intense at the triple junction.

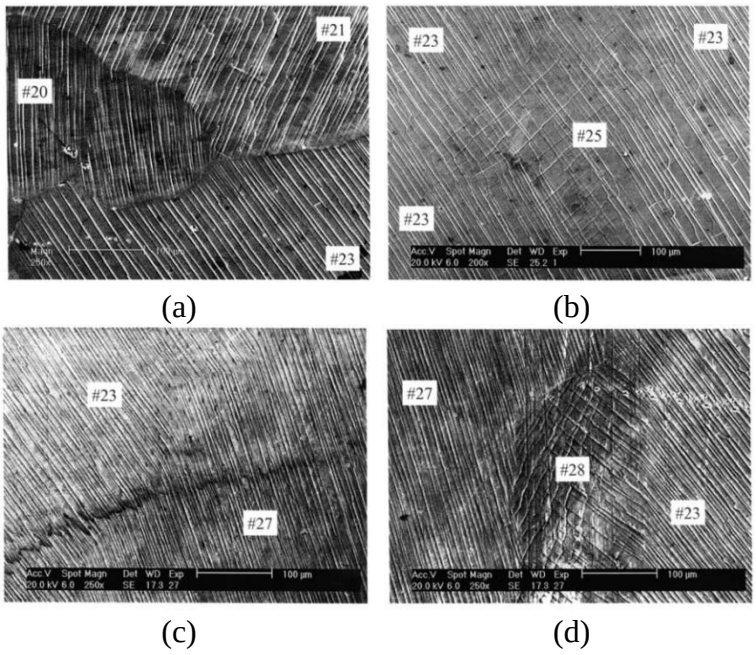


Figure 1-28. Slip-trace morphology and interaction at various grains boundaries in Al-0.5Mg, (a) triple junction, (b) within a single grain surrounded by a larger grain, (c) boundary between two neighboring grains, and (d) a smaller grain squeezed between two larger grains [55].

Another study involved the evaluation of strain inhomogeneity in an aluminum polycrystalline material with a coarse-grained microstructure during plane strain compression loading using DIC method [56] [57]. The authors observed that two different forms of grain deformation occurred during loading. One form is uniform deformation within single grain where the neighboring grains experienced significantly different strain values. The other form was described as "cluster-type deformation" where a group of neighboring grains experienced a homogenous deformation pattern. Figure 1-29 is full field maps of accumulated engineering plastic shear and von Mises strain incorporated with the grain structure distribution after straining the specimen to 15% global axial strain. Both types of deformation can easily be seen from these maps where location "A" shows a grain that experiences a uniform strain level and "B" shows a region across the specimen with a homogeneous deformation level across several grain boundaries. The authors conclude that using the DIC method is a useful tool of quantitative method for strain analysis at the grain level.

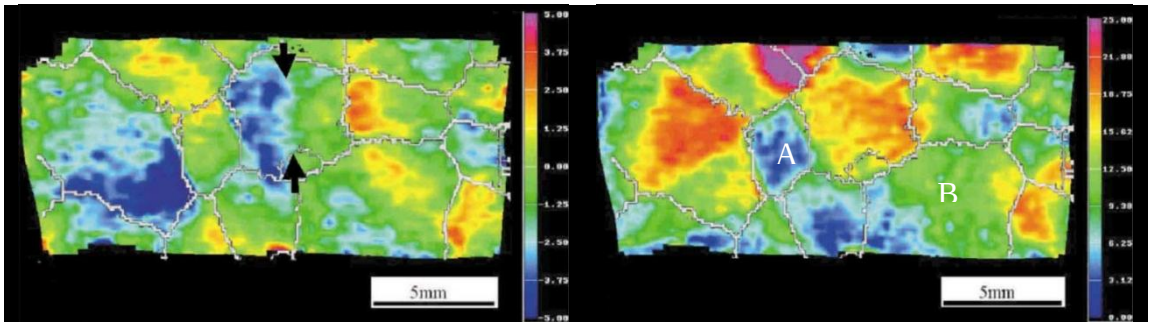


(a) (b)

Figure 1-29. Full field maps of (a) accumulated engineering plastic shear, and (b) von Mises strain at a 15% macroscopic axial strain [57].

### 1.3.2 Second Phase Particles

Second phase particles are particles distributed throughout the alloy matrix enhancing the alloys mechanical properties. In the case of A356, the second phase particles consist of eutectic Si phase particles. The particles usually play an important role in damage progression. The particles could either crack or debond from the matrix, creating "hot spots" for stress localization. Furthermore, void start to nucleate around these cracked/debonded particles and grow as the deformation progresses. The final stage of damage is the coalescence of these voids which finally leads to failure in ductile materials [58]. For this reason, an understanding of the mechanisms that enhance damage, whether it is the morphology of their particles or the distribution.

There exist extensive FE models and simulation results that are used to describe the behavior and evaluate damage spatially within the microstructure, which have not been verified experimentally [4]. Gurland et al. [59] have developed a model for the critical tensile stress σ within a particle, which is given by:

$$\sigma = \frac{E\gamma}{qD^{0.5}} \tag{1}$$

where E is weighted average of the elastic moduli of the matrix and particles, γ is the interfacial energy of the crack, q represents the particle stress concentration factor and D is the size of the particle. This model shows that larger sized particles require lower stress levels to fracture, meaning that larger particles fracture more easily when compared to smaller particles. The results show shows that stress concentration factor is inversely proportional to critical tensile stress, meaning that elongated particles would fracture more easily than the equiaxed or spherical particle.

## 1.4 Summary

Based on the above review of the literature, the following remarks are in order.

- The intent of this project is to study of large plastic deformation of A356 alloy. For this reason the T4 temper was selected rather than the T6 temper.
- The literature shows that strain mapping techniques are a good tool to be used to identify strain inhomogeneity and localization in order to be correlated with the microstructure.
- The DIC method is perhaps the most suitable for strain mapping techniques for the present work.
- No key papers were found on the bendability of cast aluminum alloys and particularly A356 alloy.
- No key papers were found on grain interaction and their effect on strain localization in cast alloys
- The FE models that describe the eutectic Si phase behavior during deformation of A356 exist but no experimental data is available for their verification.

## 1.5 Thesis Layout

The thesis presented is comprised of seven chapters (including the introduction and background chapter). A review of the literature is presented in this chapter. Chapter two introduces the motivations and objectives of this work. Chapter three introduces the method of specimen preparation starting from casting, heat treating and machining in

support of the deformation studies of A356 alloy. The chapter also shows the experimental equipment and software used to carry out mechanical testing, strain measurement and data analysis. Chapter four presents detailed results and discussion pertaining to the deformation studies on A356 alloy. Chapter five concludes the work presented in the thesis and chapter six provides several recommendations for future work.

# Chapter 2 Research Objectives and Motivations

The main objective of the presented thesis is study the deformation behavior of A356 alloy under different loading modes (tensile, compression and V-bending). The focus of the study is to elucidate the role of microstructure feature in A356 alloy that cause strain inhomogeneity and subsequently strain localization and damage when the material is deformed plastically. As indicated within the literature review chapter strontium modifies the morphology of the eutectic Si phase particles. This suggests using two different alloys, the unmodified and Sr-modified versions of the alloy. This would supply with two very similar alloys with rather different microstructures, fine and fibrous eutectic Si phase particles and coarse and plate-like eutectic Si phase particles. This would be used to compare the deformation behavior of the alloy based on the morphology of the eutectic Si phase particles. Also, the usage of Titanium as a grain refiner for comparing different grain sizes to understand their effect on the deformation behavior.

- **Development of an experimental technique for observing the deformation behavior of A356 cast alloy:** A suitable experimental technique for assessing the micro and macro-scale strain and damage development for uni-axial tensile, compression and V-bend tests is to be developed. The techniques will be utilized to assess the microstructural aspects of deformation of A356 alloy.
- **Investigate the effect of grain size on the mechanical behavior of A356 aluminum cast alloy:** This is to be carried out by using a set of different Ti levels, initially using a Ti-free cast and progressively increasing the Ti content. Ti acts as a grain refiner, resulting in a set of specimens with different grain sizes.

The different specimens will be subjected to microstructural analysis and mechanical properties assessment for a comparative investigation for the effect of the grain size and structure on the mechanical behavior of the material.

- **Investigate the shape effect and size of eutectic Si phase particles on damage progression and strain localization:** This is to be carried out by using two A356 alloys; unmodified A356 and Sr-modified. The refinement of the morphology of the eutectic Si phase particles as a result of the alloy modification will serve as an ideal counterpart to the unmodified alloy to study the effect of different eutectic Si phase particles morphology within cast alloys on the mechanical and deformation behavior.

# Chapter 3 Experimental Methodology

A detailed experimental methodology is presented in this chapter. The following summarizes the salient topics presented in this chapter:

- Material and Specimen Preparation
- Metallography
- Mechanical Testing
- Data Acquisition and Analysis

An overview of the project methodology is shown as a process flow chart in Figure 3-1.

## 3.1 Material and Specimen Preparation

Deformation studies were carried out on the Al-7%Si-0.3%Mg alloy with two levels of Sr and four levels of Ti. In this section, the specimen preparation starting from raw materials as furnace inputs to mechanical testing specimens (tensile, compression and bend testing) is described.

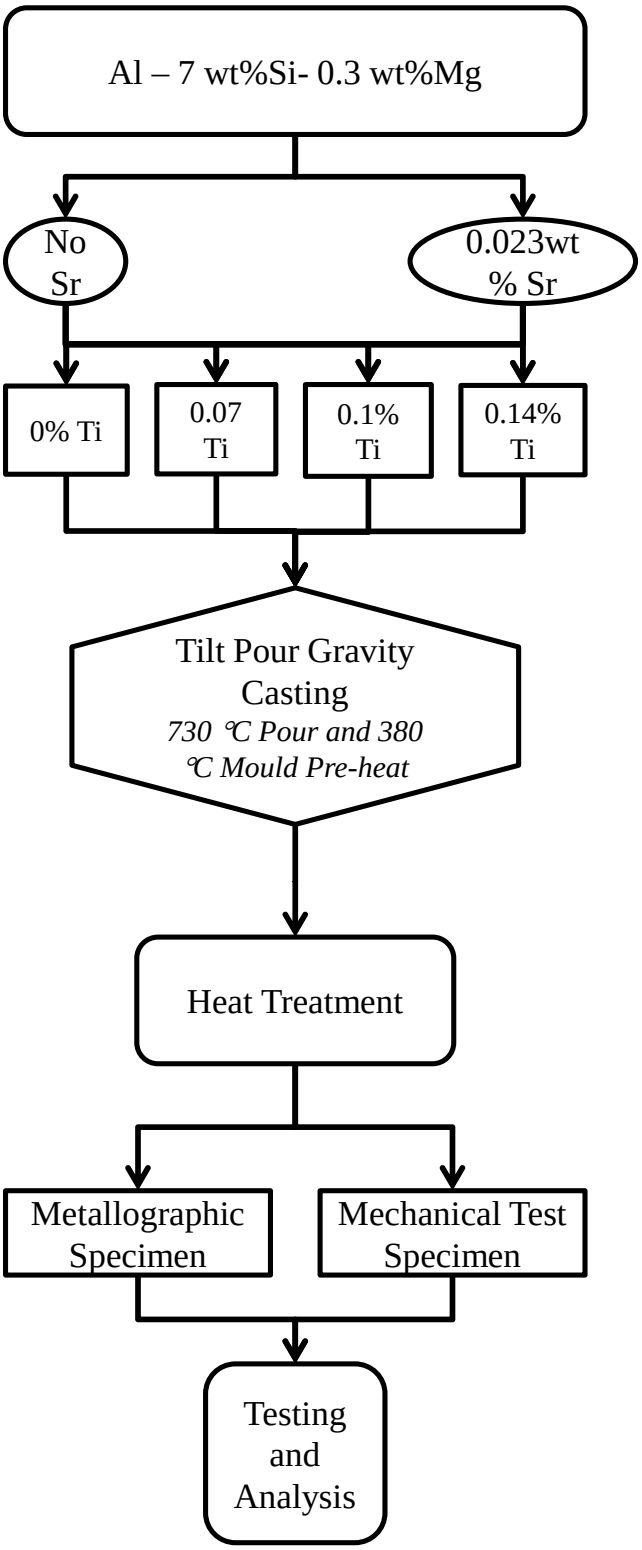


Figure 3-1. Flow chart showing a summary of casting, heat-treatment and machining steps.

### 3.1.1 Raw Material Preparation

The A356 alloy has a standard range of chemical composition for its constituents (see earlier section 1.1.1 for more details on A356 alloy). Al from ingots of commercial purity metal (see Table 3-1), and Si from Al-50wt%Si, Mg from Al-50wt%Mg, Sr from Al-10wt%Sr and Ti from Al-5wt%Ti-1wt%B master alloys were used to make the A356 composition in a 60 lb capacity electric melting and holding furnaces for casting the test specimen.

Table 3-1. Chemical composition (in weight percent) of the pure aluminum (P0404) ingot.

| Al | Si | Mg | Fe | Mn | Sr | Cu | Ti | Sn | Ni | Zn |
|---|---|---|---|---|---|---|---|---|---|---|
| 99.87 | 0.0152 | 0 | 0.047 | 0 | 0.003 | 0.011 | 0.0052 | 0.014 | 0.002 | 0.03 |

### 3.1.2 Casting

The A356 made in an electric crucible furnace was held at $750^0$C and cleaned by using a rotary degasser as shown by a schematic and photograph in Figure 3-2. In the rotary degassing method, ultra high purity (UHP) argon gas was purged through the shaft and rotor at a rate of about 6 $l.min^{-1}$ at about 400 RPM for about 20 min. The small and innumerable Ar gas bubbles in the molten metal enable the removal of dissolved hydrogen in the melt [60]. After the removal of hydrogen gas from the molten aluminum, the melt was cast into test specimen using the tilt pour gravity casting process (see Figure 3-3) and a test bar mold [21] (see Figure 3-4). The test bar mold consisted of two round dog-bone tensile specimens (see in Figure 3-5) with dimensions according to ASTM E8/E8M – 09 standard [61]. The mold pre-heat temperature was between 370 to $390^0$C so as to allow the cast to cool down at slower rate enabling larger Al grains.

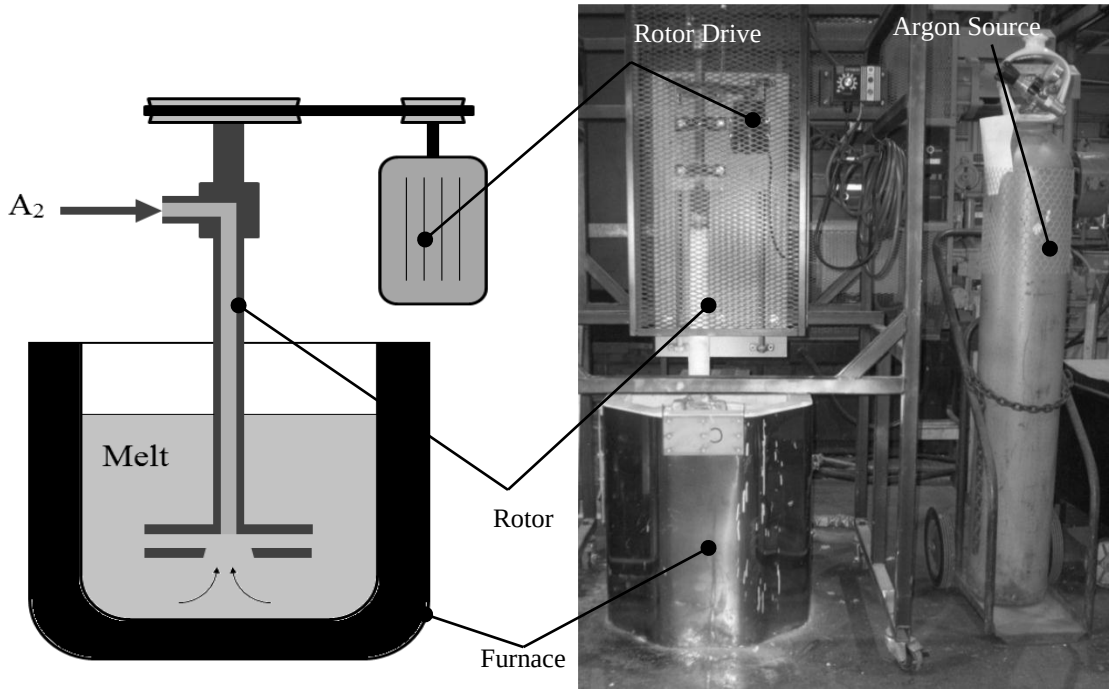


Figure 3-2. Alloy melting and cleaning, (a) a schematic of the rotary degasser and furnace, and (b) photograph of the degasser and furnace used in experiments.

A Cu mold was used to cast the specimen for chemical composition analysis (see Figure 3-6). Glow Discharge Optical Emission Spectroscopy (GDOES) was used for chemical composition analysis. GDOES is an analytical technique used to measure the elemental concentrations of solid materials. GDOES works by milling material from the sample surface using a stream of argon ions. The material sputtered is consequently excited in a low pressure plasma discharge and the resulting light emission is utilized to characterize and quantify the specimen composition. GDOES offers an improved excitation source for fast, economical, accurate, and reliable specimen turnaround. The machine utilized in this project for GDOES was the HORIBA Jobin Yvon GD-Profiler HR model

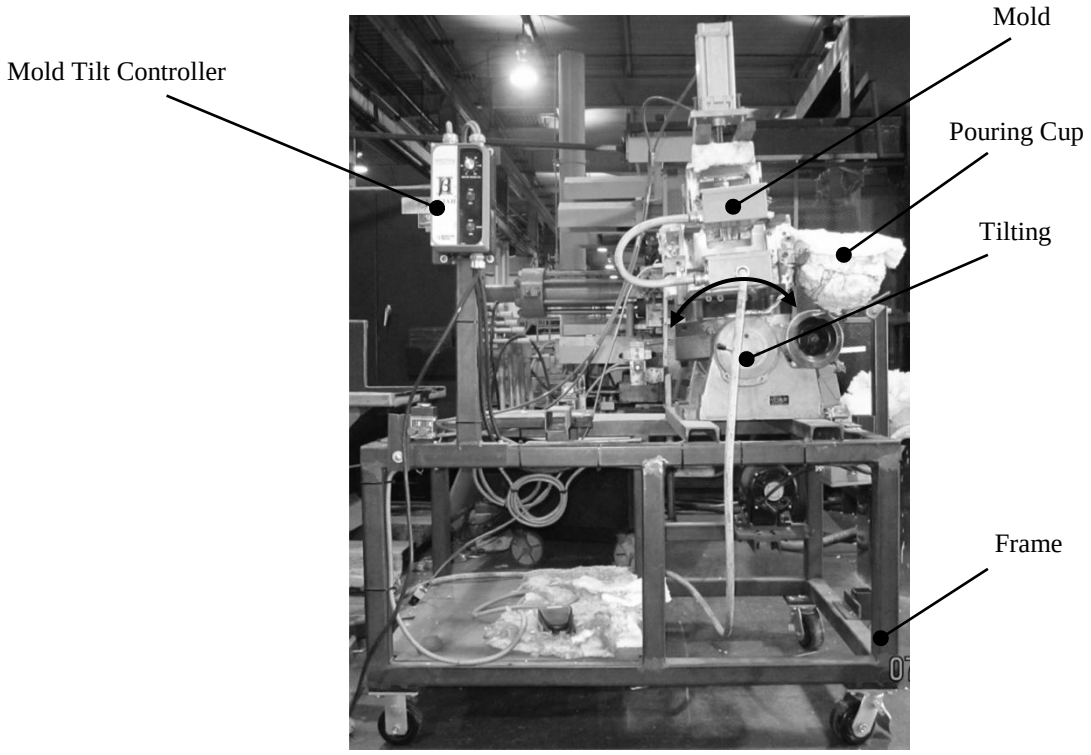


Figure 3-3. Tilt pour gravity casting machine used to cast A356 tensile specimens.

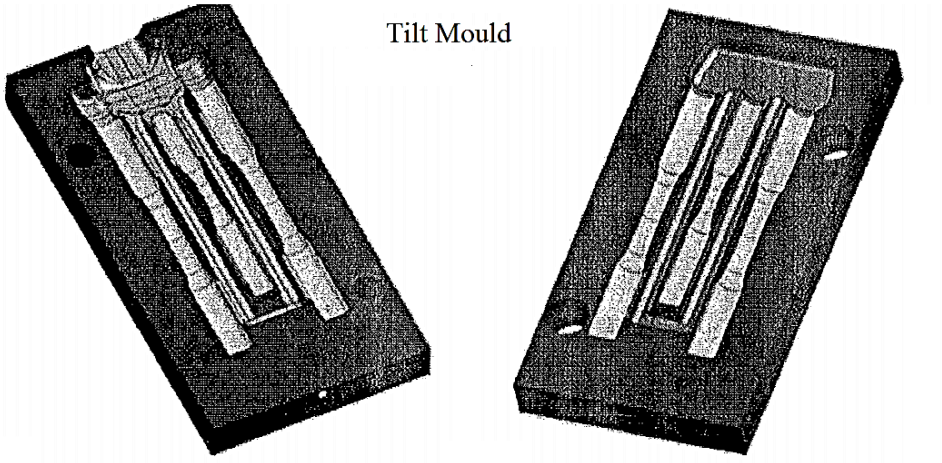


Figure 3-4. CAD drawing of the permanent mold used for tilt-pour casting of A356 tensile specimens [21].

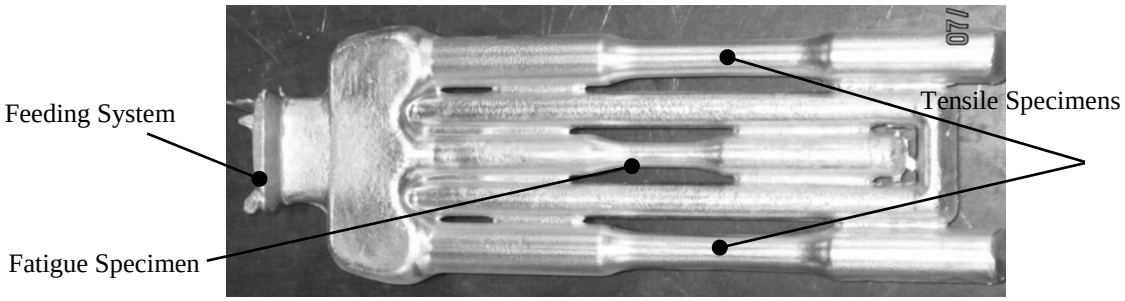


Figure 3-5. Typical casting after removal from the permanent mold.

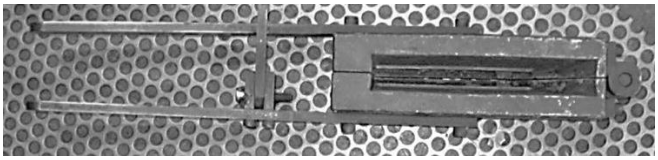

Figure 3-6. A photograph of Cu mold for casting specimen for chemical composition analysis.

### 3.1.3 Heat Treatment

The cast material was subject to T4 temper heat treating process consisting of solution treatment at $540^0$C for at least 12 hours at isothermal temperature followed by quenching in agitated water at 70-$85^0$C and then incubation at room temperature. The detailed methodology of heat treatment was as follows. First, the furnace, shown in Figure 3-7 (a), was heated until it reached steady state at $540^0$C. The cast specimens were placed into the furnace, and then were removed after 13 hours, and immediately subjected to quenching in agitated hot water. The water-filled quenching facility as shown in Figure 3-7 (b) incorporated a heating element and a thermocouple to monitor the temperature of the hot water. Once the water reached 70-$85^0$C range, the specimen were removed from the furnace and dipped into the hot water.

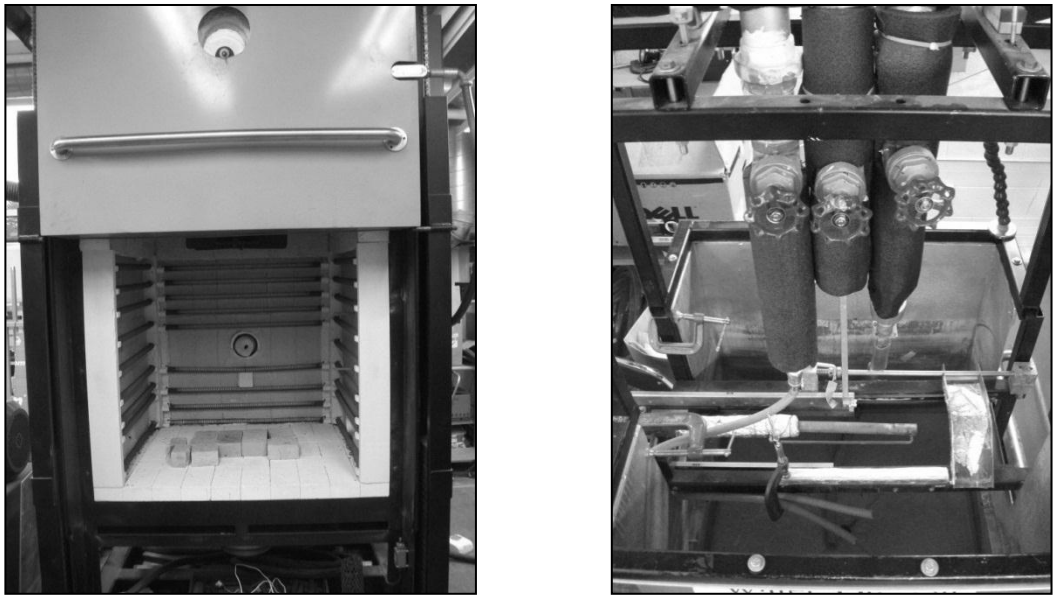

(a) (b)

Figure 3-7. Heat treatment, (a) electric furnace, and (b) water quenching facility.

### 3.1.4 Test Specimens Preparation

The heat-treated round tensile specimens were machined by first removing the runner, gates and riser with a band saw. The specimens were machined into tensile, compression and bending specimens with the required dimensions using a vertical milling machine. The dimensions of the tensile specimen are shown in Figure 3-8 (a), where the dimensions were kept to minimum possible width and thickness for the manually operated test rig (discussed in section 3.3). The compression specimens were machined to a rectangular cross-section (see Figure 3-8 (b)) to allow imaging of the flat surfaces to capture local strain data during testing using the strain mapping technique described in section 3.4. The bending specimens, as shown in Figure 3-8 (c), were also tested in a manually operated rig restricting the specimen dimensions as described in section 3.3. It is to be noted that the loading axes for the specimens is indicated using a center line shown in Figure 3-8.

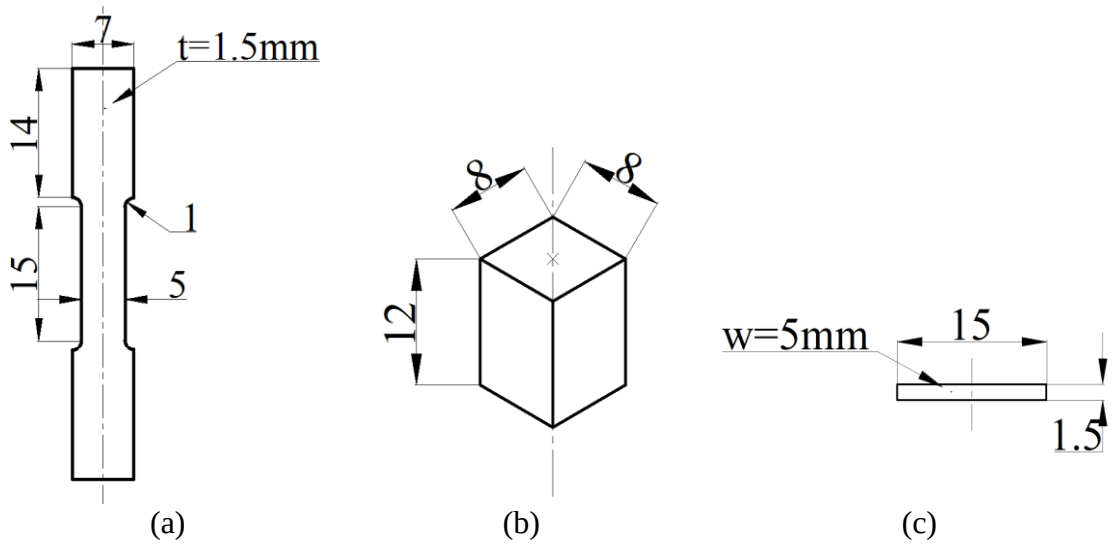


(a) (b) (c)

Figure 3-8. Specimen dimensions (in mm), (a) uniaxial tensile specimen, (b) compression specimen, and (c) bending specimen.

## 3.2 Metallography

This section presents the procedure for microstructure characterization using optical and scanning electron microscopy of the test specimens.

### 3.2.1 Specimen Preparation

The microstructures of as-cast and T4 specimens were analyzed by optical metallography. For a thorough microstructural characterization, specimens were observed in different orientations as shown in Figure 3-9. For hot mounting, the specimen were cut to size to fit in the Bakelite resin mold (diameter 31.75 mm), the specimen cutting was carried out using Struers Accutom-50 precise cutter as shown in Figure 3-10 (a). The cut specimens were then placed into Leco PR-25 mounting press shown in Figure 3-10 (b) and Bakelite powder was added. The mounted specimen were ground and

polished using manual and automatic grinding and polishing equipment (see Figure 3-10 (c-d)).

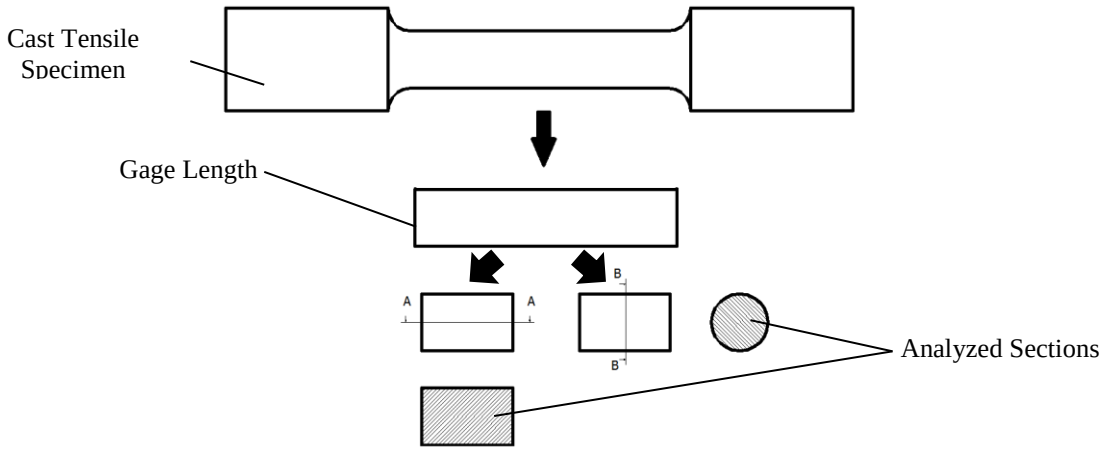


Figure 3-9. A schematic sections cutout from casted tensile rod for microstructure analysis.

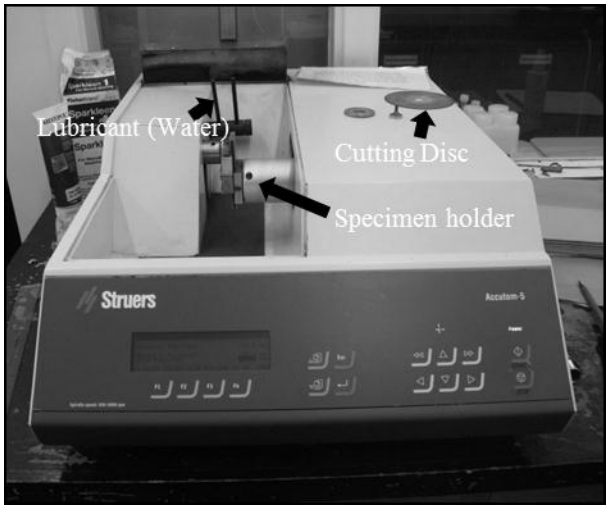


(a)


(b)

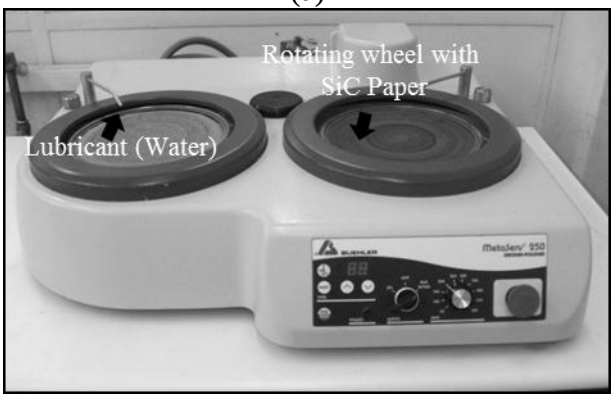


(c) (d)

Figure 3-10. Metallography specimen preparation equipment, (a) Struers Accutom-50 precise cutting machine, (b) Leco PR-25 mounting press for specimen mounting, (c) MetaServ 250 manual grinder/polisher and (d) Struers RotoPol-31 automatic polisher.

The typical polishing procedure used for aluminum alloys is presented in Table 3-2. The specimen is first ground using polishing papers (1200 SiC and then 4000 SiC). Then the specimen is polished using a series of polishing cloths and suspensions (3μm, 1μm and 0.05μm). The second phase particles, porosity and dendritic structure were investigated using light optical, regular and stereo microscope. For the characterization of the grain structure the specimens were etched prior to microscopic investigation.

Table 3-3 shows a set of etchants that were tried out with various A356 alloy. The modified Poulton's reagent and Barker's reagent proved successful with the alloy. Poulton's reagent was found to be rather corrosive and sometimes the grain boundaries were not easily defined. The results of etching the specimen with Barker's could only be seen under polarized light whereas Poulton's could be seen under regular white light.

Table 3-2. Typical polishing procedure used for aluminum alloys.

| Step | Polishing Medium | Duration (min) | Force (N/sample) | Lubricant |
|---|---|---|---|---|
| 1 | 1200 SiC polishing paper | 1.5 | 15 | Water |
| 2 | 4000 SiC polishing paper | 1.5 | 20 | Water |
| 3 | DAC (Nylon) polishing disc (cloth) - 3μm | 5 | 15 | 80% ethanol + 20% ethylene glycol + 3μm diamond suspension |
| 4 | NAP polishing disc (cloth)- 1μm | 5 | 15 | 80% ethanol + 20% ethylene glycol + 1μm diamond suspension |
| 5 | Neoprene | 5 | 10 | Collidal Silica + 10% $H_2O_2$ |

Table 3-3. Different types of etchants used for aluminum alloys. [62]

| Etching Type | Name of Etchant | Composition | Method | Duration (s) |
|---|---|---|---|---|
| Chemical | Modified Keller's reagent | 10 ml $HNO_3$ (conc.), 1.5 ml HCl (conc.), 1.0 ml HF (48%), 87.5 ml distilled water | Immersion | 30 |
| Chemical | NaOH–$Na_2CO_3$ solution | 2 g NaOH, 4 g $Na_2CO_3$, 94 ml distilled water | Immersion | 60 |
| Chemical | Poulton's reagent-solution | 50 ml Poulton's reagent (12 ml HCl (conc.), 6 ml $HNO_3$ (conc.), 1 ml distilled water, 1 ml HF (48%)), 25 ml $HNO_3$ (conc.), 40 ml of solution of 3 g chromic acid per 10 ml of distilled water | Immersion | 180 |
| Chemical | Modified Poulton's reagent-solution | 50 ml Poulton's reagent, 25 ml $HNO_3$ (conc.), 40 ml of solution of 1 g chromic acid per 10 ml of distilled water | Immersion | 10 |
| Electrolytic* | Barker's reagent | 4–5 ml $HBF_4$ (48%), 200 ml distilled water | 20 V DC (0.2 $A/cm^2$) | 80 |

*Anode: Specimen – Cathode: Stainless steel

### 3.2.2 Specially Designed Specimen Holders

Tensile specimen mount as shown below in Figure 3-11 was utilized for polishing tensile specimen for microstructure characterization prior to testing of the different cast structures. The mount was machined to size from a Teflon round stock and two specimens were attached to the mold using double-sided tape. The mount was inserted in the automatic polisher where the standard polishing procedure was followed as presented earlier in Table 3-2. For polishing bend and compression specimens, another mold, shown in Figure 3-12, was utilized where the mold was machined from an acrylic resin.

The mold had two orthogonal screws for adjustments, one from the top to ensure that the specimen orientation and the other from the side to lock the specimen in place. This mold was adaptable to various specimen sizes and shapes.

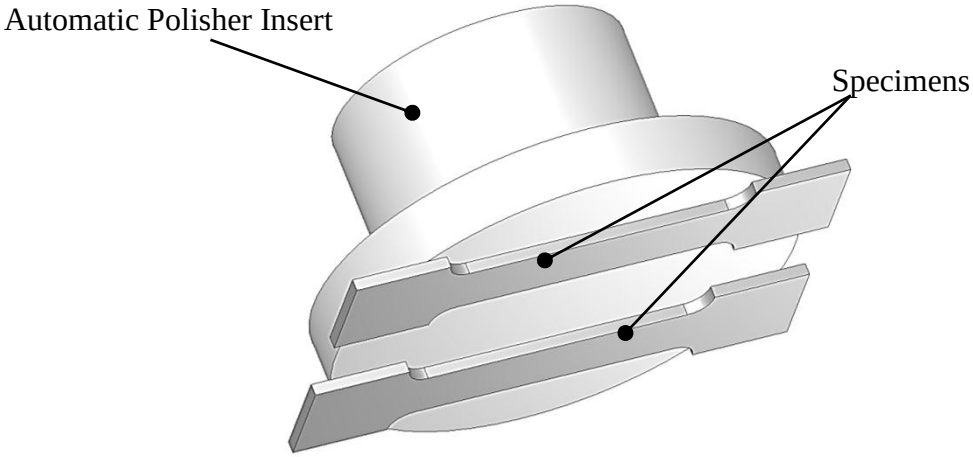


Figure 3-11. Tensile specimen holder utilized for specimen polishing and microscopy investigation.

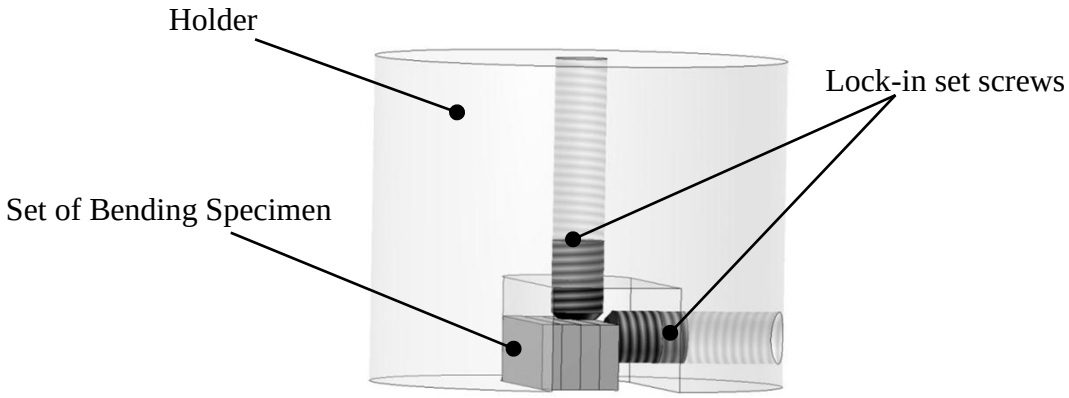


Figure 3-12. Bend and compression specimen holder utilized for specimen polishing and microscopy investigation.

### 3.2.3 Microscopy

Microscopic investigation of the alloys was carried out on a Nikon AZ100 stereoscope and Nikon Eclipse LV100 light optical microscope (see Figure 3-13). The stereoscope

range of magnification was 5X to 400X, whereas the microscope offered magnifications of 50X, 100X, 200X, 500X and 1000X. The low magnifications were useful for grain structure and porosity characterization, intermediate magnifications were used to characterize the dendritic structure and the high magnifications were used for eutectic Si phase particle characterization. For the microstructural analysis, a set of micrographs were acquired from different locations within a specimen of interest and from different specimen for each microstructure feature. The Phillips 515 Scanning Electron Microscope (SEM) was used for higher magnification investigation of fractured specimens.

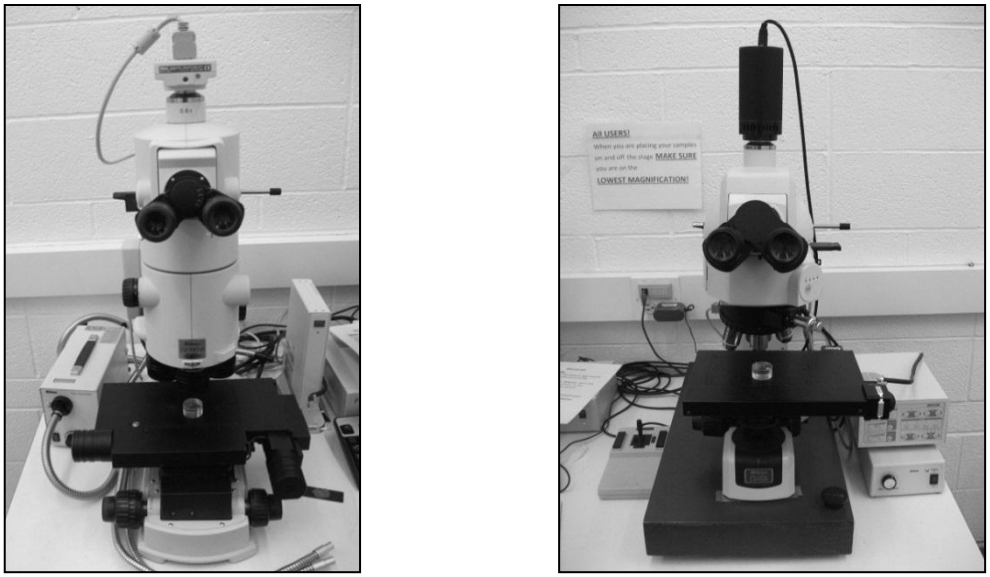


(a) (b)

Figure 3-13. Light optical microscopes (a) Nikon AZ100 stereoscope, and (b) Nikon Eclipse LV100 microscope.

### 3.2.4 Microstructure Characterization

The micrographs acquired from the microscope and stereoscope were uploaded to an image analyzing software, ImageJ 4.3U [63]. The quantification of the second phase

particles and porosity was carried out by automatic threshold and delineation of phases by the above image analysis software (see Figure 3-14 and Figure 3-15). The grain structure and secondary dendritic arm spacing (SDAS) were measured by manual delineation in the image analysis software (see Figure 3-16).

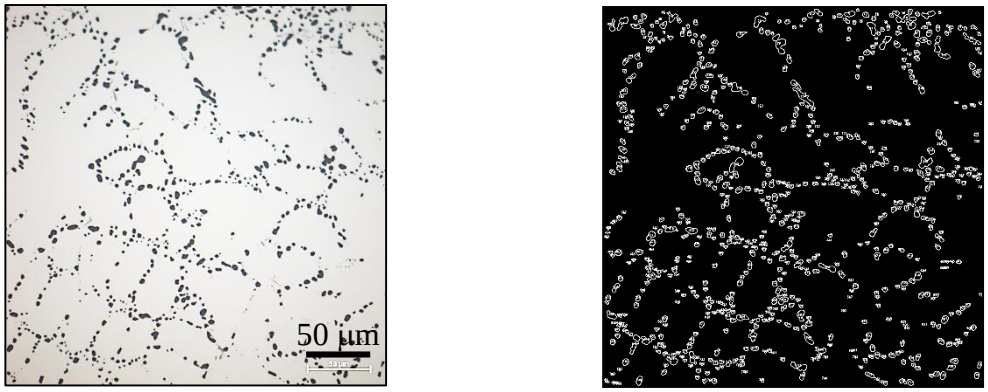


(a) (b)

Figure 3-14. Typical automatic image analysis of second phase, (a) micrograph (500X) revealing second phase particle distribution, and (b) automatic outline of eutectic Si phase in (a).

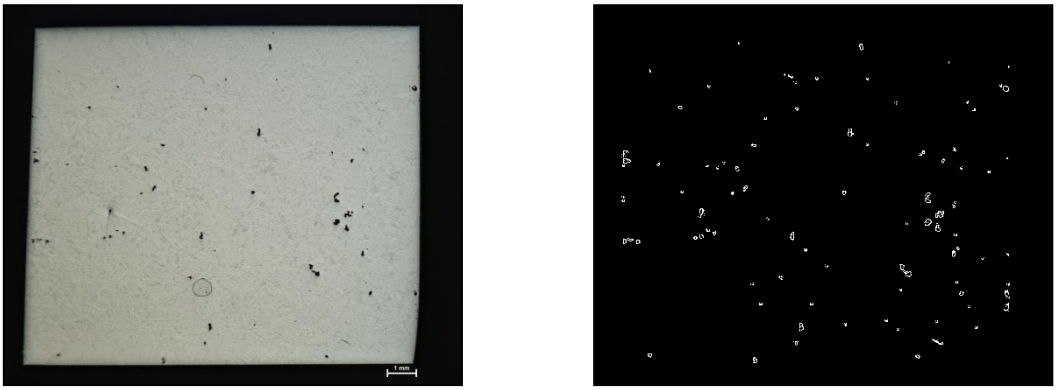

(a) (b)

Figure 3-15. Typical automatic image analysis for porosity, (a) micrograph (10X) revealing pore distribution, and (b) automatic outlining of pores by image analysis of (a).

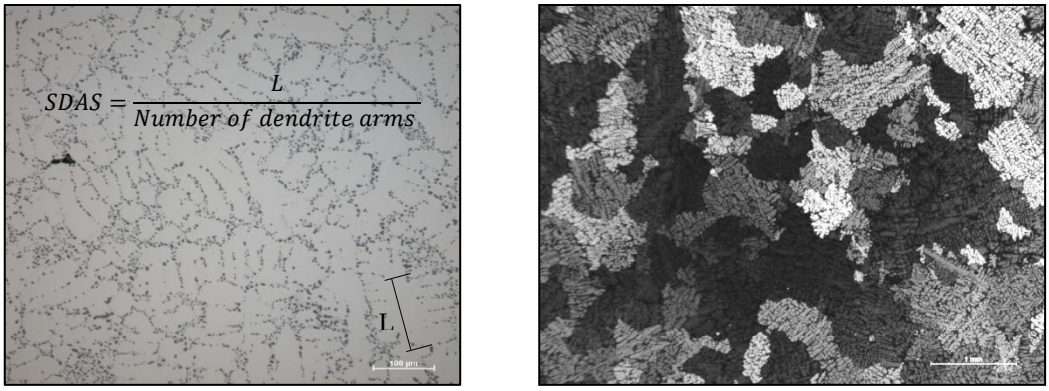


(a) (b)

Figure 3-16. Manual measurement of SDAS and grain size, (a) micrograph (200X) revealing a typical dendritic structure and SDAS evaluation method, and (b) typical micrograph (20X) of an etched alloy casting to measure grain size.

## 3.3 Mechanical Testing

The methodology for the tensile, compression and bending testing are described in this section.

### 3.3.1 Tensile Testing Configurations

Figure 3-17 shows two different test configurations used for tensile testing: (a) a single actuator, servo-hydraulic MTS frame with a 5 kip (kilopounds) load cell and (b) a universal screw-driven Instron 5566 test frame with a 10 kN load cell. With the MTS system, a CCD camera was used to capture the specimen deformation behavior during the test (see Figure 3-17). The captured images were then used in the ARAMIS software (described later in Section 3.4) to analyze and plot surface strain maps based on the Digital Image Correlation (DIC) method. With the Instron test system, a 12.5 mm extensometer was used to acquire global strain data. For both test systems, flat tensile specimens shown earlier in Figure 3-8 were tested at a 0.5 $mm.min^{-1}$ cross-head speed.

Figure 3-18 shows a screw-driven manually operated miniature tensile test jig that was also utilized for interrupted tensile testing with the objective of observing microstructure development with deformation during the test. A limitation of this test jig was that it was not equipped with any load and displacement measuring capacity. However, the displacement and macroscopic strain could be estimated by the number of turns of the screw after each interruption.

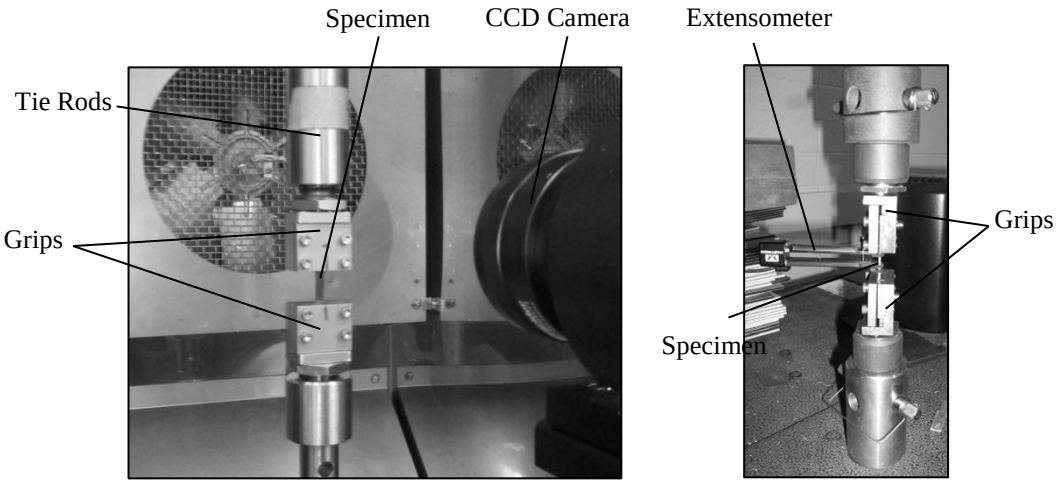


Figure 3-17. Tensile testing configuration, (a) in-situ Digital Image Correlation (DIC) strain assessment, and (b) using an extensometer.

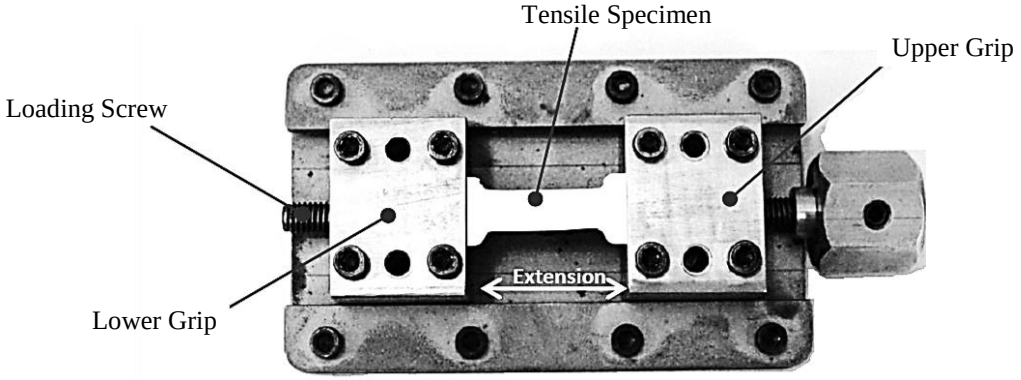


Figure 3-18. Tensile test jig used for microscopic investigation by in-situ testing.

### 3.3.2 Compressive Test Configuration

Uniaxial compression tests were carried out in the MTS mechanical test system, but with a 55 kips load cell due to increased failure loads expected in uniaxial compression compared to uniaxial tension. The specimen was placed between two using well-lubricated parallel plates and compressed while recording the deformation of the specimen surface with a CCD camera (see Figure 3-19). The images were later analyzed using the Aramis system (described later in Section 3.4) to obtain surface strain data. The test specimen geometry was shown earlier in Figure 3-8. The tests were conducted at 0.5 $mm.min^{-1}$ cross-head speed.

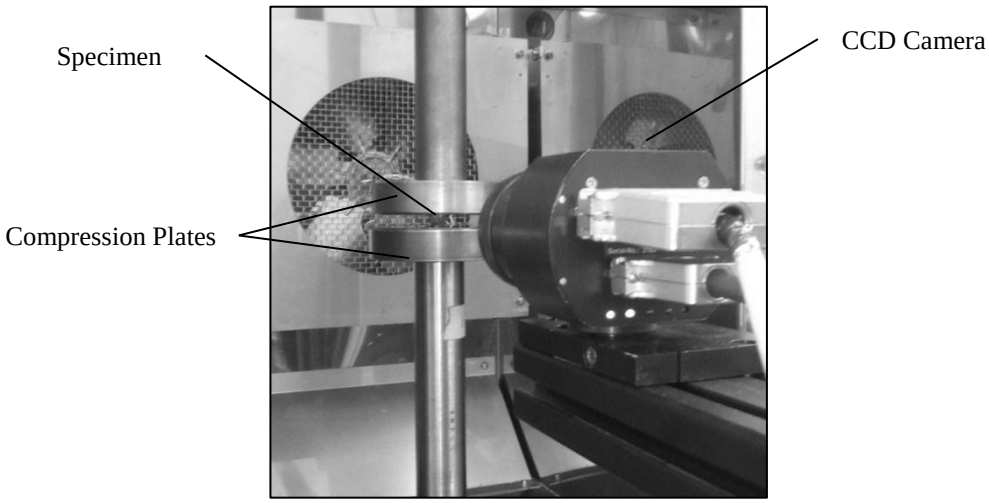


Figure 3-19. Compression test configuration equipped with DIC based strain analysis system (Aramis).

### 3.3.3 V-Bend Test Configurations

Figure 3-20 (a) shows the bend test configuration installed on the Instron 5566 test frame. The bend tests were conducted while recording images of the through-thickness region from one of the edges of the specimen. The images were later used within the Aramis system to obtain the strain maps. Load and displacement data was also acquired via the

in-built load cell and the Linear Variable Differential Transducer (LVDT), respectively. The tests were carried out at a mandrel speed of 1 $mm.min^{-1}$. Figure 3-20 (b) shows the dimensions of the mandrel and die radii. Another small test jig for in-situ bending study, equipped with a die and bending mandrel, was also utilized (see Figure 3-21). This jig was placed under an optical microscope and the specimen was deformed incrementally while images were captured at each increment.

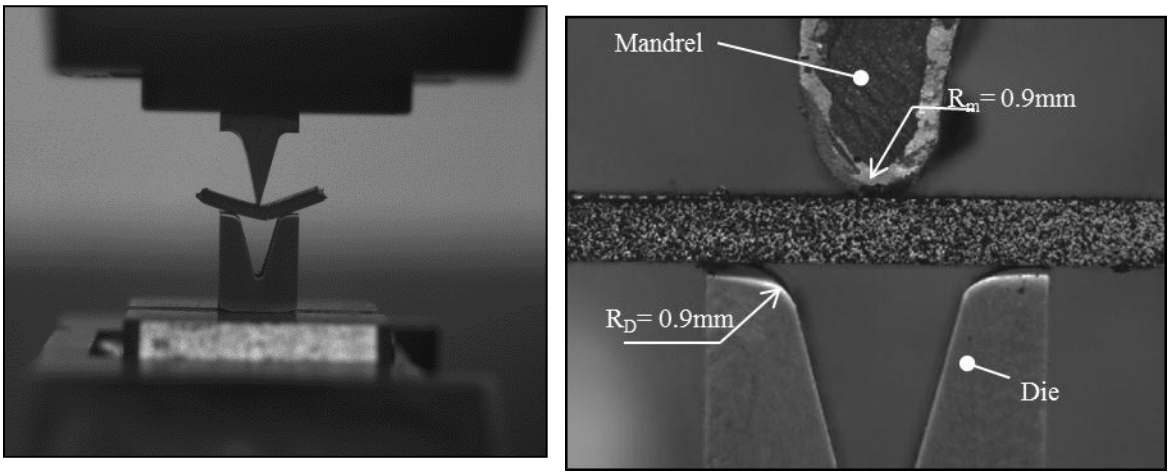


Figure 3-20. Bend test configuration, (a) Instron test frame, and (b) magnified image of the die-mandrel configuration.

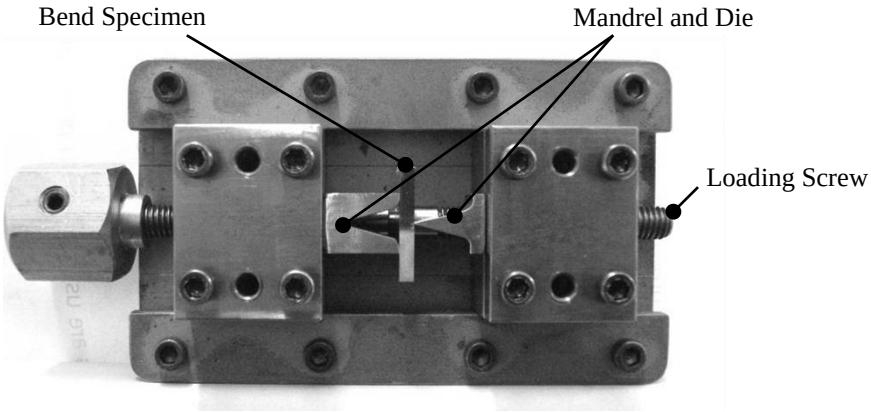


Figure 3-21. Tensile test jig used for microscopic investigation during in-situ testing.

## 3.4 Data Acquisition and Analysis

This section describes the strain data acquisition during the tensile, compression and bending tests on cast A356 specimens.

### 3.4.1 Strain Measurement Techniques

Strain data was analyzed in terms of global strain or local strain distributions (strain maps). The global strain, measured with a clip-on extensometer, is a measurement of the deformation in totality disregarding if deformation is localized in one or several locations throughout the specimen. Extensometers offer good resolution, accuracy and ease of data acquisition. On the other hand, local strain is measured with the Argus [64] and Aramis [65] systems and provide spatial strain data in the form of strain contours or maps, which are useful in identifying regions of inhomogeneous deformation. As explained in Chapter 1, there are two methods that could be used to develop strain maps of the surface, the direct grid method or the digital image correlation method. Argus and Aramis systems, available in the Metal Forming Laboratory at McMaster University, comprised of a CCD camera, data processor and software to analyze the data and utilize periodic grid and a speckle pattern respectively on the specimen surface as an input. Both systems were briefly discussed earlier in Chapter 1 and DIC method (i.e., Aramis system) was selected as the analysis tool for the experimental work.

Aramis system operates in 2D and 3D modes using 2 and 3 cameras, respectively. The 2D mode was sufficient for the flat specimens shown earlier in Figure 3-8. The DIC methodology is illustrated in Figure 3-22. A speckle pattern was applied to the specimen

surface prior to testing as shown in Figure 3-23. As the specimen was deformed, the CCD cameras captured images at a rate of one image per second. These images are then loaded on to the Aramis software where the images were converted to a gray scale. The software divides the loaded images into a matrix of facets and utilizes the speckle pattern within each facet to evaluate the displacement vector field to construct a comprehensive strain map. The limitation of this method is the resolution of the camera, camera magnification, depth of focus and fineness of the speckle pattern, which would result in a smaller facet size. As the selected facet size is decreased, one is able to capture strains around fine microstructural features such as pores, second phase particles and grain boundaries. Figure 3-23 shows an actual speckle pattern applied to a tensile specimen and the resulting strain map after loading the specimen.

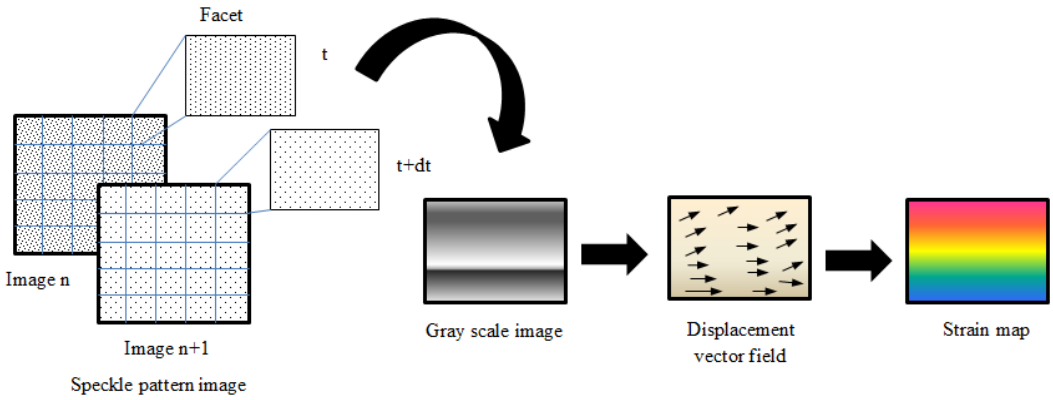


Figure 3-22. Steps in obtaining surface strain maps using digital image correlation method.

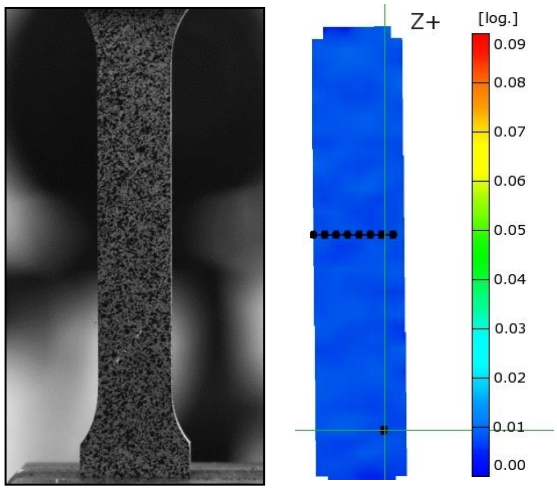


Figure 3-23. Photograph of typical speckle pattern applied to a flat tensile specimen along with the resulting strain map.

### 3.4.2 Damage Evaluation

Lemaitre has developed the following elastic modulus dependent damage parameter, D for a particle reinforced composite material subjected to tensile deformation [66] [67].

$$D = 1 - \frac{E_{current}}{E_{inital}}$$

where $E_{current}$ and $E_{intial}$ are the current and inital modulus of elasticity, respectively. The damage parameter can be obtained as a function of axial strain by conducting a sequence of unloading steps at different displacement values with a single test specimen. The slope of the stress-strain curve in the unloading region can be obtained by curve fitting to obtain the D parameter. Figure 3-24 and Table 3-4 show an example of the formulation of the damage parameter as a function of axial strain for a Ti-free Sr-modified alloy.

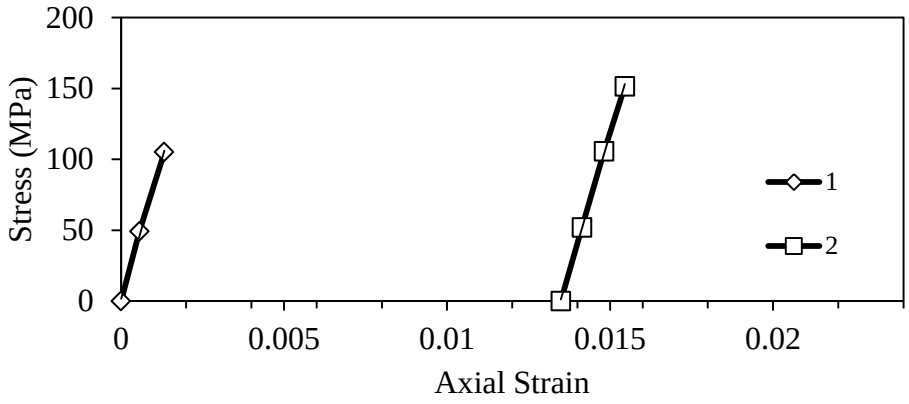


Figure 3-24. Typical evaluation of the change in modulus of elasticity as the specimen deforms, data is from the Ti-free Sr-modified alloy.

Table 3-4. Results of change in modulus of elasticity and calculated damage parameter extracted from Figure 3-24.

| Point | 1 | 2 |
|---|---|---|
| $E_{cur}$ (GPa) | 78.9 | 77.3 |
| D | 0 | 0.02 |

### 3.4.3 Second Phase Particle Cracking

For analysis of second phase particles that undergo cracking during tensile, compression or bending deformation, specimens were polished and examined using a Nikon optical microscope (sub-section 3.2.3). A large number of micrographs at 500X were acquired and uploaded to ImageJ software to analyze the cracked particle size and crack orientation with respect to the loading direction within the second phase particle, with the aid of histograms.

### 3.4.4 Surface Topography

Figure 3-25 shows an optical profilometer as a non-contact method of providing surface topography profile data. The core technology of the Zygo NewView 5000 profilometer is

based on low coherence interferometry. The Zygo was utilized to analyze the change in surface topography of tensile specimen surfaces as a function of axial strain. Each specimen was analyzed at different strains with respect to the stress-strain curve (interrupted testing). Tensile specimens were polished prior to testing and then pre-strained to 0.025, 0.05, 0.075 as well as to fracture. Pre-strained test specimens were analyzed using the Zygo system which typically utilizes an area of investigation of 1.83 mm x 1.37 mm at low magnification. Several points were investigated and mean values of surface undulations were calculated at each pre-strain. Using the initial surface topography and several values of the pre-strained specimens, a plot of the trend of surface deformation as a function of global true strain was developed. A plot for different alloys with different grain sizes was constructed to correlate of grain size and surface deformation during deformation.

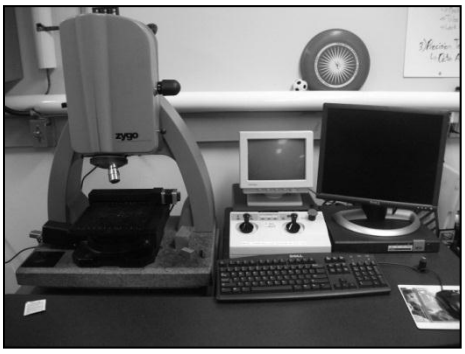


Figure 3-25. A photograph of Zygo NewView 5000, a non-contact surface profilometer.

### 3.4.5 Bending

Wang et al. [68] developed an analytical model for bending moment prediction for a plane strain V-bending condition. Their final expression, as shown Equation 3-1, considers both the moment required to bend the specimen and moment needed to overcome the friction between the die and the specimen.

$$M_{external} = M_{bending} + M_{friction} = \frac{PL_d}{4}\left(1 - \frac{4R_D}{L_D}\sin\theta\right) + \frac{PL_d}{4}\frac{\tan\theta - \mu}{1 + \mu\tan\theta}\left(\frac{2d}{L_D} - \frac{2R_D}{L_D}(1 - \cos\theta)\right) \quad (3\text{-}1)$$

where $M_{external}$ is the total moment exerted by the test frame, $M_{bending}$ is the the moment causing the specimen to bend, $M_{friction}$ is the moment to overcome the friction between the specimen and die, P is load applied (load cell data), $L_d$ is the distance between the radii of the die, $R_d$ is the radius of the die shoulders, $\theta$ is the bend angle, $\mu$ is the coefficient of friction between the die and the specimen material and d is the punch displacement. The model in equation (3-1) was used to plot the total moment versus bend angle.

# Chapter 4 Results and Discussion

This chapter presents the results and the respective discussion of the analysis of results in the following format:

- Material and Microstructural Analysis
- Deformation Characteristics in Tensile Loading
- Deformation Characteristics in Compression Loading
- Deformation Characteristics in V-Bending

## 4.1 Material and Microstructural Analysis

This section presents the results of cast samples and metallographic analysis of the same.

### 4.1.1 Overview

Table 4-1 shows a summary of the chemical composition analysis for the cast alloys. As mentioned in the previous chapter (see Figure 3-1) two main alloys were cast, unmodified and Sr-modified A356 alloys and every alloy had four different levels of Ti in the A356 base composition. The various impurities such as Mn, Fe, Cu, Sn, Cr, Ni and Zi in the cast alloy were minimal and within specified impurity levels for A356. Both Si and Mg content were maintained at constant levels ranging between 6.5-7 wt% and 0.232-0.267 wt%, respectively. The notations for the different levels of Ti used hereafter are also shown in Table 4-1.

Table 4-1. Chemical composition of cast A356 alloys.

| Cast | Unmodified | | | | Sr-Modified | | | |
|---|---|---|---|---|---|---|---|---|
| Ti-Level | 0 | 1 | 2 | 3 | 0 | 1 | 2 | 3 |
| Notation | Ti-0 | Ti-1 | Ti-2 | Ti-3 | Ti-0 | Ti-1 | Ti-2 | Ti-3 |
| Al | 92.53 | 92.68 | 92.8 | 92.7 | 92.64 | 92.56 | 92.63 | 92.95 |
| Si | 7.05 | 6.84 | 6.71 | 6.8 | 6.95 | 6.96 | 6.86 | 6.51 |
| Mg | 0.27 | 0.26 | 0.25 | 0.25 | 0.25 | 0.25 | 0.24 | 0.23 |
| Sr | 0 | 0 | 0 | 0 | 0.022 | 0.02 | 0.02 | 0.02 |
| Ti | 0 | 0.07 | 0.11 | 0.14 | 0 | 0.06 | 0.1 | 0.14 |
| Fe | 0.09 | 0.09 | 0.09 | 0.09 | 0.09 | 0.1 | 0.09 | 0.1 |

Aluminum A356 cast alloy microstructure consists of the primary Al-matrix in the form of dendritic structures, eutectic Si phase particles (Si particles), minimal traces of Fe-rich intermetallic phases and pores (shrinkage and hydrogen porosity). Figure 4-1 (a-b) shows a typical microstructure of an as-cast unmodified A356 Ti-0 alloy at two different magnifications, 50X and 500X respectively.

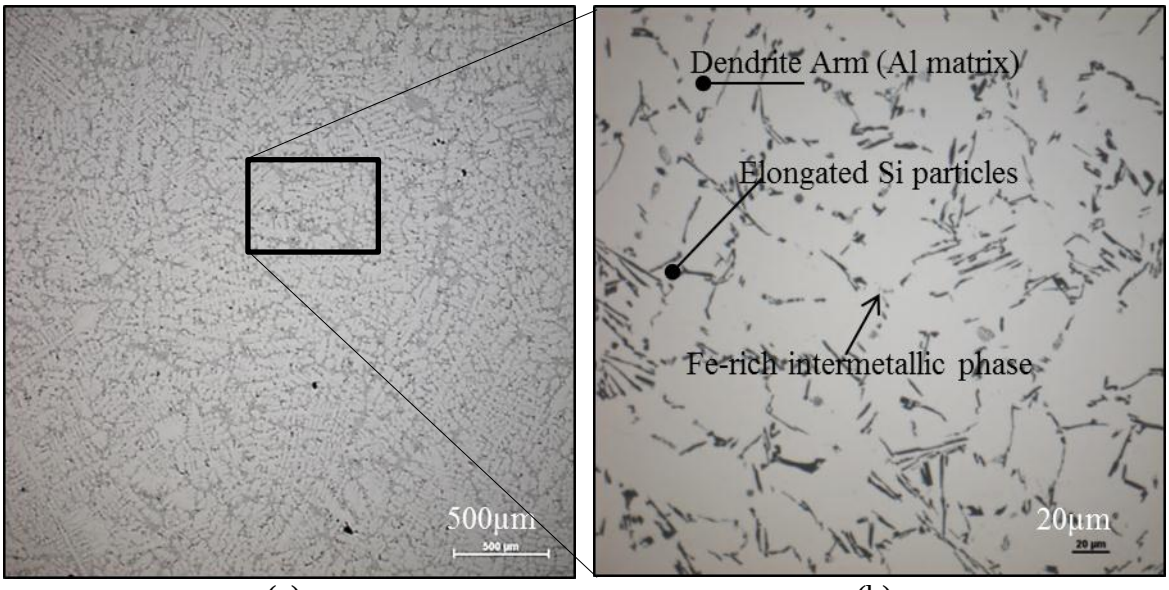


(a) (b)

Figure 4-1. Typical micrographs of as-cast unmodified A356 Ti-0, (a) 50X, and (b) 500X.

Figure 4-1 (a) shows the typical dendritic structure of the Al-matrix with an average secondary dendritic arm spacing (SDAS) of 25.6 μm. The figure also reveals the dendrites surrounded by Si particles and only a few pores are present throughout the specimen surface. Figure 4-1 (b) shows the eutectic Si phase particle distribution revealing the plate-like morphology of the Si phase. In addition, there are minor traces of the Fe-rich intermetallic phases as well. The T4 heat treatment, as observed in Figure 4-2 (a-b), results in spherodization of the Si particles for this alloy where some particles have become round and the elongated particles have round edges as opposed to the sharp edges of the Si particles in the as-cast state. Also the Fe-rich intermetallic phases are scattered throughout the cast structure as opposed to the small clusters revealed in Figure 4-1 (b) in the as-cast alloy.

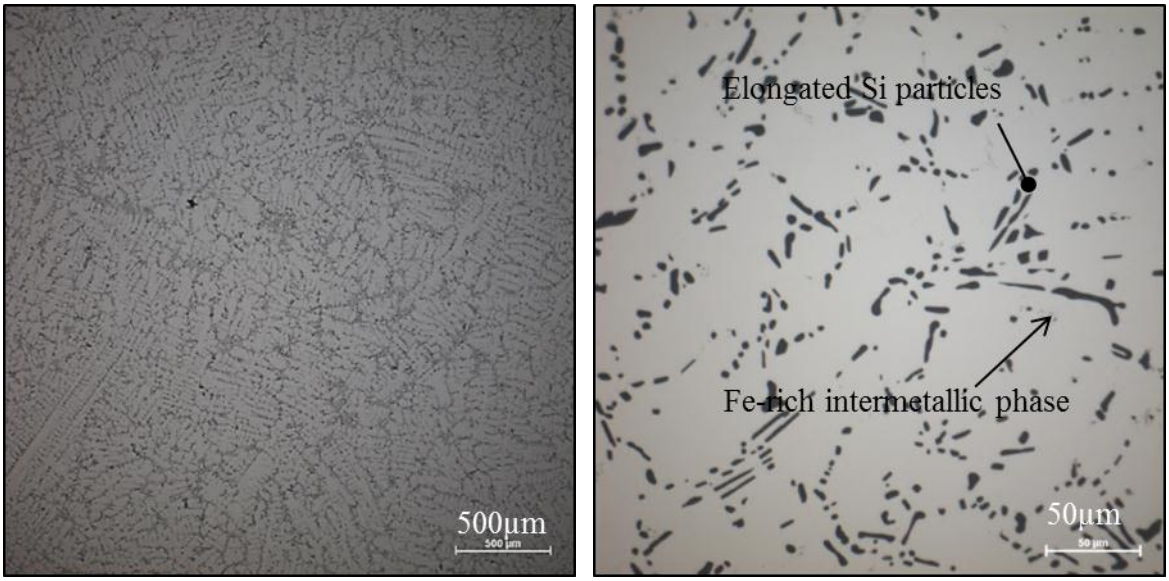


(a) (b)

Figure 4-2. Typical micrographs of the unmodified A356-T4 Ti-0, (a) 50X, and (b) 500X.

The effect of modifying the alloy using Sr is shown in the as-cast state and T4 temper in Figures 4-3 and 4-4, respectively.

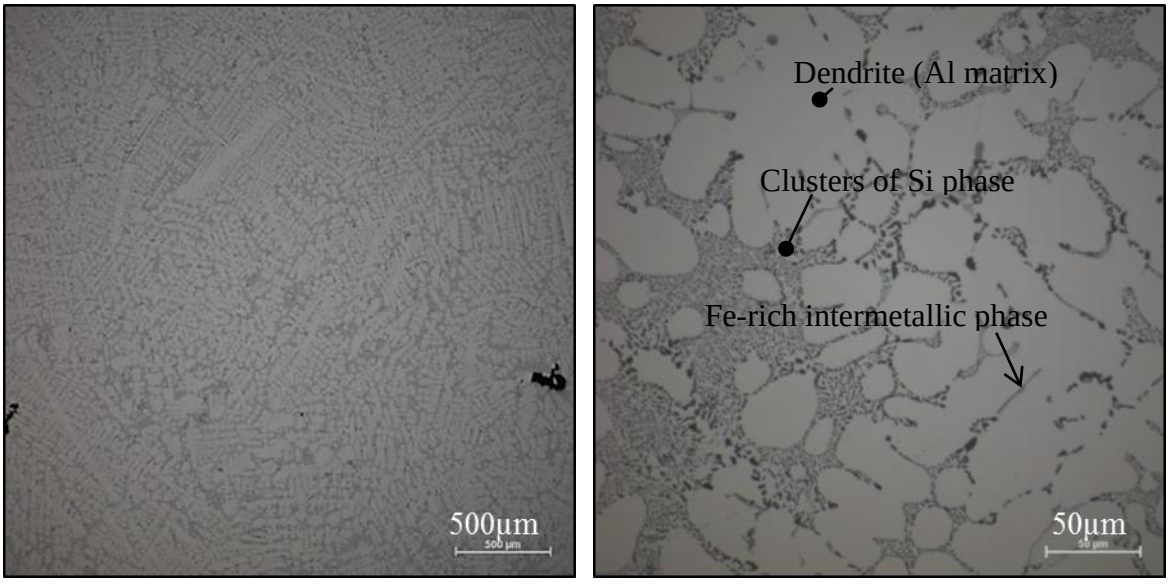


(a) (b)

Figure 4-3. Typical micrographs of as-cast Sr-modified and 0% Ti A356 cast alloy, (a) 50X, and (b) 500X.

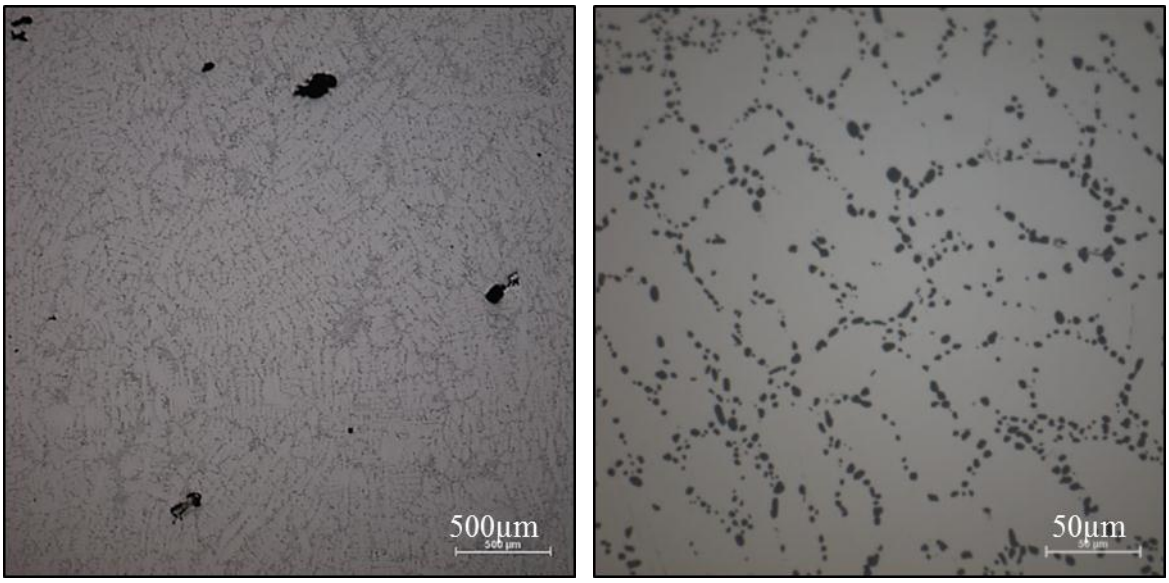


(a) (b)

Figure 4-4. Typical micrographs of Sr-modified Ti-0 A356-T4 cast alloy, (a) 50X, and (b) 500X.

Figure 4-3 (a) shows the typical dendritic structure of the Al-matrix with an average secondary dendritic arm spacing (SDAS) of 23 µm and the existence of larger pores as compared to the unmodified alloy. Figure 4-3 (b) shows a more detailed microstructure,

where extremely fine Si particles appear as clusters surrounding the dendrites. In addition, there are minor traces of Fe-rich intermetallic phases. The T4 heat treatment, as observed in Figure 4-4 (a-b), reveals the Al matrix dendritic structure with an average SDAS of 25.6 μm along with a uniform distribution of Si particles throughout the cast as achieved through heat treating. The extremely fine Si phase in the as-cast cast state is coalesced into larger uniformly distributed Si particles. The Fe-rich intermetallic phases are dispersed throughout the microstructure.

Figure 4-5 shows the dendritic structure for the unmodified and Sr-modified Ti-3, respectively. Comparing these micrographs with Figure 4-2 and Figure 4-4 (Ti free alloys), it is to be noted that the addition of Ti and Sr have no appreciable effect on the dendritic structure (SDAS).

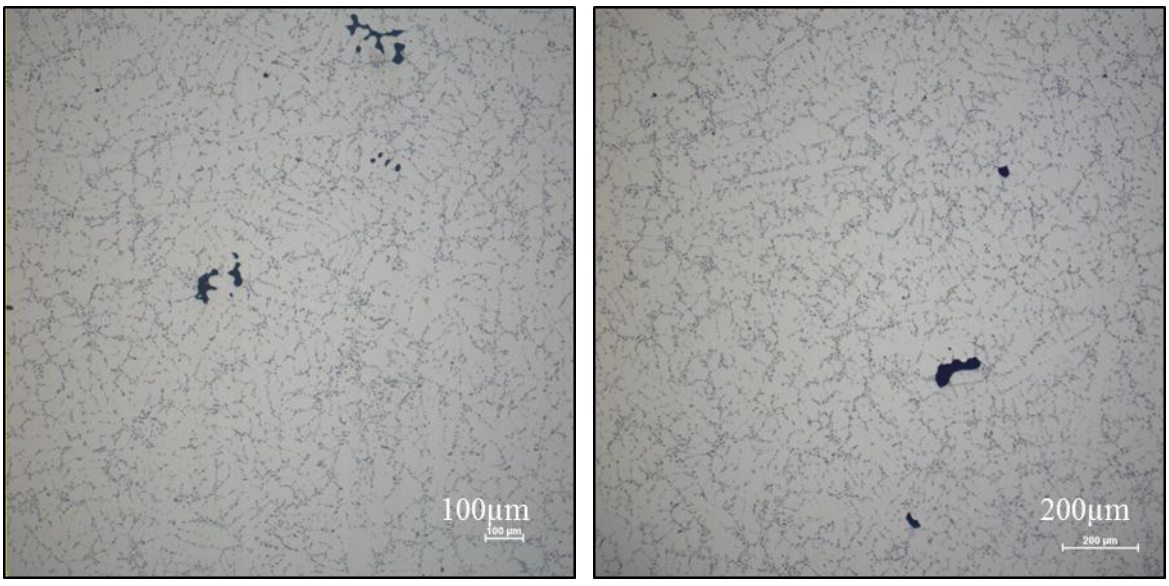


(a) (b)

Figure 4-5. Dendritic cast structure of A356 at 100X for (a) unmodified Ti-3, and (b) Sr-modified Ti-3 alloys.

### 4.1.2 Eutectic Si Phase Particles

Analysis of large magnification (500X) optical micrographs taken for the various casting conditions subjected to T4 Temper (unmodified and Sr-modified alloys at the different Ti levels) were utilized for the analysis of the Si particle size and aspect ratio distribution (see Figure 4-6 (a) and (b)).

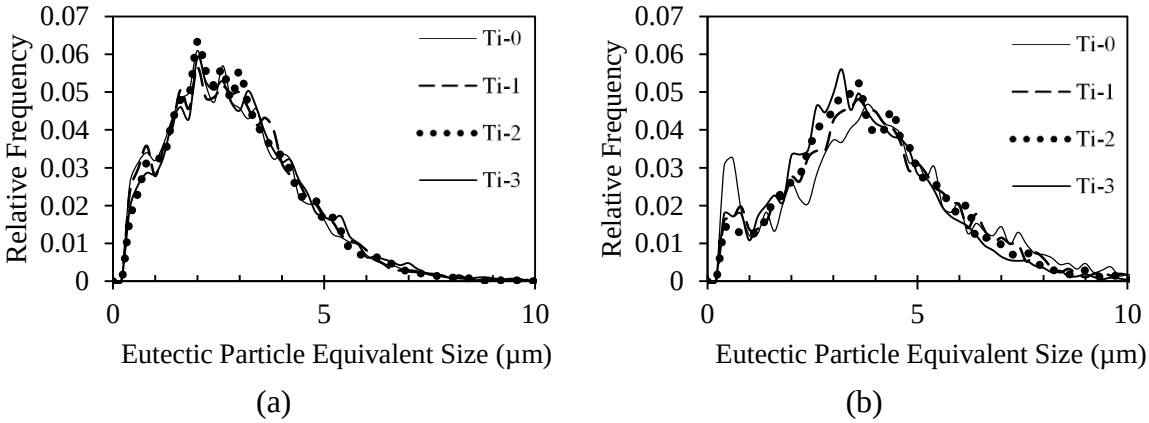


Figure 4-6. Histograms showing the distribution of the particle equivalent circle diameter (μm) of Si phase particles in T4 heat treated alloys, (a) Sr-modified alloy, and (b) unmodified alloy.

Figure 4-6 (a) and (b) shows that Ti has no marked effect on the size distribution (equivalent circle diameter) of the Si phase particles for both the unmodified and Sr-modified alloys, respectively, in the T4 heat treated condition. The size distribution for the Sr modified cast is marginally narrower than that of the unmodified alloy and the average particle size for the Sr modified alloy is finer than that of the unmodified alloy due to the initial refinement of the Si phase morphology in the as-cast condition for the Sr-modified alloy. Figure 4-7 (a) and (b) shows the aspect ratio distribution of the Si phase morphology for both the unmodified and Sr-modified castings with various levels of Ti, respectively for the T4 heat treated condition. Similar to the particle size

distribution, Ti seems to have no effect on the aspect ratio of the Si phase particles. However, Sr modification has a homogenizing effect on the aspect ratio of the particles as indicated by narrower particle aspect ratio band in Figure 4-7(a). This could be attributed to the initial refinement of the Si phase morphology due to Sr addition in the as-cast microstructure shown earlier in Figure 4-3.

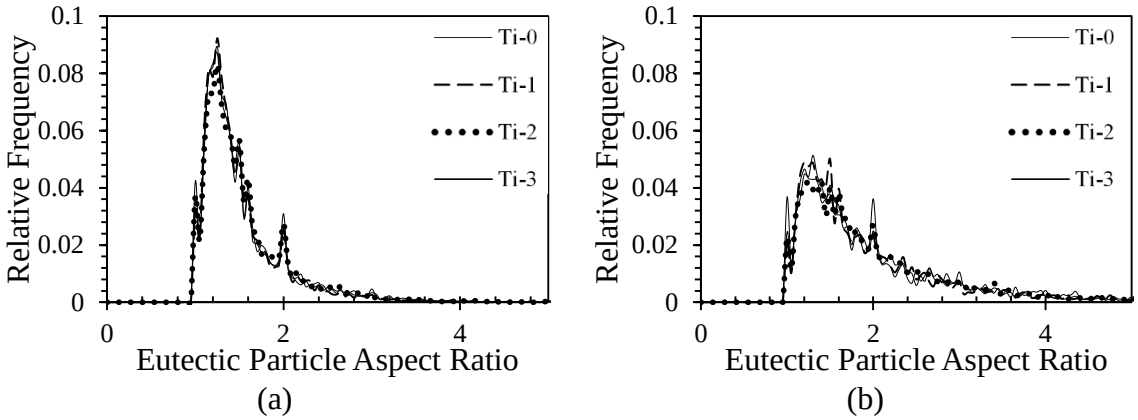


Figure 4-7. Histograms showing the distribution of the eutectic particle aspect ratio, (a) Sr modified alloy, and (b) unmodified alloy.

Figure 4-8 presents a summary of the effect of Sr and Ti on the average size and aspect ratio of the Si phase morphology in the alloys along with their respective 95% confidence interval shown by the dotted lines. Sr addition to the alloy decreases the average size of the particles by about 30% and the average aspect ratio by 26.5% when compared to the unmodified alloy, after T4 heat treatment of the samples. Different levels of Ti additions, on the other hand, have virtually no effect on the particle size and particle aspect ratio. A summary of the eutectic Si phase particles data of the cast alloys is presented in Table 4-2.

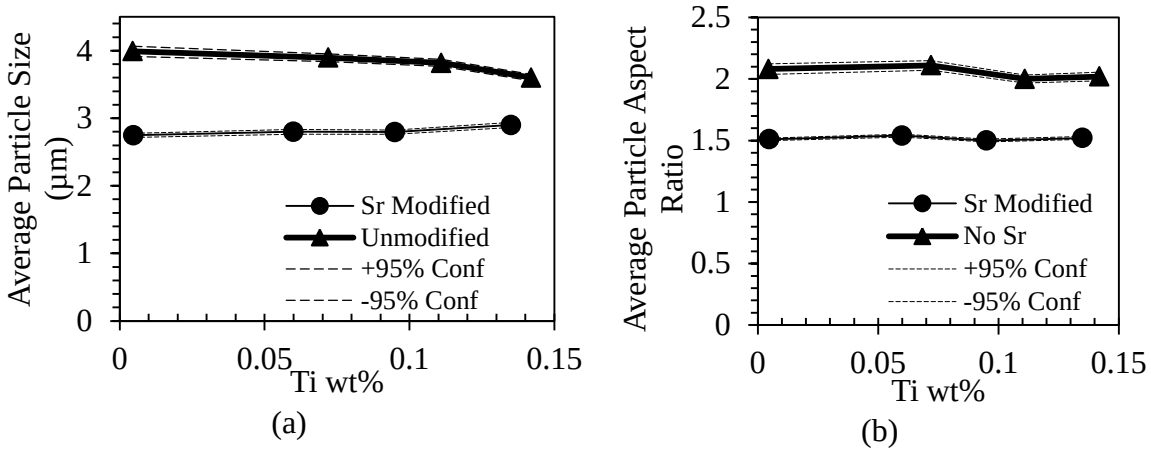


Figure 4-8. Composite plots showing the effect of Ti and Sr on the eutectic Si phase particles in A356 cast alloy subjected to a T4 temper, (a) effect on average particle size, and (b) average particle aspect ratio.

### 4.1.3 Grain Structure

Low magnification (18X) micrographs taken from etched specimen (see Figure 4-9 and Figure 4-10) of the (unmodified and Sr-modified) A356 alloy subjected to T4 temper were utilized for the analysis of the grain size and grain aspect ratio distributions. Typical results from this analysis are shown in Figure 4-11 for the unmodified and Sr-modified alloys, respectively, both with the Ti-0 condition. Figure 4-12 shows the effect of Ti additions on the grain size distribution for the Sr-modified and unmodified alloys.

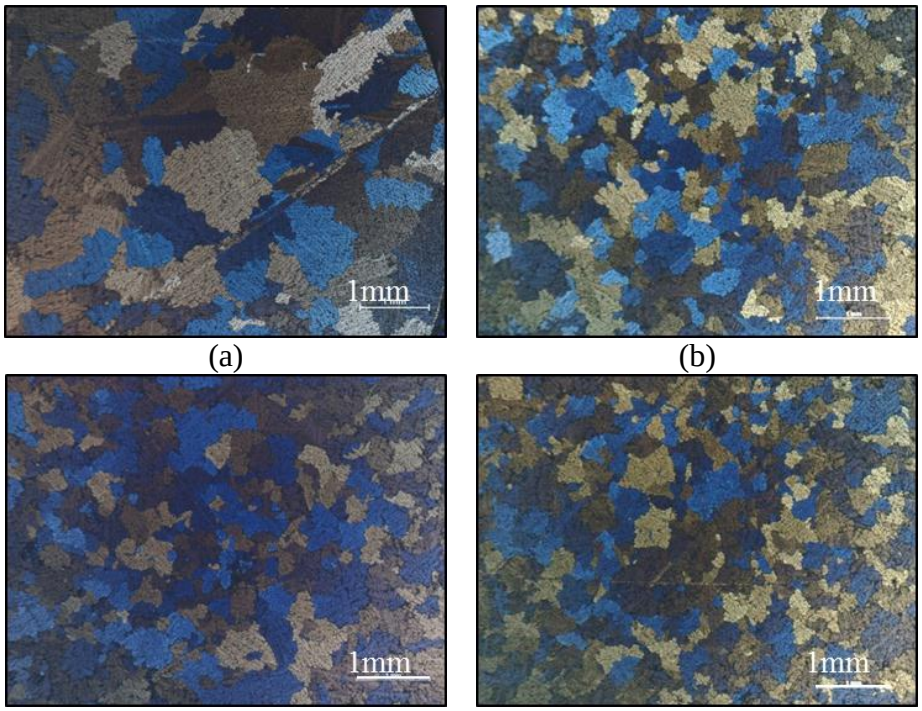


(a) (b)

(c) (d)

Figure 4-9. Grain structure of the unmodified A356 alloys, (a) Ti-0, (b) Ti-1, (c) Ti-2, and (d) Ti-3.

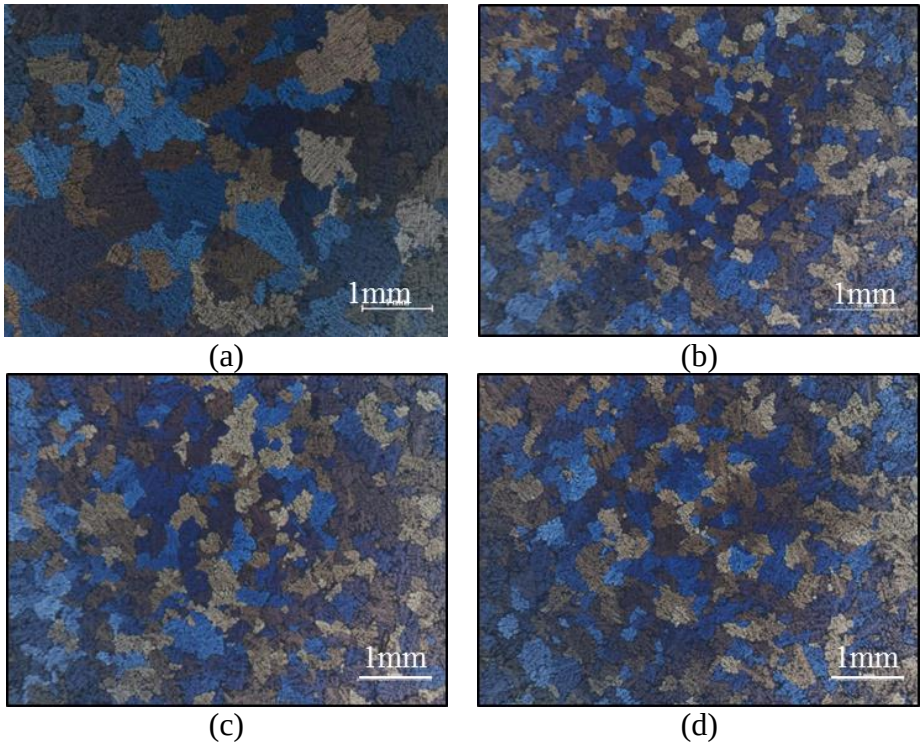


(a) (b)

(c) (d)

Figure 4-10. Grain structure of the Sr-modified A356 alloys, (a) Ti-0, (b) Ti-1, (c) Ti-2, and (d) Ti-3.

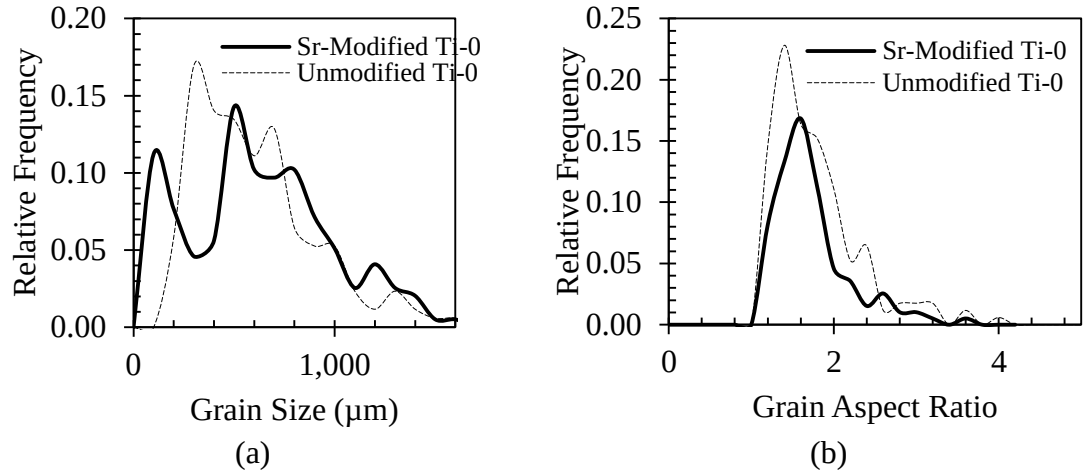


Figure 4-11. Histogram showing the distribution of the (a) equivalent grain size and (b) aspect ratio for A356-T4 Ti-0.

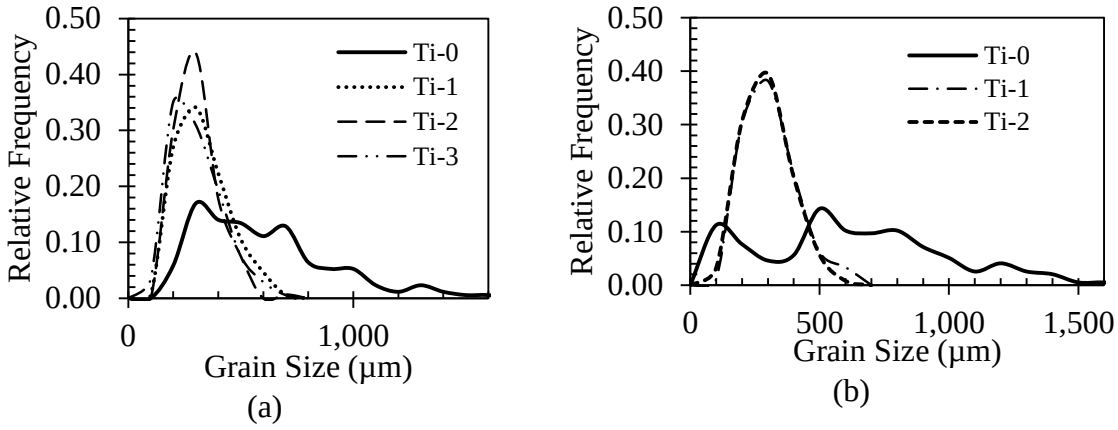


Figure 4-12. Comparison of grain size distribution for different levels of Ti, (a) unmodified, and (b) Sr-modified alloy.

The data shows that the Sr-modified alloy has a very similar grain size distribution compared to the unmodified alloy. In terms of grain aspect ratio distribution, Sr addition has a negligible effect. Figure 4-13 shows the results for the average grain size and average grain aspect ratio for entire set of cast alloys. The results show that Ti refining effect is only prevalent at very low Ti amounts, and as Ti increases in the alloy the grain size does not show any appreciable change. Ti additions have no appreciable effect on the

grain aspect ratio. A summary of the grain structure data of the cast alloys is presented in Table 4-2.

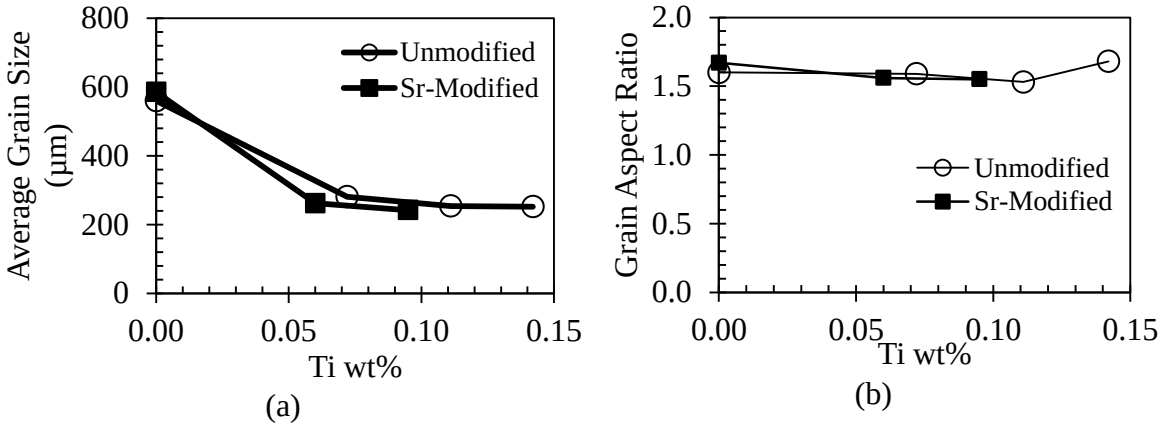


Figure 4-13. Composite plots showing the effect of Ti and Sr on the grain structure of A356 cast alloy subjected to a T4 temper, (a) effect on average grain size, and (b) average grain aspect ratio.

The grain refining effect of Ti on the A356 cast alloy is evident from Figure 4-13 where the refining effect shows to be saturated at a level of Ti above 0.05 wt%. The results agree with those reported in the literature [12] [14] [13]. Ti addition did not exhibit any effect on the eutectic Si phase particle morphology in unmodified and Sr-modified alloys (see Figure 4-6 and Figure 4-7).

### 4.1.4 Porosity

Figure 4-14 and Figure 4-15 show low magnification (7X) micrographs taken for the various cast compositions (unmodified and Sr-modified alloys at the different Ti levels) subjected to T4 Temper. The resulting microstructures were utilized for the analysis of average pore size, average pore aspect ratio and pore area fraction (see Figure 4-16 (a-c)). The Figure 4-14, Figure 4-15 and Figure 4-16 (a) show that the unmodified A356 has a significantly lower average pore size compared to the Sr-modified alloy. However,

Figure 4-16 (b) shows that the morphology of the pores has no appreciable change due to Sr addition to the alloy. Additionally, Figure 4-14 and Figure 4-15 show that increasing levels of Ti additions to the alloys, with and without Sr, increases the number of pores in the sample, while there is no appreciable change in the size of these pores. The porosity observed in Figure 4-14 and Figure 4-15 is predominantly gas porosity caused by the release and entrapment of hydrogen gas during solidification of the alloys. A summary of the porosity of the cast alloys is presented in Table 4-2. Addition of Sr to the alloy results in an increased levels of hydrogen dissolved in the alloy when compared to the unmodified alloy, and this leads to increased size of average porosity [19]. Further, Sr addition to the alloy changes the viscosity and surface tension of the solidifying liquid and results in an increased nucleation of gas porosity in the interdendritic region during solidification as shown by the work done by Emadi et al. [18]. The authors were investigating the effect of Na and Sr modification on surface tension and volumetric shrinkage in A356 alloy and their consequent effect on porosity formation. Their investigation showed that modification of alloy results in a decrease in the surface tension and increase in volumetric shrinkage. The surface tension and volumetric shrinkage alterations assist in the porosity formation, which results in larger pores. Other studies carried out by Shivkumar et al. [69] and Lashgari et al. [70] on A319 and A356-10%$B_4C$ castings, respectively, showed that pore fraction area (%) increased when the cast was subjected to Sr- modification. On the other hand, Dinnis et al. [71] shows contradicting results where the authors work claims that porosity size (pore diameter) and the amount of porosity was decreased due to the addition of Sr.

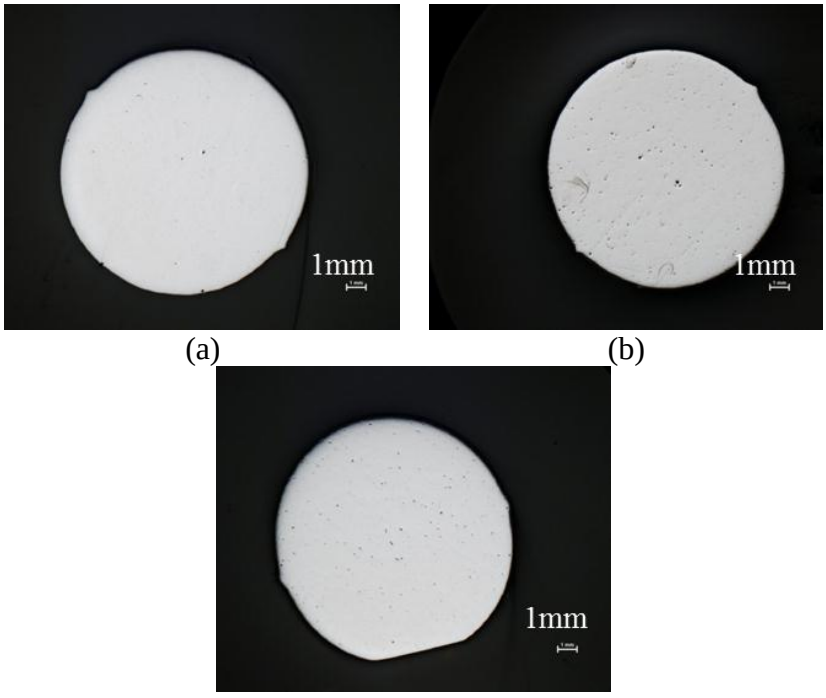


(a) (b)

(c)

Figure 4-14. Porosity content of the unmodified A356 alloys, (a) Ti-0, (b) Ti-1, (c) Ti-2, and (d) Ti-3.

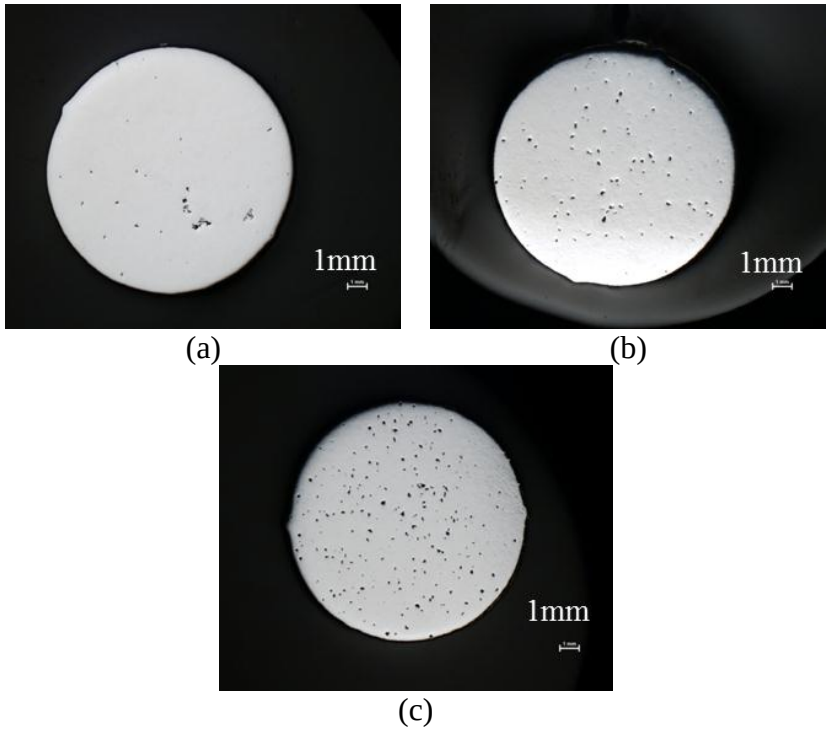


(a) (b)

(c)

Figure 4-15. Porosity content of the Sr-modified A356 alloys (a) Ti-0, (b) Ti-1, and (c) Ti-3.

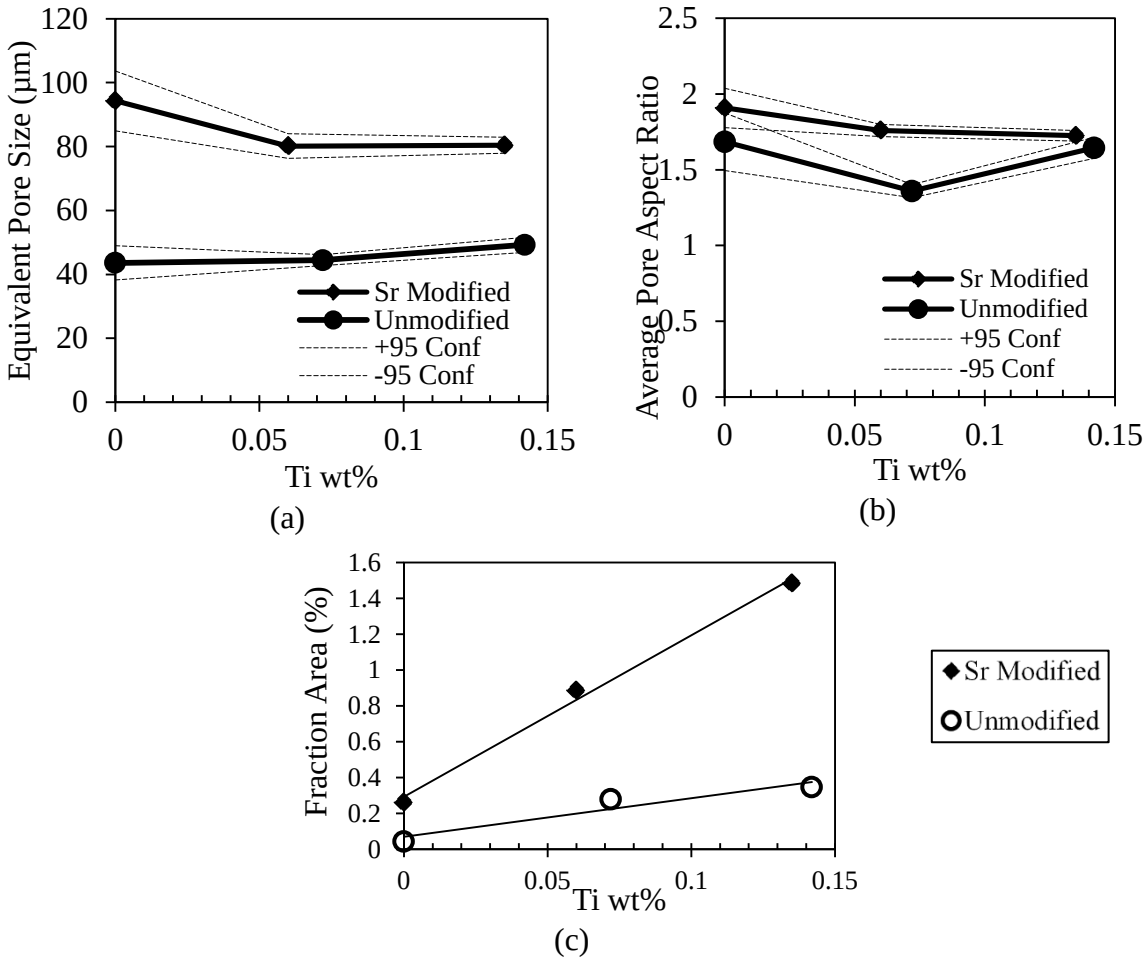


Figure 4-16. Composite plots showing the effect of Ti and Sr on porosity, (a) effect on equivalent pore size, (b) pore aspect ratio, and (c) pore area fraction.

Ti addition to the alloys induces grain refinement of the primary Al phase during solidification as observed in Figure 4-13 (a). Grain refinement leads to a significant increase in the surface area of the growing solid/liquid interface during solidification, which in these alloys would be an increased area of Al dendrite in contact with the solidifying liquid. This presents a significantly more favorable environment for the nucleation and growth of gas porosity in the sample resulting in a higher pore fraction area in the sample. However, Figure 4-16 (a) and (b) show that there was no appreciable change in the pore size and aspect ratio with increased levels of Ti in both the Sr-

modified and unmodified alloys. In contrast, there was a significant increase in volume fraction of pores in the microstructure for both the unmodified and Sr-modified alloys with increasing levels of Ti, as shown in Figure 4-16 (c). This can not be explained by the increased surface area of the Al dendrites due to Ti additions to the alloy because with the larger distribution of the porosity, the size of the pores should have decreased while the total volume fraction of porosity should have remained unchanged. Hence, the results in Figure 4-16 (a) to (c) show that there is an increase in the levels of hydrogen gas dissolved in the interdendritic liquid during solidification and this coupled with the increased surface area of Al dendrites caused by grain refinement would lead to the observed results on Ti additions on porosity. There seem to be no reported observation in the literature on the effect of grain refinement by Ti additions and the resultant levels of gas porosity in the solidified alloy. The results from this work will warrant an in-depth research on this salient topic.

### 4.1.5 Summary of Metallographic Analysis

The results of quantitative microstructural analysis for alloy samples discussed in this section are summarized in Table 4-2. The results of the metallographic analysis show that Sr and Ti additions cause significant change to the porosity in the cast and heat treated alloy samples (increase in size and distribution of pores). All the three levels of Ti addition results in the same level of grain refinement, however, increasing the Ti levels cause an increase in the porosity levels in the casting. Hence, for further analysis of the tensile, compression and V-bending tests, the unmodified and Sr-modified Ti-free alloys (Ti-0) were chosen along with the unmodified alloy with 0.15wt% Ti (Ti-3) for further

analysis. The addition of Ti did not have any appreciable difference in the microstructure between unmodified and Sr-modified alloys, or in other words, there is no appreciable interaction between Sr and Ti additions to the alloy.

Result from the metallographic analysis indicates a strong correlation between Ti additions to the alloy and porosity levels in the solidified samples. It is recommended that further in-depth work be carried out to elucidate and quantify this interaction.

Table 4-2. Summary of microstructural analysis for both unmodified and Sr-modified alloys with the various levels of Ti.

| | | Unmodified | | | | Sr-Modified | | | |
|---|---|---|---|---|---|---|---|---|---|
| Ti Level | | Ti-0 | Ti-1 | Ti-2 | Ti-3 | Ti-0 | Ti-1 | Ti-2 | Ti-3 |
| Dendrite | Average SDAS (µm) | 26.5 | 26.7 | 26.7 | 26.25 | 25.6 | 24.6 | 27.9 | 25.8 |
| | SDAS St. Deviation (µm) | 6 | 7.23 | 6.2 | 6.4 | 6.1 | 5.5 | 7.2 | 5.8 |
| Eutectic Si Phase | Average Size (µm) | 4 | 3.9 | 3.82 | 3.6 | 2.77 | 2.8 | 2.8 | 2.9 |
| | Size St. Deviation (µm) | 2.2 | 2.01 | 1.88 | 1.79 | 1.57 | 1.57 | 1.51 | 1.63 |
| | Average Circularity (%) | 79.2 | 78.6 | 80.5 | 80.6 | 88.4 | 88.3 | 89.1 | 88.3 |
| | Circularity St. Deviation | 19 | 19 | 18.3 | 18.2 | 15.34 | 14.2 | 14.1 | 14.5 |
| | Average Aspect Ratio | 2.09 | 2.11 | 2.01 | 2.02 | 1.51 | 1.54 | 1.5 | 1.52 |
| | Aspect Ratio St. Deviation | 1.3 | 1.34 | 1.19 | 1.29 | 0.53 | 0.59 | 0.54 | 0.56 |
| Grain | Average Size (µm) | 560 | 281 | 254 | 252 | 585 | 262 | 242 | |
| | Size St. Deviation (µm) | 283 | 114 | 96 | 112 | 316 | 100 | 97 | |
| | Average Aspect Ratio | 1.67 | 1.59 | 1.53 | 1.68 | 1.67 | 1.56 | 1.55 | |
| | Aspect Ratio St. Deviation | 0.48 | 0.43 | 0.35 | 0.52 | 0.45 | 0.4 | 0.36 | |
| Porosity | Average Size (µm) | 43.6 | 44.45 | | 49.28 | 94.3 | 80.16 | | 80.39 |
| | Size St. Deviation (µm) | 29.9 | 24.46 | | 27.8 | 58.7 | 43.93 | | 43.4 |
| | Average Aspect Ratio | 1.69 | 1.36 | | 1.65 | 1.91 | 1.76 | | 1.725 |
| | Aspect Ratio St. Deviation | 1.11 | 0.65 | | 0.846 | 0.82 | 0.6 | | 0.63 |
| | Fraction Area (%) | 0.043 | 0.28 | | 0.35 | 0.26 | 0.89 | | 1.48 |

## 4.2 Deformation Characteristics in Tensile Loading

This section presents the results of tensile testing and analysis of the T4 heat treated alloys. The cast condition is of no significant interest to this study because of the low ductility in the as-cast condition, which does not present an opportunity to understand the interaction of microstructure features with plastic deformation. This reasoning could also be extended to explain the lack of the study of the T6 heat treated condition, as well.

### 4.2.1 Overview

The results of uniaxial tensile testing of round dog-bone tensile specimen for 8 different chemical compositions are shown in Figures 4-17, 4-18 and 4-19. All tests were conducted at a cross-head speed of 1.7 $mm.min^{-1}$. The stress strain curves for unmodified and Sr-modified Ti-0 A356 (see Figure 4-17) show that Sr enhances the materials ductility, whereas the strength is slightly reduced. Sr modification reduces the average yield strength (YS) (0.2% proof stress) from 125 to 115 MPa while increasing the global strain (elongation) at fracture by about 26%. The unmodified alloy Ti-1 yielded higher levels of global strain compared to Ti-0 with no apparent change in the work hardening behavior of the alloy (i.e., shape of the plastic region of the curve) (Figure 4-18). However, further increase in Ti levels (Ti-2 and Ti-3) did not affect the nature of the stress-strain curves. Further, Figure 4-18 shows that addition of Ti to the unmodified alloy marginally increases the strength (YS and fracture stress (FS)), but the increase is nearly the same for all the three levels of Ti addition. There is an increase in elongation from the unmodified alloy with addition of Ti, but there is no change in this increase with the three levels of Ti. For the Sr-modified alloy at different levels of Ti showed no

significant effect on the stress-strain curves except that addition of Ti marginally increases the YS and fracture strain while marginally decreasing the elongation (see Figure 4-19). Thus, the effect of Sr is more dominant on the stress-strain curves of the A356 alloy than that of Ti additions, and there is no significant interaction between Ti and Sr additions to the alloy.

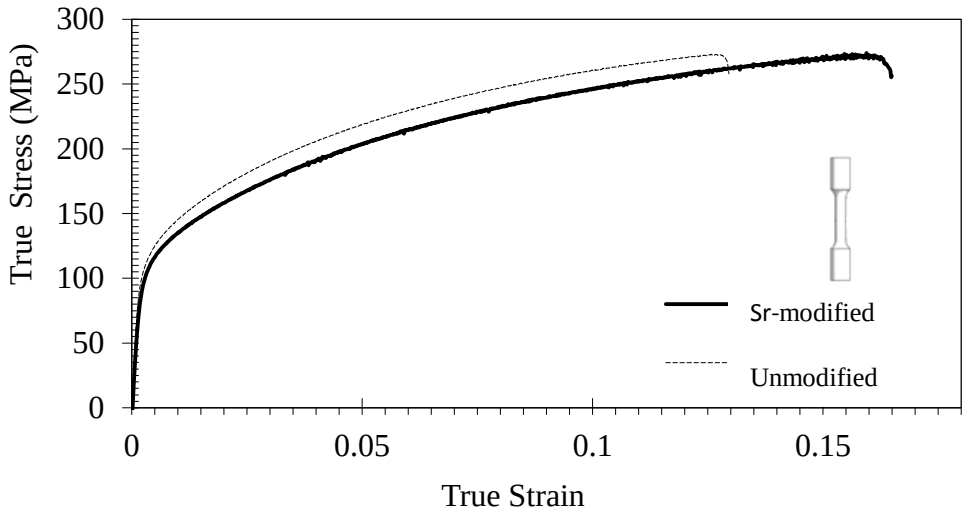


Figure 4-17. Stress strain curves of Ti-0 Sr-modified and unmodified A356.

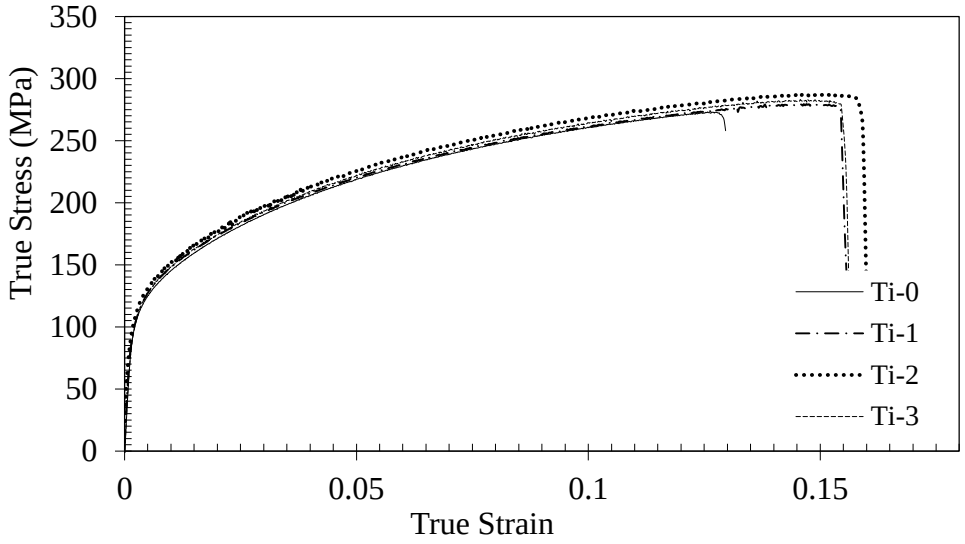


Figure 4-18. Stress strain curves of unmodified A356 Al cast alloy with multiple Ti levels.

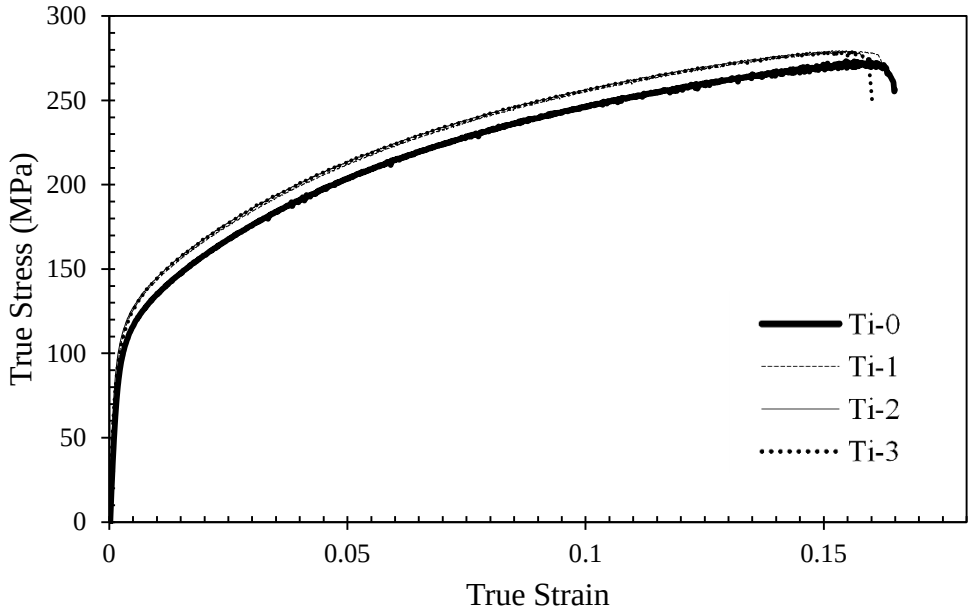


Figure 4-19. Stress strain curves of Sr-modified A356 alloy with multiple Ti levels.

Figure 4-20 shows the tensile results for specimen machined flat from the round bars where stress-strain curves are presented for the three chosen cast compositions: *unmodified Ti-0, unmodified Ti-3 and Sr-modified Ti-0*. These three alloys were chosen for further mechanical tests because they show significant variations in the YS, FS and elongation among the set of alloys cast and further, these three alloys compositions show significant variations in the microstructure features such as grain size, Si phase particle size and morphology, and porosity levels, as discussed in the previous section on metallographic analysis. A summary of material parameters obtained from the stress-strains curves for the materials are shown in Figure 4-21. The results reveal that Sr-modified alloy has the highest strain hardening exponent, elongation and FS and the lowest YS. On the other hand, the unmodified alloy has the lowest strain hardening exponent, elongation and FS. The unmodified Ti-3 alloy showed the highest YS as expected.

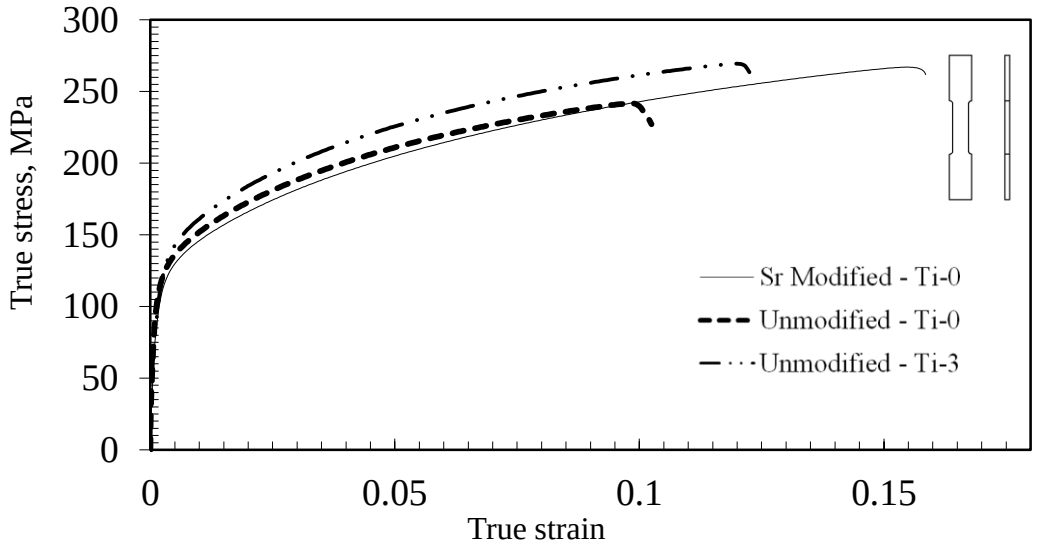


Figure 4-20. Stress strain curves using flat dog-boned tensile specimen o three different cast compositions, Sr-modified Ti-0, unmodified Ti-0 and unmodified Ti-3.

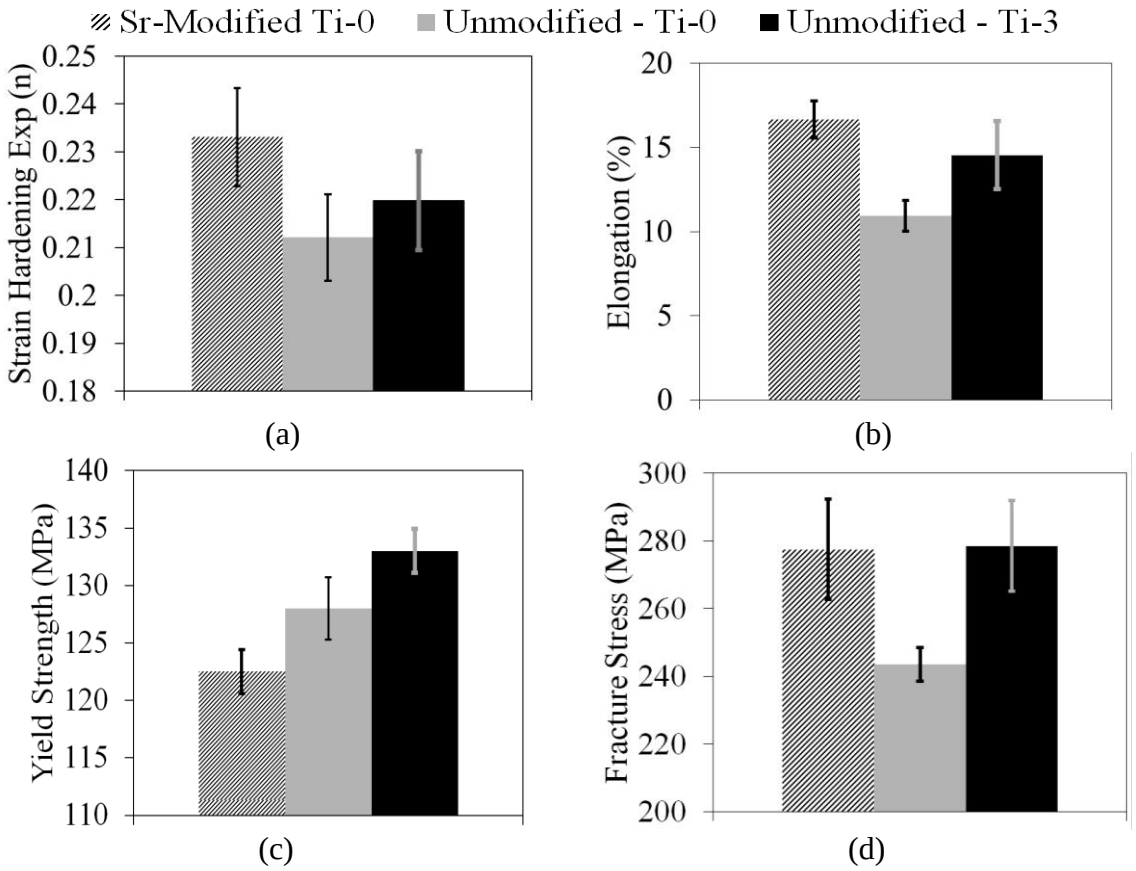


Figure 4-21. Material parameters from the stress-strain curves for the Sr-modified Ti-0, unmodified Ti-0 and unmodified Ti-3. (a) Strain hardening exponent (n), (b) elongation, (c) yield strength and (d) fracture stress.

### 4.2.2 Surface Strain Mapping

Figure 4-22 (a-f) shows typical micrographs of the gage section of three tensile specimen prior to testing, (a) and (d) Sr-modified Ti-0, (b and e) unmodified Ti-0, and (c and f) unmodified Ti-level 3. Figure 4-22 (a-c) are micrographs taken from polished specimen revealing the phase distribution whereas Figure 4-22 (d-f) are micrographs from etched specimens revealing the grain structure.

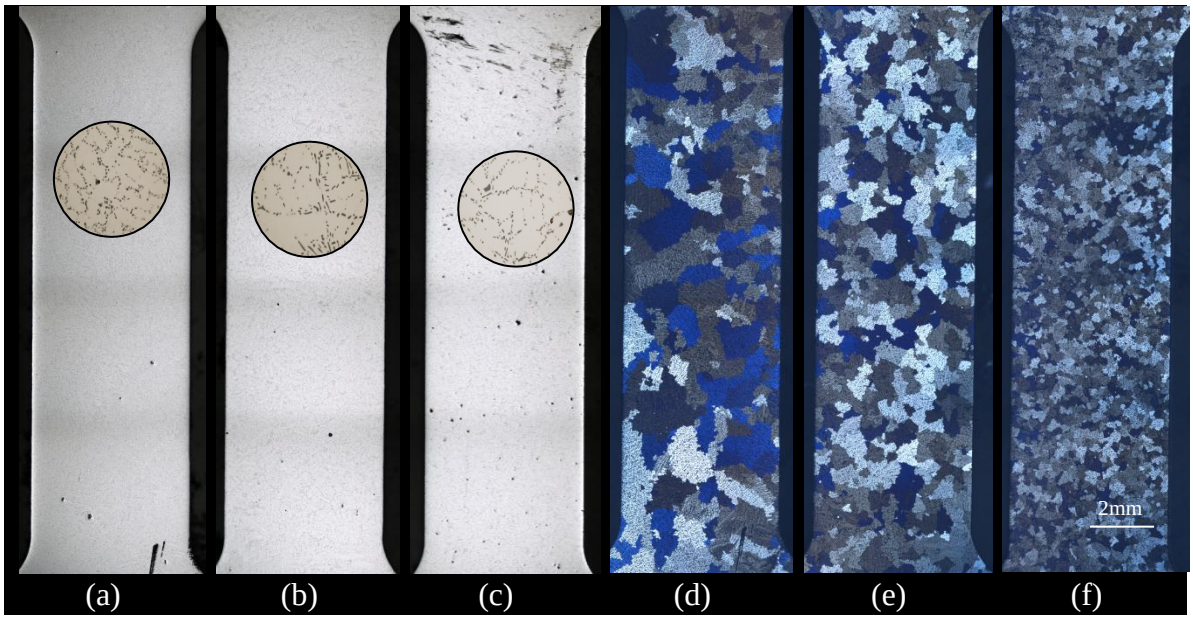


Figure 4-22. Typical micrographs from the gage section of tensile specimen prior to testing (a-c) Si phase and porosity characteristics, and (d-f) the grain structure. The micrographs are taken from different alloy compositions (a) and (d) Sr-modified Ti-0, (b) and (e) unmodified Ti-0, and (c) and (f) unmodified Ti-3.

The Aramis strain maps were obtained from the samples shown in Figure 4-22. These are presented in Figure 4-23 and 4-24 at 5% and 10% global strains, respectively. The maps show that the local axial strain in the Sr-modified and unmodified Ti-0 alloy develop heterogeneously, as opposed to the unmodified Ti-3. At 10% global strain (Figure 4-24) the three maps show strain localization in the vicinity of fracture that exhibits very large strains as compared to the rest of the specimen surface.

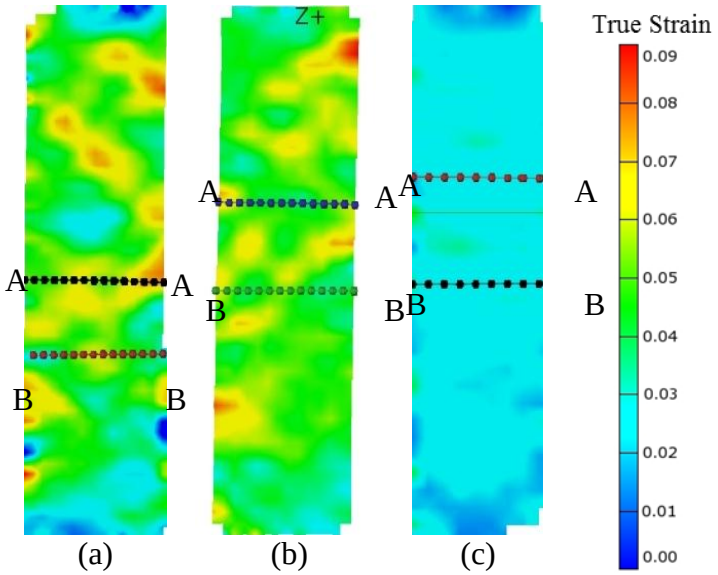


Figure 4-23. Strain maps from tensile specimen deformed at 5% axial strain, (a) Sr-modified Ti-0, (b) unmodified Ti-0 and (c) unmodified Ti-3.

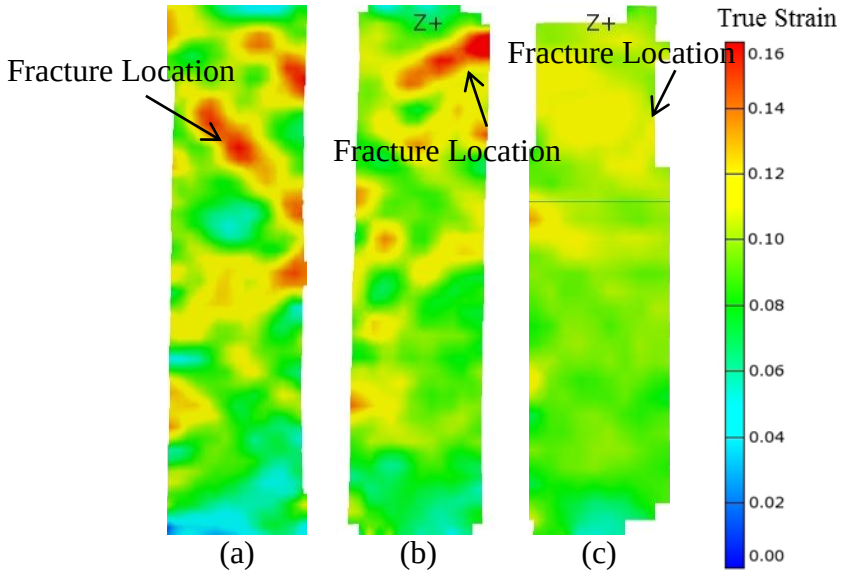


Figure 4-24. Strain maps from tensile specimen deformed at 10% axial strain, (a) Sr-modified Ti-0, (b) unmodified Ti-0 and (c) unmodified Ti-3.

To visualize the difference between the specimens, two arbitrary sections (A-A and B-B as seen in Figure 4-23) were taken across the specimen width for each composition and utilized to plot Figure 4-25 to Figure 4-27. For the Sr-modified and unmodified Ti-0 alloys the strain develops inhomogeneously early on in the deformation process, whereas

the unmodified Ti-3 alloy shows the development of a relatively more uniform strain up to 10% global axial strain.

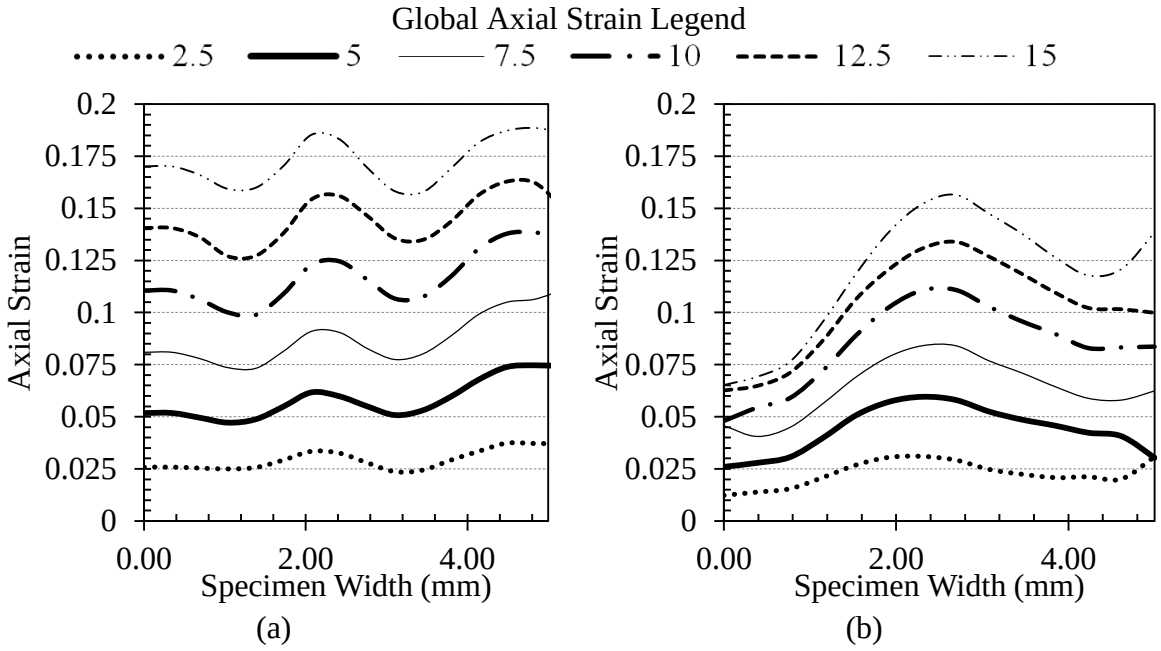


Figure 4-25. Strain distribution across a Sr-modified Ti-0 tensile specimen width at various axial strains, (a) section A-A and (b) section B-B (refer to Figure 4-23 (a)).

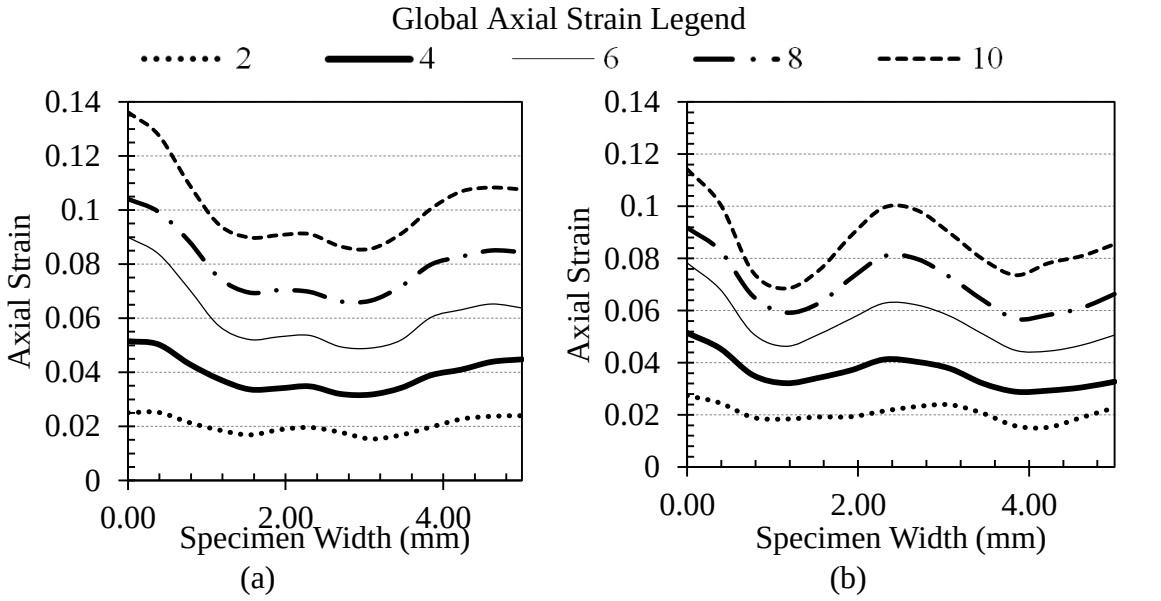


Figure 4-26. Strain distribution across an unmodified Ti-0 tensile specimen width at various axial strains, (a) section A-A and (b) section B-B (refer to Figure 4-23 (b)).

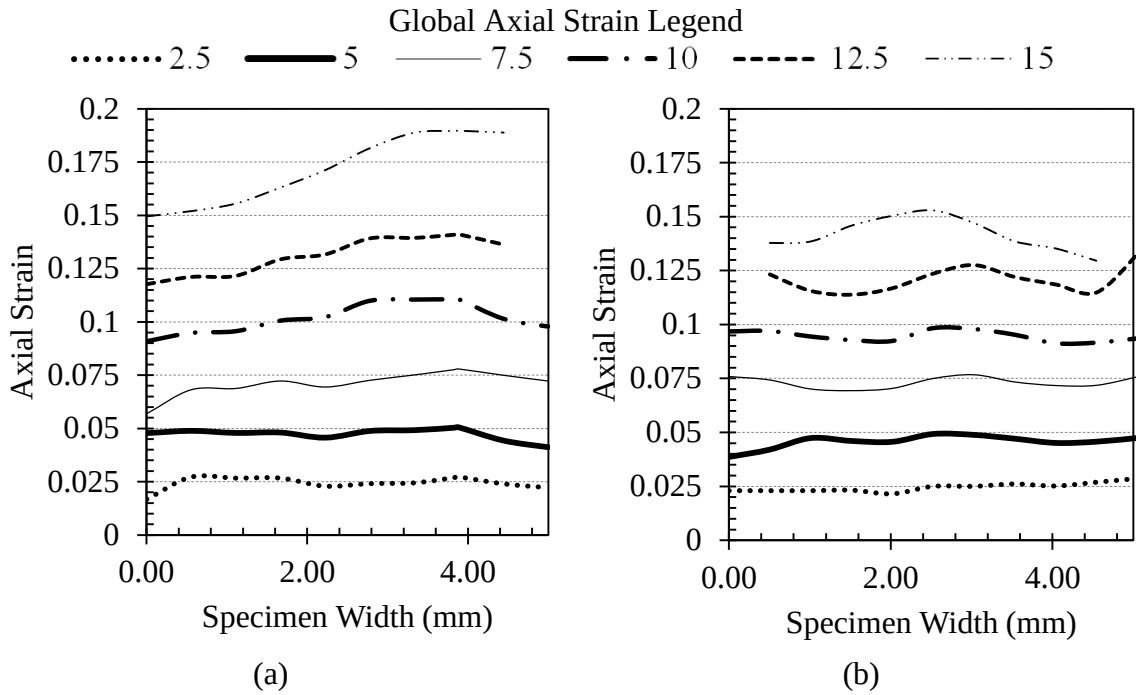


Figure 4-27. Strain distribution across an unmodified Ti-3 tensile specimen width at various axial strains, (a) section A-A and (b) section B-B (refer to Figure 4-23 (c)).

Figure 4-22 to Figure 4-27 show that the strain mapping techniques is capable of detecting strain localization due to grain interactions. The usage of a more enhanced resolution image capturing system would in return enhance the quality of these strain maps and would facilitate the correlation between the microstructure of the strain maps. With a more enhanced strain map, one could pin-point the aspects of the microstructure that induces inhomogeneous deformation. Results shown by [57] [43] reveal strain maps that show strain variation at a sub-grain level. The authors used a high resolution CCD cameras and an optical microscope, respectively indicating that the quality of the strain maps shown Figure 4-23 and Figure 4-24 could be enhanced if a high resolution CCD camera was used.

### 4.2.3 Damage Quantification

The Sr-modified alloy at Ti-0 level had the most porosity among the three alloys evaluated (see Figure 4-16) and hence this sample was used for damage quantification studies to understand the role of porosity on the dynamic deformation of the sample during uni-axial tensile loading. Figure 4-28 (a-d) shows composite micrographs made up of 32 micrographs taken at 40X magnification for a deformed Sr-modified Ti-0 alloy tensile specimen showing the deformation progression in the specimen at 0%, 1.4%, 5.2% and 12.3% global true strain, respectively. The specimen had an initial void volume fraction of 0.289% (Figure 4-28 (a)). The micrographs reveal evident surface roughening as the tensile specimen deforms. The specimen surface roughening is discussed in sub-section 4.2.4. Figure 4-29 (b) shows a detailed micrograph (400X) of the region demarcated by a square in Figure 4-28 (b). By comparing this region to its corresponding location in Figure 4-28 (a), it appears that a new void has formed due to 1.4% of strain. However, Figure 4-29 (b) shows that the location is subjected to out-of-plane deformation around a cluster of Si phase particles, as opposed to the nucleation of a new void. So, it is to be noted that not all dark regions in Figure 4-28 (b-d) are voids, and the majority represent out-of-plane deformation of the sample during testing. Further, it is to be noted that existing pores do not seem to be affected by the specimen deformation, as the deformation is localized in regions away from the porosity in the specimen. Figure 4-30 shows a plot of the average macro-pore diameter versus axial strain. The pores experience linear growth with an average increase in size of 40% of the original pore diameter at an axial strain of 0.12 and no void coalescence was observed for this strain level. Further analysis of the micrographs in Figure 4-28 (a-d) qualitatively reveal

that the pores elongated in a direction parallel to the uni-axial tensile loading leading to increased pore-sizes with increased strain.

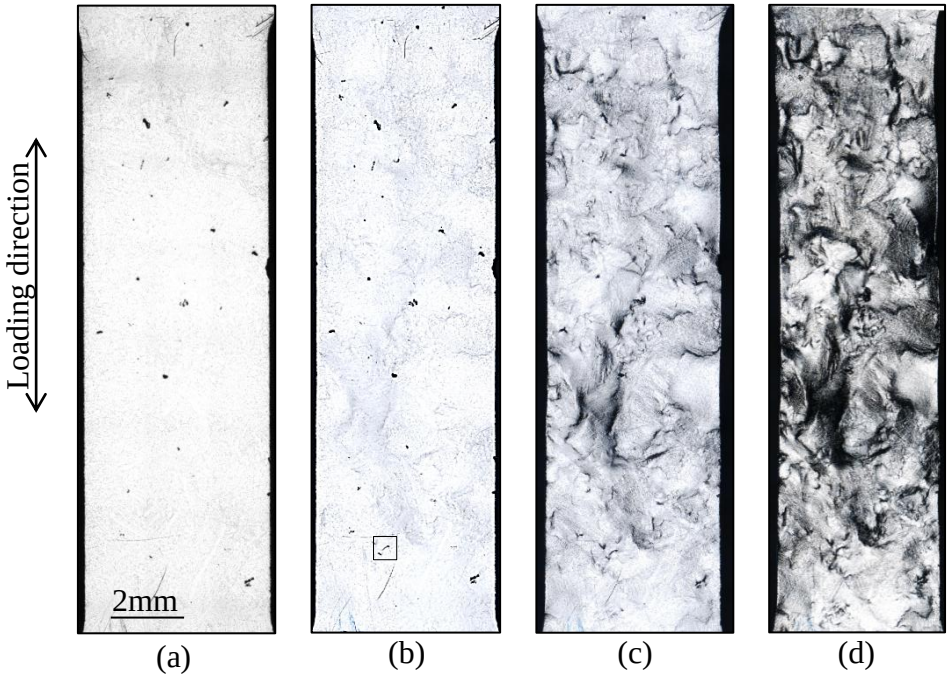


Figure 4-28. Composite micrographs composed of 32 micrographs at 40X recording the deformation of a Sr modified A356 tensile specimen, (a) 0% true strain, (b) 1.4%, (c) 5.2% and (d) 12.3%.

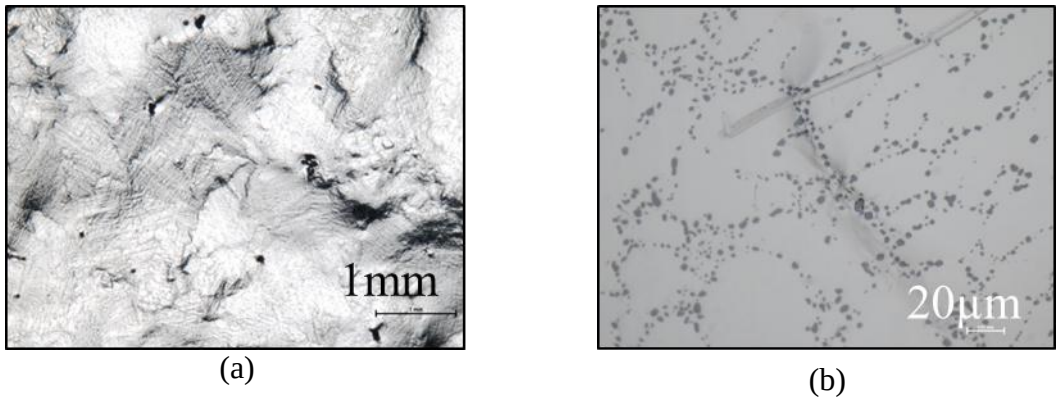


Figure 4-29. Micrograph from deformed Sr-modified Ti-0 tensile specimen at global strain of 1.9, (a) revealing surface roughening (mag. 20X), and (b) micrograph revealing out-of-plane deformation around a cluster of Si phase particles (mag. 400X) (detailed micrograph of marked region shown in Figure 4-28 (b)).

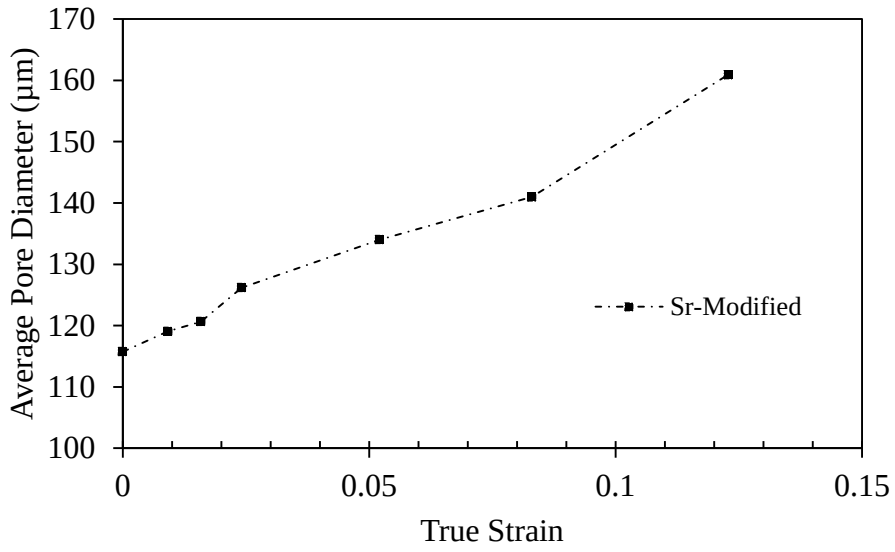


Figure 4-30. Average macro-pore diameter versus global strain for Sr-modified Ti-0 alloy

Figure 4-31 (a) shows a non-linear decrease in the modulus of elasticity as the material deforms for the unmodified Ti-0, unmodified Ti-3 and Sr-modified Ti-0 conditions. A damage parameter (D) (see section 3.4.2) calculated on the basis of change in the modulus of elasticity is presented in Figure 4-31 (b). The results show that this method is not sensitive to capture the differences between the equiaxed and elongated particle damage in the Sr-modified and unmodified alloys, respectively. The results of the stress-strain curves from uniaxial tensile loading as shown in Figure 4-20 indicate that the elongation is lower and YS is higher for the unmodified alloy than the Sr-modified counterpart, suggesting that the rate of damage represented by the damage parameter D should be higher for the unmodified alloy at any given strain value.

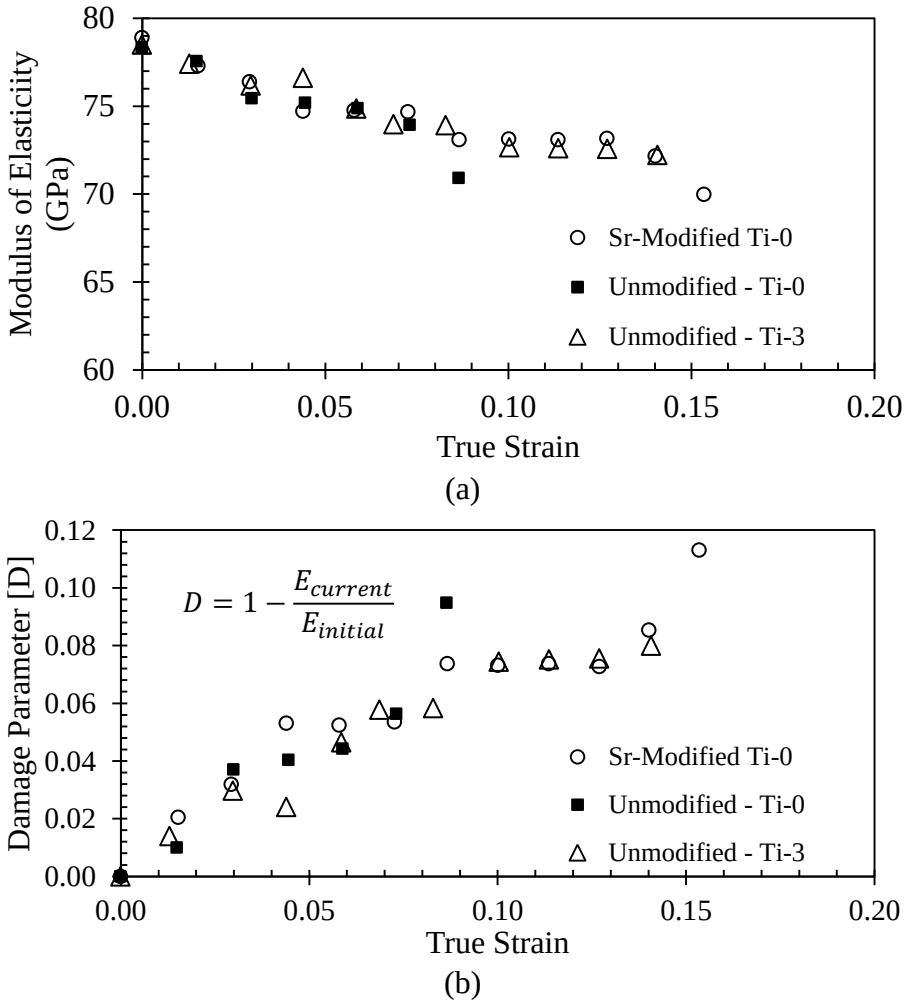


Figure 4-31. Damage characterization in A356 alloy under uniaxial tension, (a) modulus of elasticity versus true strain and (b) D values calculated from the values shown in (a).

Figure 4-32 shows the crack initiation site in the microstructure during uni-axial tensile loading of the Sr-modified Ti-0 condition sample. Figure 4-32 (a) shows a typical region in the microstructure prior to the tensile loading of the sample. The sample is a thin dog-bone tensile specimen and the test procedure was described earlier in section 3.3.1. Figure 4-32 (b) shows the microstructure at the same location as in Figure 4-32(a) at the onset of crack initiation in the Al-Si and Al-pore interfaces as can be observed in the magnified image in Figure 4-32 (c) obtained from the square box in Figure 4-32(b). The microstructures in Figure 4-32 show that during the plastic deformation stage of the

tensile curve shown in Figure 4-20 cracks begin to appear on the microstructure of the free surface of the sample under loading. These cracks were consistently observed on the surface microstructure alone and did not show up in the bulk microstructure of the sample. The shear bands initiate at the weakest regions of the microstructure, which are typically the interface between the Al matrix and Si, and Al matrix and pore.

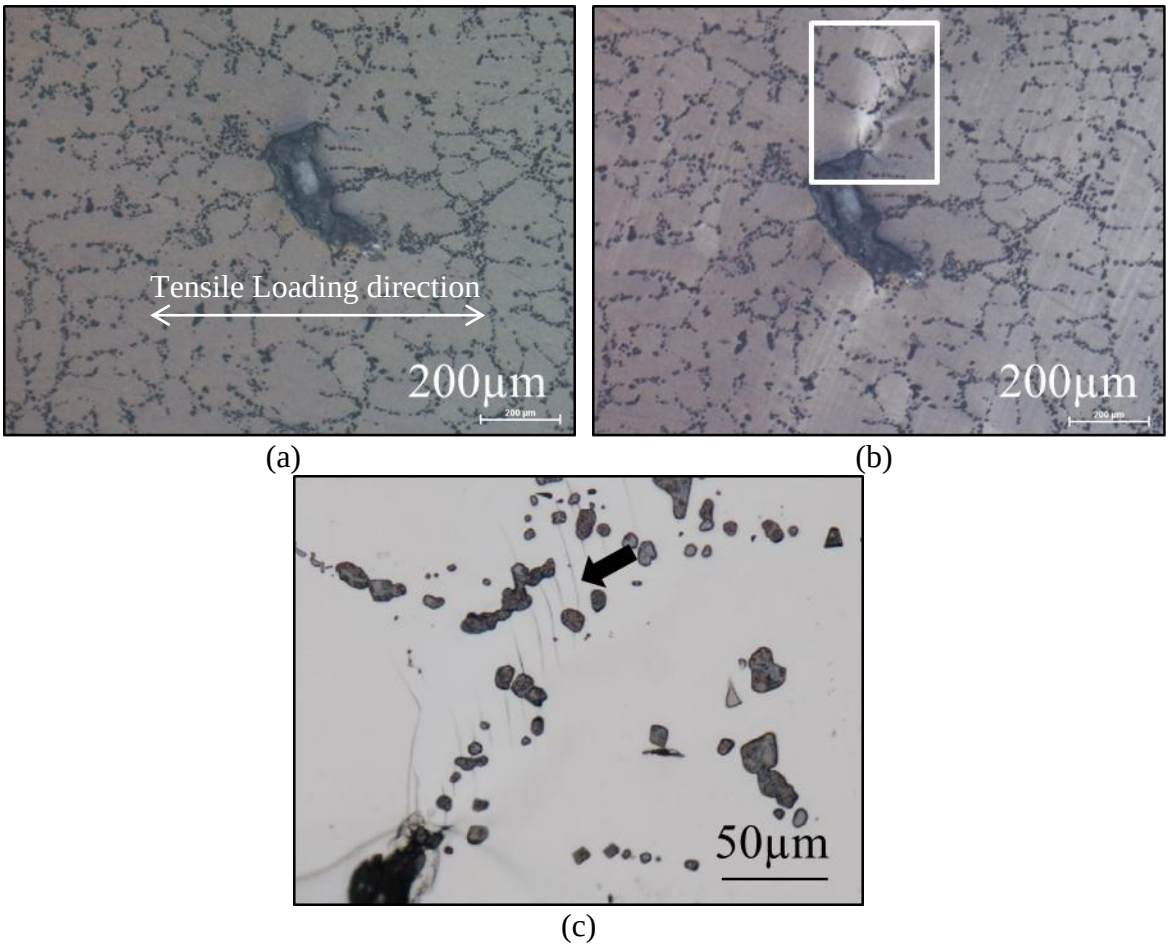


(a) (b)

(c)

Figure 4-32. Crack initiation at the Al-Si and Al-pore interfaces during uni-axial tensile loading of the Sr-modified Ti-0 alloy. (a) typical pore location in the microstructure taken prior to tensile loading, (b) microstructure from the same location as in (a) showing initiation of cracks at the Al-Si and Al-pore interfaces, (c) higher magnification of the square box in (b) showing the details of the initiated cracks.

Figure 4-33 (a-c) shows the typical SEM secondary image of surface cracks and shear bands that are present in the sample at fracture. Figure 4-33 (a) is for the Sr-modifed

alloy at Ti-0 condition showing the surface cracks oriented perpendicular to the loading direction and the shear bands oriented at a 45° angle to the tensile loading direction. Figure 4-33 (b) shows a magnified image of Figure 4-33(a) wherein the cracks and shear band can be observed to propagate through the interfaces of Al and Si phases. Figure 4-33 (c) and (d) are microstructures showing the surface cracks and intersecting shear bands in two different orientations for the unmodified Ti-0 alloy. Figure 4-33 shows that the surface cracks cause damage in the eutectic region at the Al-Si interfaces and extensive damage can be quite significant as can be seen in Figure 4-33 (d). These surface cracks could be initiation sites for bulk fracture in the sample during tensile loading.

The in-situ study of surface cracks developed during tensile loading has suggested that, in Sr-modified alloy where the Si phases are smaller with lower aspect ratio than those in the unmodified alloy, the formation of the surface cracks at the Al-Si phase interfaces would be triggered at a later stage during plastic deformation compared to the unmodified counterpart. This could result in higher elongation in the Sr-modified alloys as shown earlier Figure 4-20.

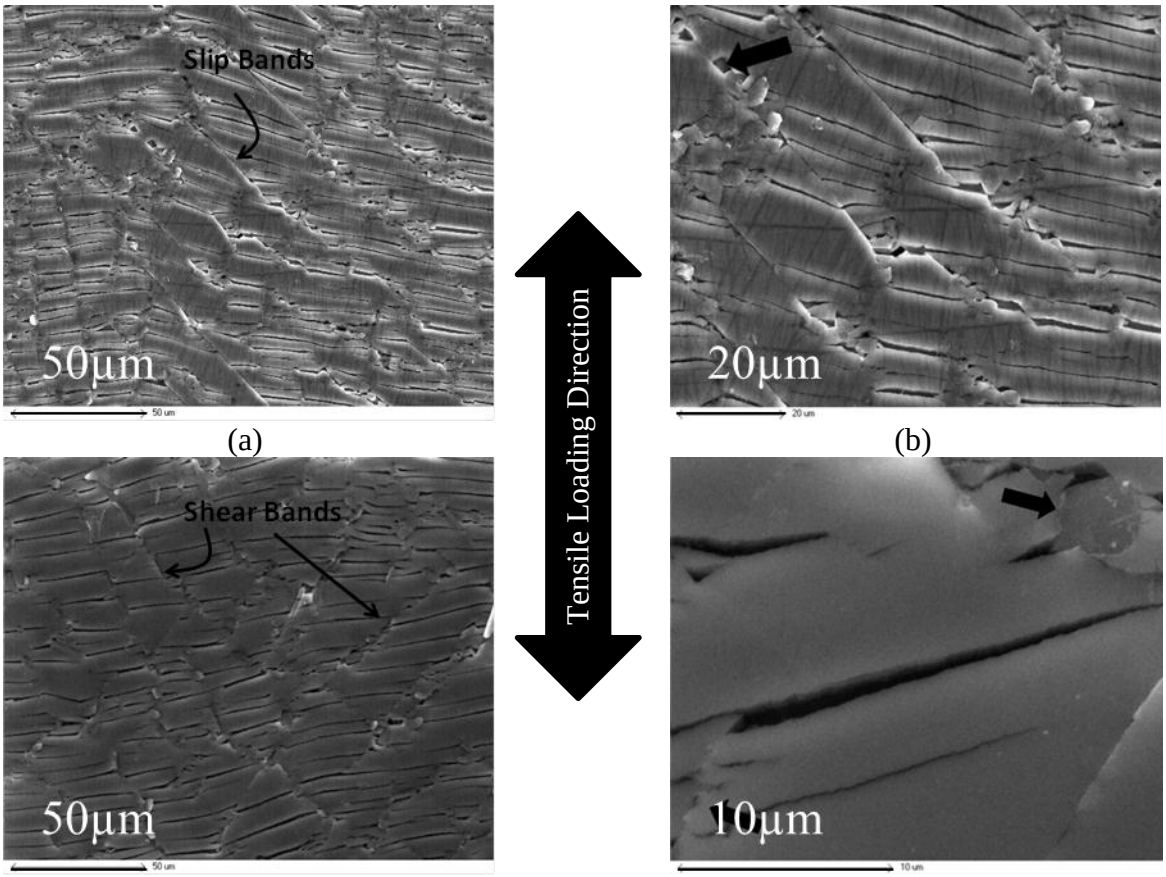


Figure 4-33. SEM secondary image showing surface cracks and slip bands developed, as indicated by arrows, during the plastic deformation stage of the tensile loading. (a) and (b) Sr-modified alloy at Ti-0 condition, and (c) and (d) unmodified alloy at Ti-0 condition.

Figure 4-34(a) and (b) show a Sr-modified tensile specimen that was polished with minimal force on the sample so that the only a few high peaks (light regions) of the surface undulations would be polished and the valleys (dark regions) would remain untouched. Figure 4-34 (b) shows surface cracking in the unpolished region and this is not observed in the polished region of the specimen. This indicates that these features (surface cracking) in occurring only on the surface and do not exist in the bulk. The origin of surface cracks perpendicular to the direction and their role in promoting damage localization via shear band formation needs to be further investigated.

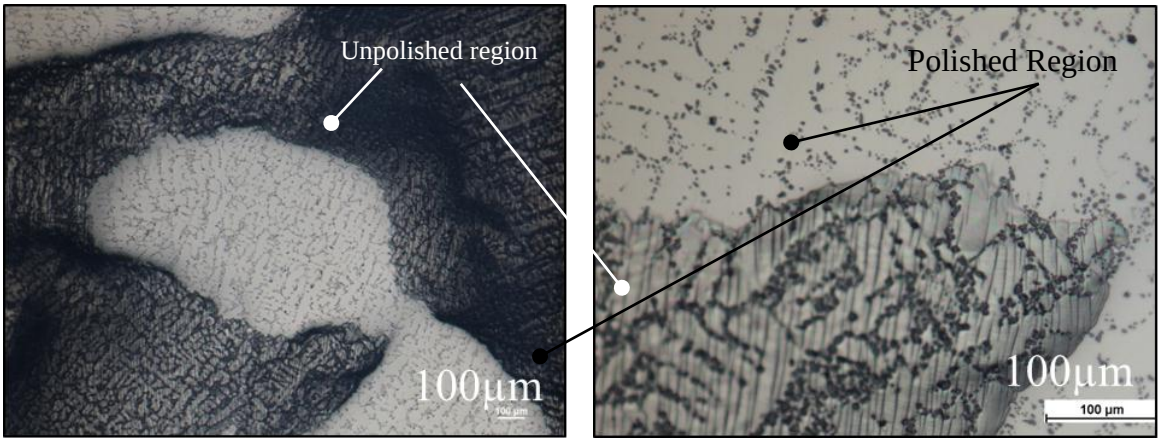


(a) (b)

Figure 4-34. Polished undulations on Sr-modified Ti-0 tensile specimen surface at different magnifications (a) 50X and (b) 200X.

### 4.2.4 Surface Topography

Under plastic deformation, the specimen experiences extensive surface deformation caused by the significantly large movements of grains in the microstructure (i.e., grain boundry sliding and rotation). The surface undulations were measured, as a function of axial strain, using Zygo profilometer resulting in surface topography maps, as shown in Figure 4-35. The maps shown were taken of specimen post-fracture at axial strains of 17.3% for Sr-modified Ti-0, 11.06% for unmodified Ti-0 and 15.43% for unmodified Ti-3 alloy. As reported earlier in section 4.1.3, the Sr-modified Ti-0 has the largest grain size, and the unmodified Ti-3 the smallest, out of the three alloys chosen for this study. The maps show that grains rotate out of plane as the specimen deforms and the extent of surface deformation is related to the initial grain size of the material. Surface topography data for each specimen at different axial strains was converted to the arithmetic average of the vertical deviations of the surface profile from the mean line (i.e., $R_a$ value). Figure 4-36 shows the results of the $R_a$ value versus axial strain. The plots show that the

Sr-modified Ti-0 exhibits the highest surface undulations, whereas the unmodified Ti-3 alloy exhibits the least surface undulations.

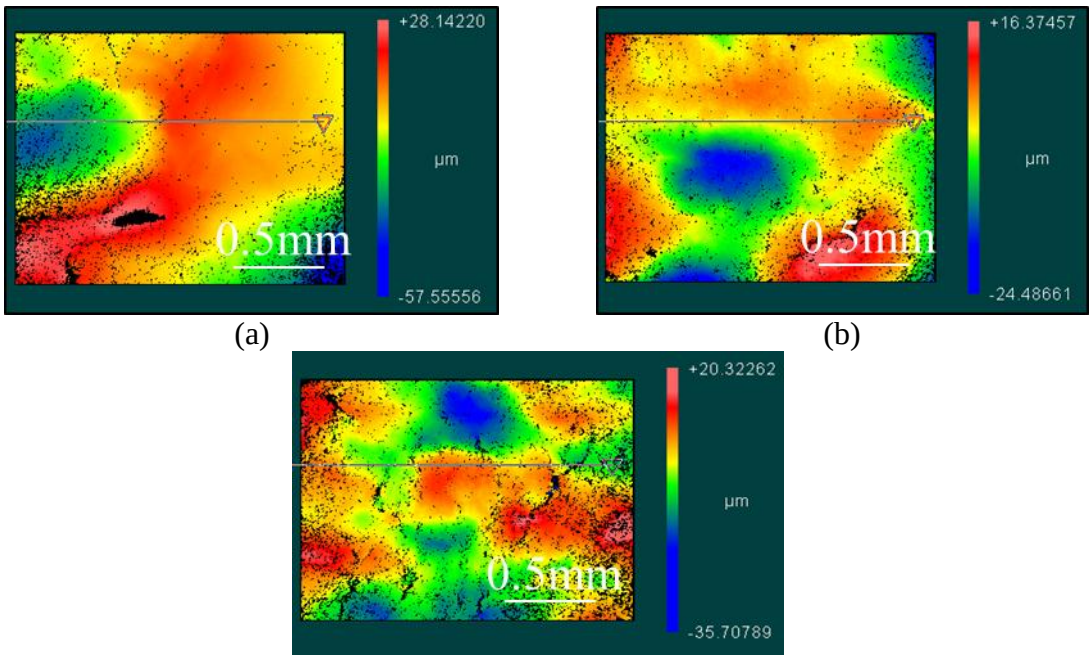


Figure 4-35. Post-fracture surface topography of tensile specimen post-fracture, (a) Sr-modified Ti-0, axial strain 17.3%, (b) unmodified Ti-0, axial strain 11.06%, and (c) unmodified Ti-3, axial strains 15.4%.

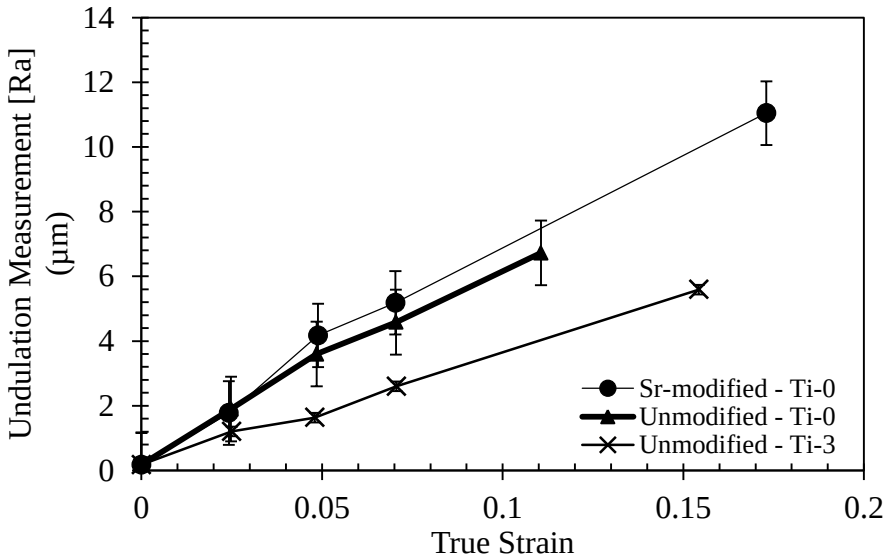


Figure 4-36. Surface undulation arithmetic mean [Ra] versus true strain for Sr-modified Ti-0, unmodified Ti-0 and unmodified Ti-3.

### 4.2.5 Observations from Fractured Tensile Specimens

Figure 4-37(a) and (b) shows micrographs revealing eutectic Si phase particle cracking in fractured tensile specimen from unmodified Ti-0 and Sr-modified Ti-0 alloys respectively. The cracks in the Si phase are predominantly orthogonal to the tensile loading direction for both alloys. The orientation of the fracture within the eutectic Si phase particles is quantified in Figure 4-38(a) which represents in the form of a histogram the observations in Figure 4-37. The results show strong agreement with the literature as seen in Figure 4-38(b). Figure 4-39(a) and (b), and Figure 4-40(a) and (b) show histograms characterizing the cracked eutectic Si phase particle in the unmodified and Sr-modified alloy, respectively, in terms of equivalent particle size and particle aspect ratio. The bulk and cracked particle data in there figures as shown as dashed and continuous lines respectively. The larger elongated particles are more susceptible to fracture as opposed to smaller equiaxed particles.

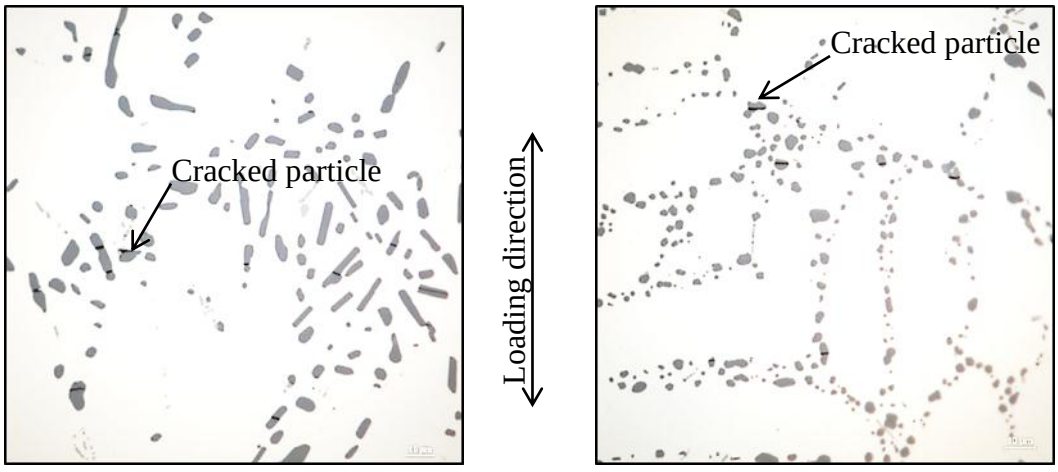


Figure 4-37. Post-fracture micrographs (1000X) post-fracture of tensile specimen showing eutectic Si phase particle cracking, (a) unmodified, and (b) Sr-modified alloys at 10.25% and 15.8% global strain respectively.

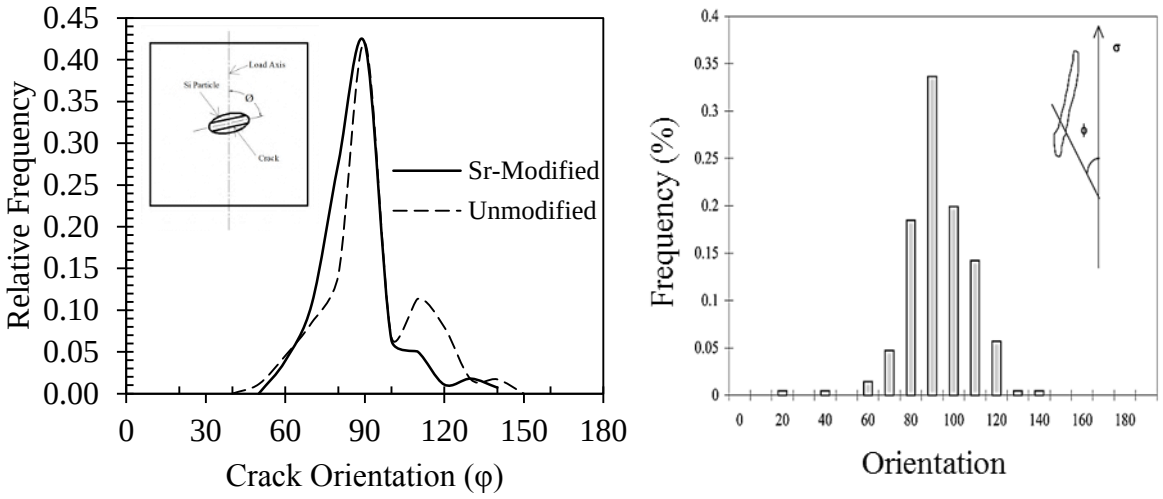


(a) (b)

Figure 4-38. Histogram showing the crack orientation (φ) with respect to the tensile load axis, (a) unmodified and Sr-modified at 10.25% and 15.8% global strain, respectively and (b) results from the literature for Sr-modified A356 [4].

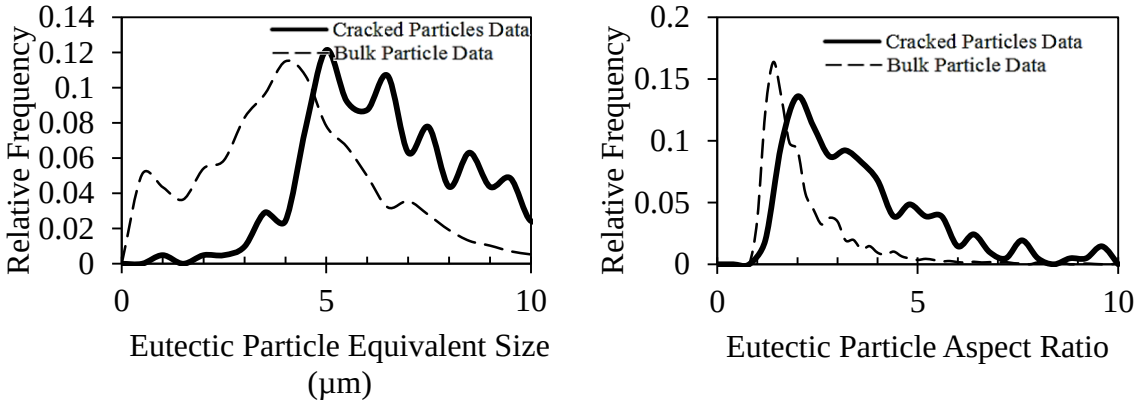


(a) (b)

Figure 4-39. Histogram showing (a) particle size distribution, and (b) aspect ratio of the cracked Si particles versus bulk Si particles in the unmodified Ti-0 alloy at 10.25% global strain.

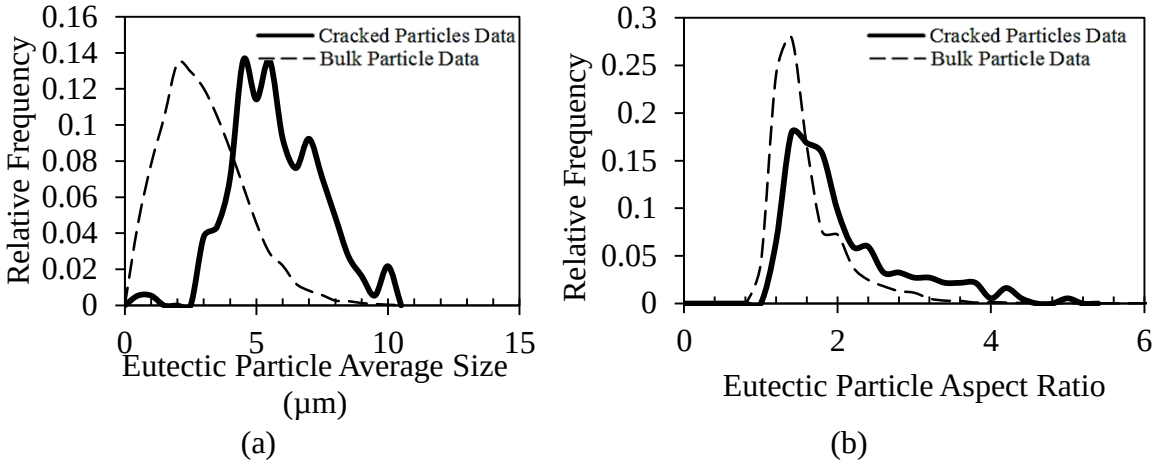


Figure 4-40. Histogram showing (a) particle size distribution, and (b) aspect ratio of the cracked Si particles versus bulk Si particles in the Sr-modified Ti-0 alloy at 15.8% global strain.

Figure 4-41 shows that fraction of particles damaged at fracture for the unmodified and Sr-modified alloys. The data shows that the unmodified alloy has a much higher fraction of damaged particles (0.12) at a much lower strain value (10.25%) compared to the Sr-modified alloy. This is due to the fact that larger-elongated particles have a much lower critical stress value as indicated by the model formulated by Gurland et al. [59]. Figure 4-42(a) shows the probability of the particle damage ($P=N_{Damage}/N_{Bulk}$) versus the size of the particle for the failed tensile specimen from the unmodified and Sr-modified alloys. The results indicate that probability increases in a non-linear fashion with the increase in particle size. The results show a similar trend to existing data within the literature for tensile testing carried out on a Sr-modified A356-T6 (Figure 4-42 (b)). These results agree with the model developed by Gurland et al. [59] where larger particles have a higher tendency to fracture.

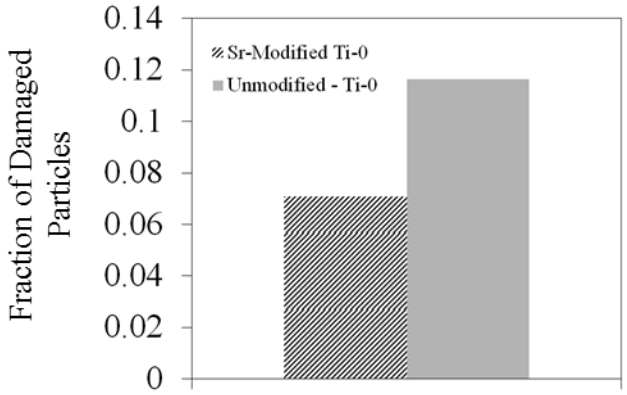


Figure 4-41. Fraction of damaged particles due to tensile loading for unmodified and Sr-modified A356 alloy at fracture strains of 10.25 and 15.8%, respectively.

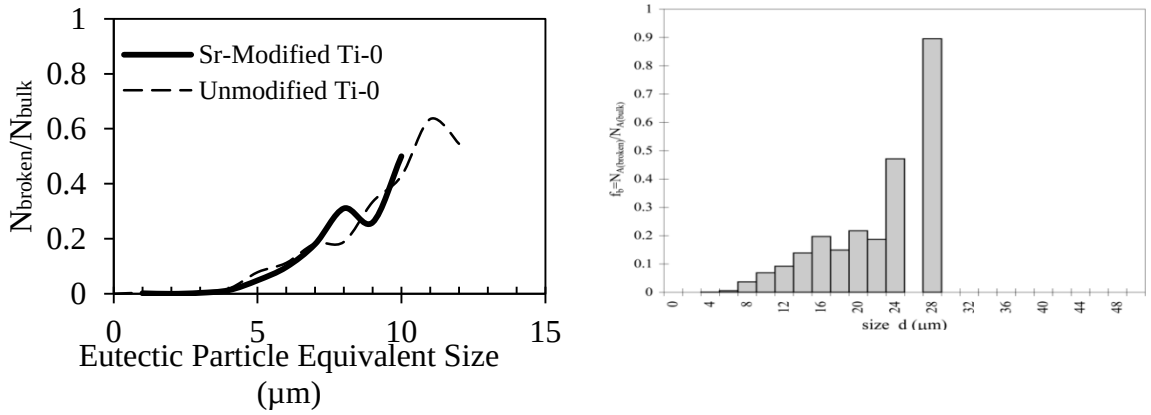


(a) (b)

Figure 4-42. Probability histogram of particle damage due to tensile loading versus eutectic Si phase particle size, (a) experimental data for unmodified and Sr-modified A356 alloy at 10.25% and 15.8% axial strain, respectively (at fracture) and (b) experimental data from the literature for Sr-modified A356 at 7.5% axial strain (at fracture) [4].

Figure 4-43, 4-44 and 4-45 show micrographs of the fracture surfaces of Sr-modified Ti-0, unmodified Ti-0 and unmodified Ti-3 tensile specimens at three different magnifications. The fracture surfaces show that the specimen exhibited dimpled rupture where the dimples are formed at the cracked eutectic Si phase particles by plastic deformation of the matrix. The elongated nature of the dimples result from elongated Si particles in the unmodified alloy in contrast to the equiaxed dimples from round eutectic silicon phase particles in the Sr-modified alloy.

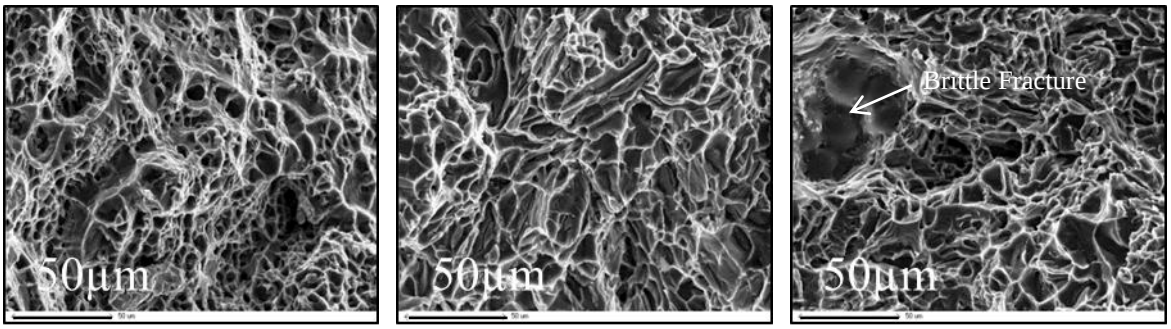


(a) (b) (c)

Figure 4-43. SEM micrographs of the fracture surface at 625X, (a) Sr-modified Ti-0, (b) unmodified Ti-0, and (c) unmodified Ti-3 alloys.

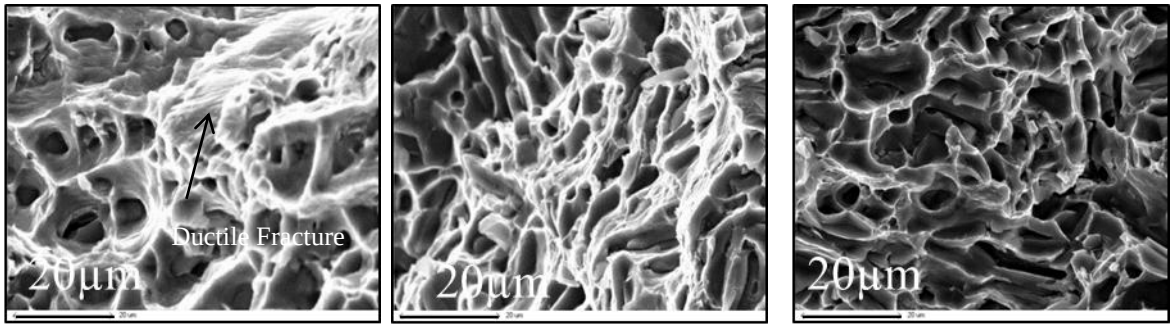


(a) (b) (c)

Figure 4-44. SEM micrographs of the fracture surface at 1550X, (a) Sr-modified Ti-0, (b) unmodified Ti-0, and (c) unmodified Ti-3 alloys.

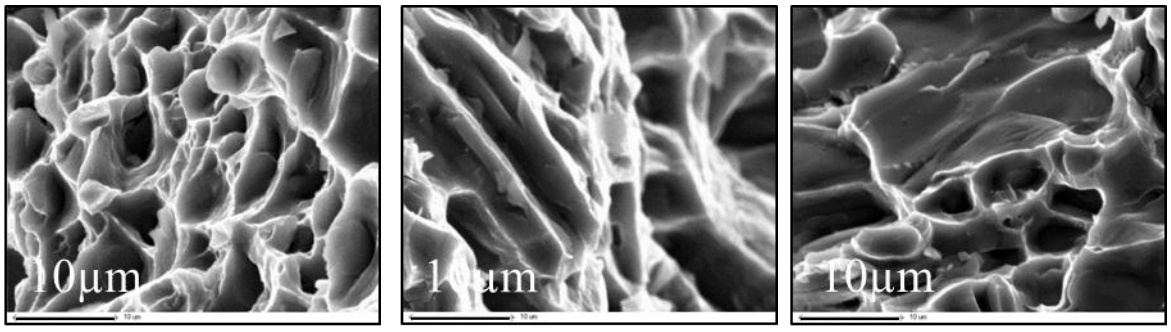


(a) (b) (c)

Figure 4-45. SEM micrographs of the fracture surface at 3240X, (a) Sr-modified Ti-0, (b) unmodified Ti-0, and (c) unmodified Ti-3 alloys.

## 4.3 Deformation Characteristics in Compression Loading

This section presents the results of compression testing and microstructural analysis of fractured specimens from the unmodified and Sr-modified alloys. The analysis of fractured eutectic Si phase particles is presented to compare the effect of shape and size of the particles on deformation behavior in uniaxial compression.

### 4.3.1 Overview

Limited uniaxial compression testing was carried out to determine if the damage processes in various compositions of A356 alloy were different from that in uniaxial tension in the unmodified and Sr-modified alloys, both in the Ti-0 condition. The results in the form of stress-strain curves are shown in Figure 4-46 where the two materials exhibit rather similar response with only minor differences in YS. The specimens were deformed to a global strain of about 25% with no visible fracture. The plot only shows strain up to 7% as the specimen surface was intensely deformed affecting the ARAMIS global strain measurement data unreliable.

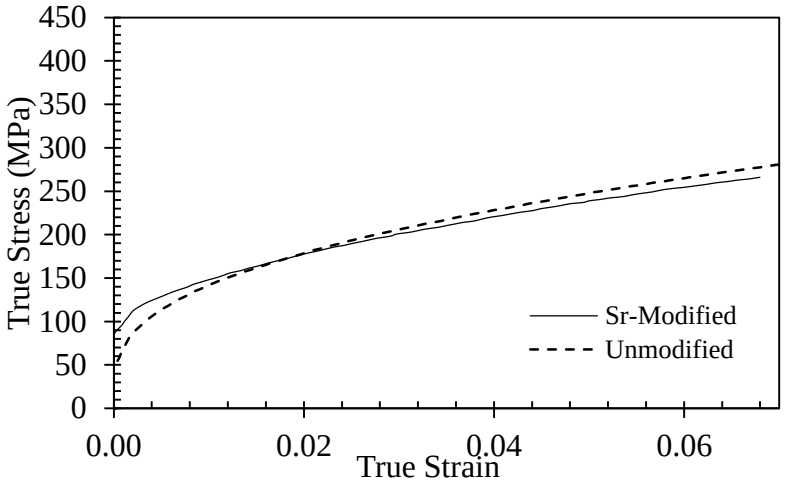


Figure 4-46. Uniaxial compression stress-strain curves for unmodified and Sr-modified alloys.

### 4.3.2 Microstructural Observations from Deformed Compression Specimen

Figure 4-47 shows the damage mechanism that occured on the specimen free surfaces, where Si phase particle decohesion was widely observed throughout out the specimen surface. Most Si phase particle are seen to be unaffected by deformation and cracking of the phase particles was rare. In comparison, the bulk microstructure revealed extensive particle cracking and particle decohesion similar to the case of uniaxial tension, see Figure 4-48. In the case of the unmodified alloy, the particle cracking occurs at a direction that is orthogonal to the major dimension of the particle and independent of the particle orientation. Also, the elongated particles are mainly subjected to cracking and not the round ones. As for the Sr-modified alloy, particle cracking seems to be in the direction of the applied load. Figure 4-49(a) shows a histogram of particle crack orientation for unmodified and Sr-modified alloys, wherein the crack direction parallel to the compressive loading direction is observed in the Sr-modified alloys. However, no such preferred orientation of the crack was observed in the unmodified alloys.

Figure 4-49(b) shows a histogram of particle crack orientation for Sr-modified A356 from the literature where the results show that particles favored crack orientation is along the loading direction which is with agreement with the results shown Figure 4-49(a). Figure 4-50 and Figure 4-51 show the particle size and aspect ratio distribution for unmodified and Sr-modified alloys subjected to a global uniaxial compressive strain of 11.5 and 12.07%, respectively; wherein, the cracked Si phase particles are compared to those in the bulk. Both figures show that larger and non-equiaxed particles are more susceptible to cracking, specifically, the unmodified alloy has an average cracked particle size of 6.6µm and aspect ratio of 3.4 as opposed to the Sr-modified in which the average cracked particle size is 5.2µm and aspect ratio is 1.96. Typically, Figure 4-50 and Figure 4-51 show that the size of the cracked particles are typically greater than about 5 µm; in the unmodified alloy, the number of particles in this preferred size range is significantly greater than that in the Sr-modified alloy.

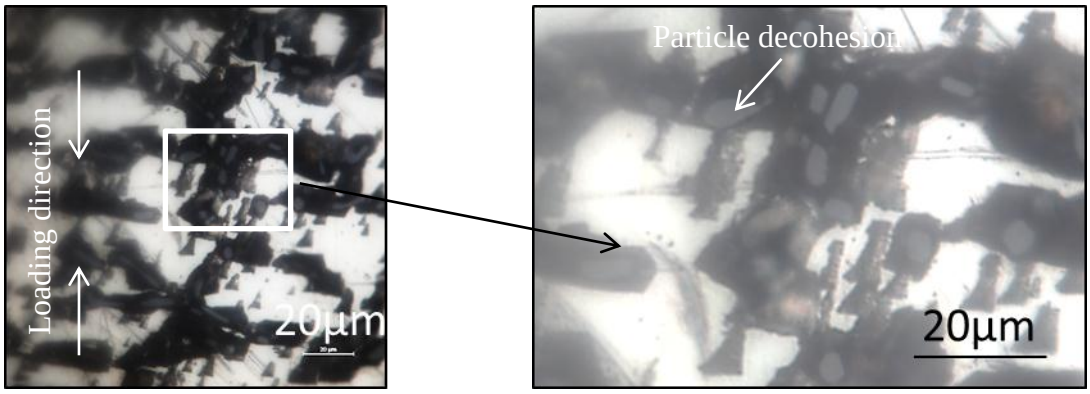


Figure 4-47. Surface damage characteristics in an unmodified A356 compression specimen surface.

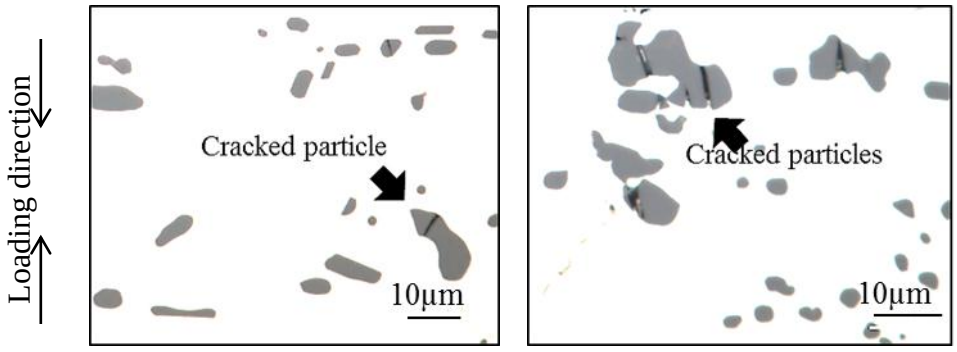


Figure 4-48. Bulk damage characteristics under compression, (a) unmodified, and (b) Sr-modified alloys at 11% and 12.25% axial strain, respectively.

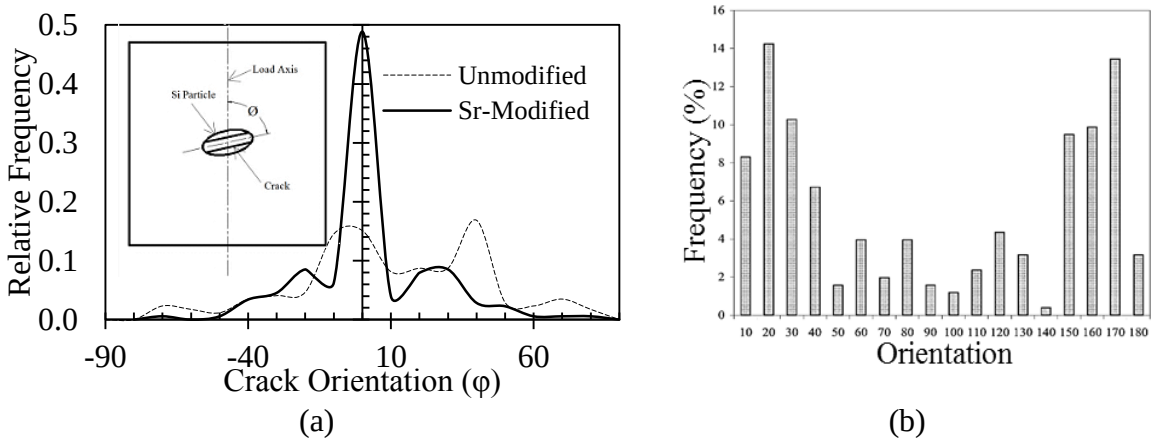


Figure 4-49. Histogram showing the crack orientation (φ) with respect to the compressive load axis for (a) unmodified and Sr-modified alloys (b) results from the literature for Sr-modified A356 [4].

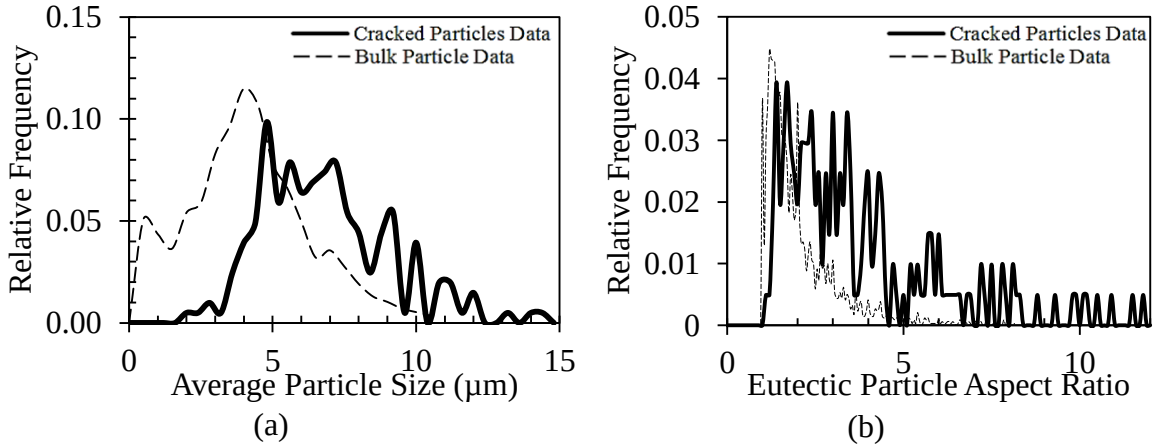


Figure 4-50. Histogram showing, (a) particle size distribution, and (b) aspect ratio of the cracked Si particles versus bulk Si particles in the unmodified Ti-0 alloy after compression loading (at 12.07% global strain).

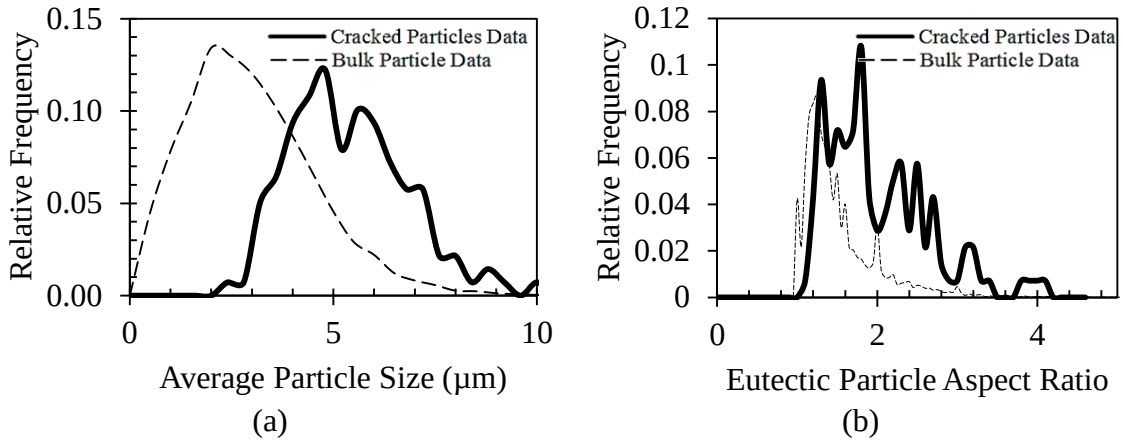


Figure 4-51. Histogram showing, (a) particle size distribution, and (b) aspect ratio of the cracked Si particles versus bulk Si particles in the Sr-modified Ti-0 alloy after compression loading (at 11.5% global strain).

Dighe et al [4] suggested that in A356 alloy, typically, for tensile loading, the cracks in the eutectic Si phase particles are usually orthogonal to the loading direction and for compressive loading, the cracks are usually parallel to the loading direction. According to the results shown in Figure 4-38, the orientation of the cracks in eutectic Si phase particles deformed under tensile loading are indeed orthogonal to the loading direction and agrees with the results presented by Dighe et al [4]. But in the case of compressive loading of the Sr-modified alloy (see Figure 4-49), the results do agree with the statement that the cracks are parallel to the loading direction by Dighe et al [4]. Also, in the case of unmodified alloy (with elongated Si particles), the results in Figure 4-49 show that there is no preferred directionality to fracture for the particles in compressive loading. Further, the micrographs of cracked particles in Figure 4-37 show that extremely elongated particles prefer to crack orthogonal to the major axis of the particle even when they are randomly oriented with respect to the loading direction. In the unmodified alloy, the aspect ratio coupled with the larger size of the eutectic Si phase particles play a dominant

role in effecting a random orientation of the cracks in the particles, rather than the direction of the compressive loading.

Figure 4-52 shows the fraction of particles damaged at fracture for the unmodified and Sr-modified alloys. The unmodified alloy has a much higher fraction of damaged particles at a much lower strain value. For the same reason as given for uniaxial tensile results, larger-elongated particles have a much lower critical stress value as indicated by the model formulated by Gurland et al. [59]. When compared with the tensile results (see Figure 4-41), compression exhibits a lower fraction of damaged particles. This is consistent with the results in the literature [4]. Figure 4-53 (a) shows the probability of the particle damage ($P=N_{Damage}/N_{Bulk}$) versus the size of the particle for deformed compression specimen from the unmodified and Sr-modified alloys. The results indicate that probability increases in a non-linear fashion with the increase in particle size. The results again show a similar trend to existing data within shown in Figure 4-53 (b) and once again agree with the model developed by Gurland et al. where larger particles have a higher tendency to fracture. It is to be noted that the differences in the probability of fractured eutectic Si phase particles in the Sr-modified alloy and the results of Dighe et al. is due to the fact that the results displayed by the author were from specimens that have experienced 22.5% (see Figure 4-53 (b)) opposed to the results shown in Figure 4-53 (a) which were from specimens that experienced 12% of strain.

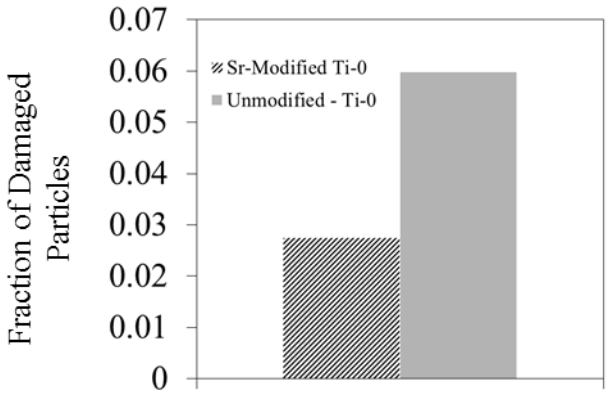


Figure 4-52. Fraction of damaged particles due to compressive loading for unmodified and Sr-modified A356 alloy.

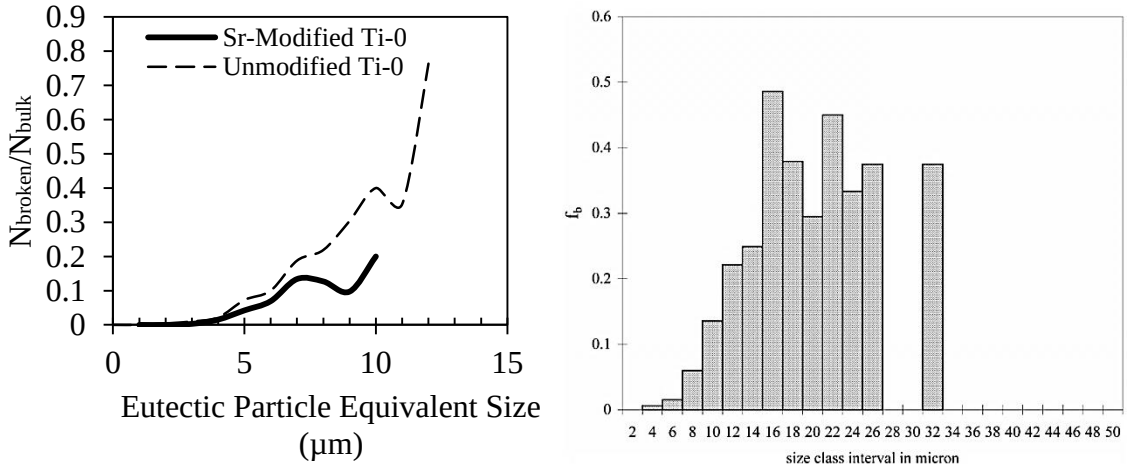


(a) (b)

Figure 4-53. Probability histogram of particle damage due to compressive loading versus eutectic Si phase particle size, (a) experimental data for unmodified and Sr-modified A356 alloy at 10.5% and 12% axial strain, respectively and (b) experimental data from the literature for Sr-modified A356 at 22.5% axial strain [4].

## 4.4 Deformation Characteristics in V-Bending

In this section, the unmodified and Sr-modified alloys are subjected to V-bending to assess their bendability properties and correlate them to microstructural features in order to understand the effect of eutectic Si phase particles shape and size on the bendability of the material.

### 4.4.1 Overview

Figure 4-54(a) and (b) shows the load per unit cross-section area versus the bend angle and the bending moment versus the bend angle respectively for the unmodified and Sr modified Ti-0 alloys. The plot shows that Sr-modified alloy exhibits a higher load and bend moment capacity compared to the unmodified alloy. For the unmodified alloy, the load starts to drop at a bend angle of $20.65^0$ as cracks starts to initiate from the tensile surface. Sr-modified alloy on the other hand could be bent to a $40^0$ angle without any fracture. Similar results were observed when plotting bending mandrel displacement versus bend angle as shown in Figure 4-55. Figure 4-56 shows the specimen in the punch-die configuration at the end of the test. The figure shows that Sr-modified has an enhanced bendability as compared to the unmodified alloy. The results are generally consistent with previously presented tensile and compressive test results (compare Figure 4-20 and Figure 4-55).

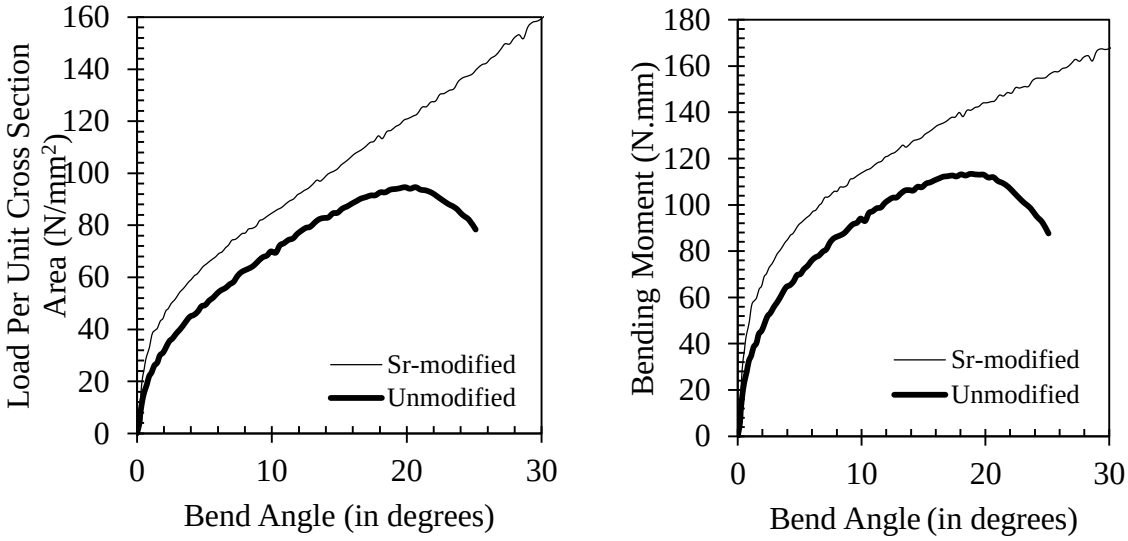

Figure 4-54. Load characteristics in the V-bending tests, (a) load per unit cross-section versus bend angle, and (b) bending moment versus bend angle for a V-bend test for unmodified and Sr-modified Ti-0 alloy.

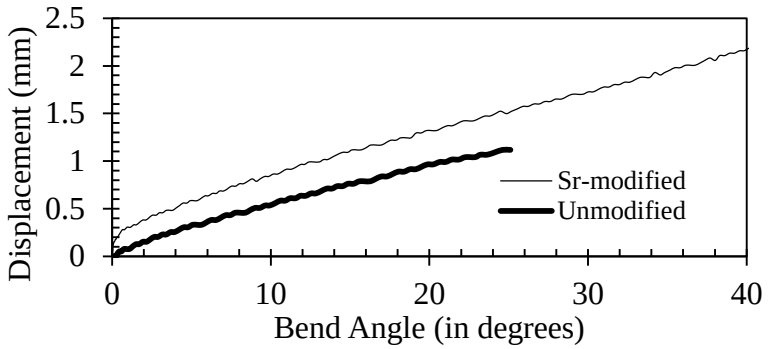


Figure 4-55. Punch displacement versus bend angle for a V-bend test for unmodified and Sr-modified, both in Ti-0 condition.

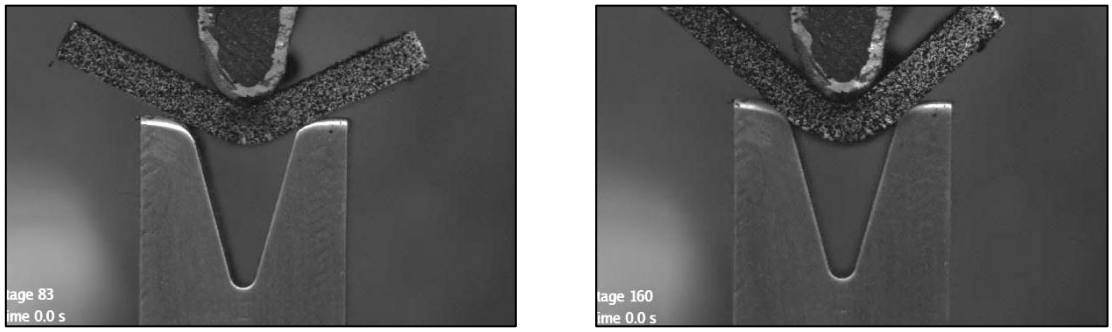


(a) (b)

Figure 4-56. Bend specimen in punch-die configuration at the maximum bend angle for each alloy, (a) unmodified, and (b) Sr-modified alloys.

### 4.4.2 Strain Mapping

Figure 4-57 shows the tangential strain map of the surface of a bend specimen at bend angle of $22.5^0$ for both the unmodified and Sr-modified alloys. The strain maps show the typical features of a bend specimen; the outer fiber is subjected to tension, inner fiber is compressed and a zero strain region exists near the mid-section of the specimen (neutral axis). However, these visual examinations do not reveal much differences between the two alloys.

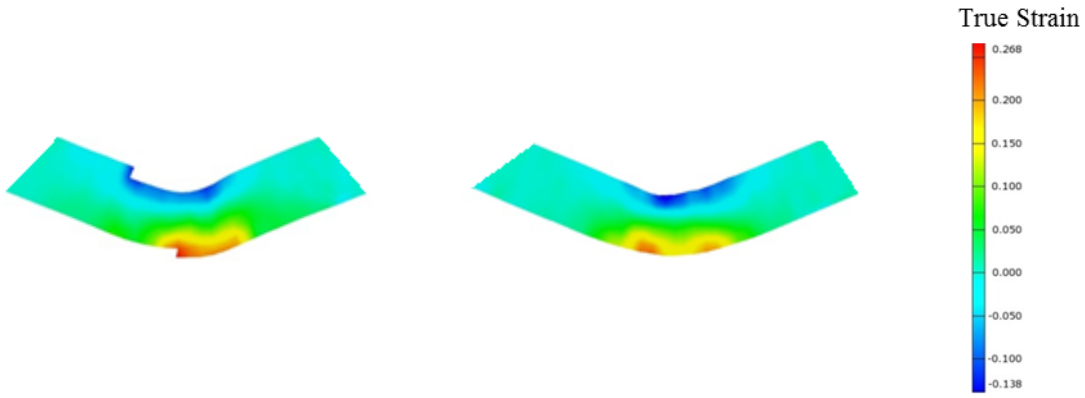


Figure 4-57. Surface tangential strain map of bend specimen at $22.5^0$ bend angle, (a) unmodified alloy and (b) Sr-modified alloy.

A vertical section through the sample thickness at the line of symmetry of the bend was used to plot the tangential and radial strain profiles versus the thickness of the specimen for various bend angles as shown in Figure 4-58 and Figure 4-59, respectively, for the unmodified and Sr-modified alloys. In Figure 4-58 and Figure 4-59, the thickness on the x-axis is measured from the top surface (compressive side) of the specimen in Figure 4-56.

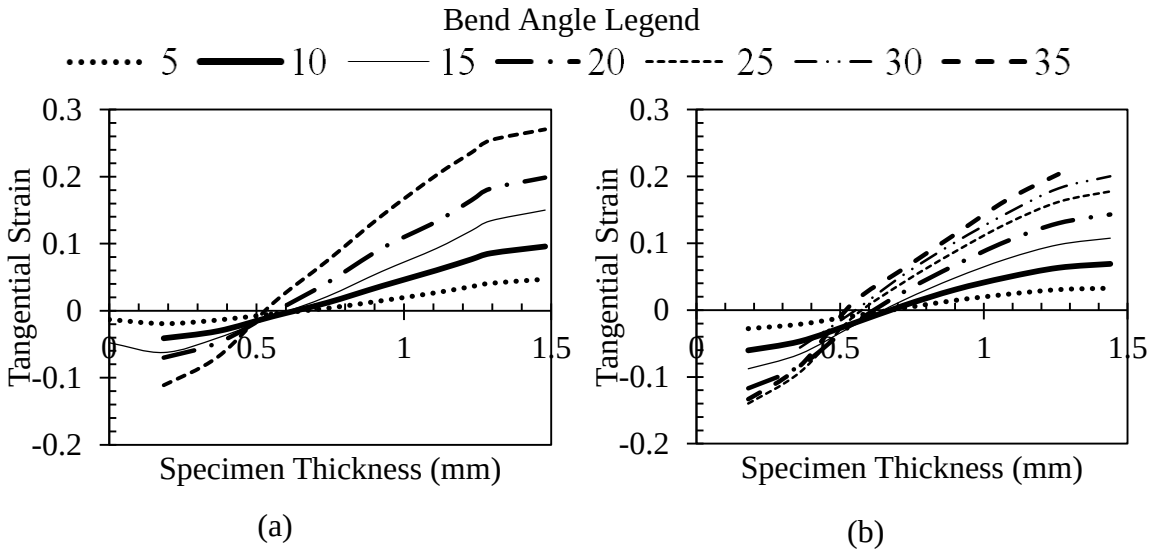


Figure 4-58. Tangential strain profiles across specimen thickness at different bend angles from V-bending tests for (a) unmodified alloy and (b) Sr-modified alloy.

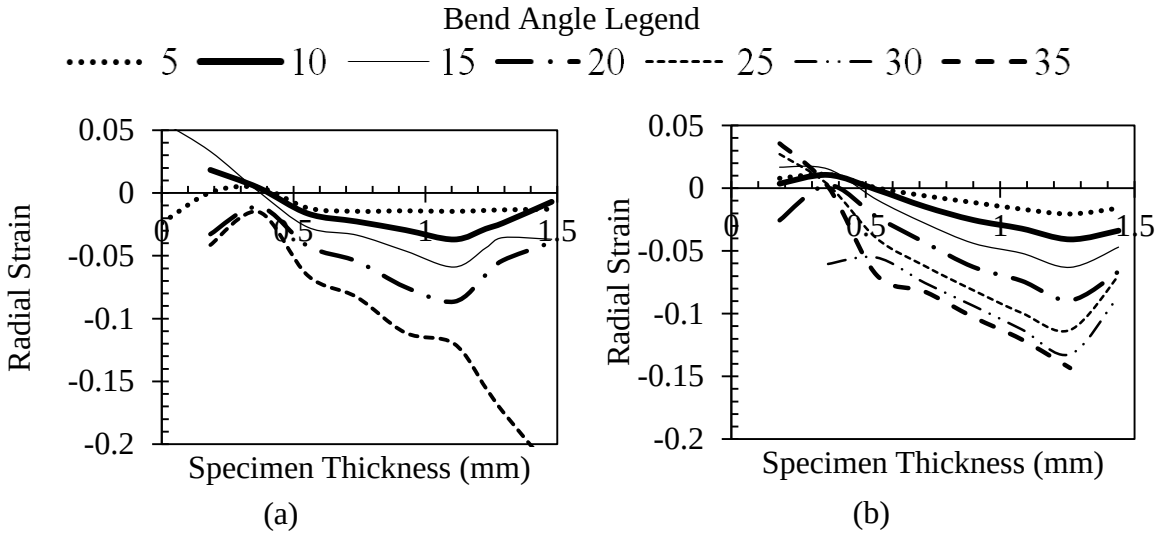


Figure 4-59. Radial strain profiles across specimen thickness at different bend angles from V-bending tests for (a) unmodified alloy and (b) Sr-modified alloy.

In Figure 4-58 (b), the Sr-modified alloy experiences a significantly larger bend angle than that for the unmodified alloy in Figure 4-58(a). Further, in Figure 4-58 (b), the tangential strain at any given bend angle is significantly lower for the Sr-modified alloy than that for the unmodified counterpart in Figure 4-58(a). Figure 4-59(a) and (b) show that there is no significant difference in the distribution of the radial strain between the unmodified and Sr-modified alloys, respectively.

Figure 4-58(a) and (b) show there is a shift in the neutral axis of the sample towards the compression region of the sample as the bend angle increases during the test. This can be observed by the shift in the intersection point between each tangential strain profile at specific bend angles with the horizontal line at zero tangential strain value. This intersection point shifts to negative strain values (compression regime) for both the unmodified and Sr-modified alloy alike.

It is to be noted from earlier Figure 3-8 (c) that the sample did not have large width to thickness ratio for plane strain bending mode (typically a ratio of 8 is recommended for plane strain whereas the samples used had a ratio of 3.3). This was due to two main experimental limitations. First, the flat bend sample had to be prepared from a 12mm dia. round bars limiting the width of the sample and a certain minimum thickness was needed for through-thickness measurement using the Aramis system. Second, the available V-bending test jig design had a width limitation of about 6 mm. The implication of not achieving plane strain state is that the magnitudes of tangential and radial components of strain at the bend line, as measured by Aramis from the edge of the V-bend specimen, are not equal as evident in Figure 4-58 and Figure 4-59. In fact, the magnitudes of radial strain are significantly lower than those of the tangential strain at extreme fiber locations. There is also measurement errors due to the possibility of some edge effect (i.e., at top and bottom surfaces) from the Aramis system.

However, Figure 4-60 shows that for a specific bend angle, the shift in the neutral axis is more for the unmodified alloy than the Sr-modified counterpart. Figure 4-20 shows that the fracture strength and elongation is higher for the Sr-modified alloy than the unmodified alloy and hence, the neutral axis shift is greater to the compression regime in the unmodified alloy for the V-bend test than that for the Sr-modified alloy in order to allow more material in the tensile regime and compensate for the lower tensile strength in the sample.

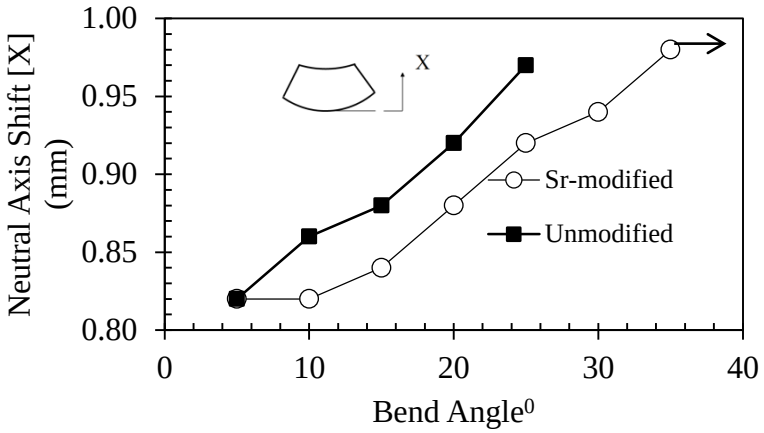


Figure 4-60. Neutral axis shift versus bend angle for unmodified and Sr-modified Ti-0 alloys.

Figure 4-61 is a plot of the thickness reduction and the rate of change of the thickness reduction versus the bend angle, and plot of the derivative showing the rate of thickness reduction as a function of bend angle for both the unmodified and Sr-modified alloys. The unmodified alloy fractures at a 10% thickness reduction whereas the Sr-modified alloy reaches the same thickness reduction at a higher bend angle with no sign of fracture. Further, Figure 4-61(a) shows that the rate of thickness reduction is greater for the unmodified alloy which suggests that the rate of flow of material is grater for this alloy compared to the Sr-modified alloy. Figure 4-61 (b) shows that rate of change in the specimen thickness for the unmodified alloy is much greater that the Sr-modified alloy.

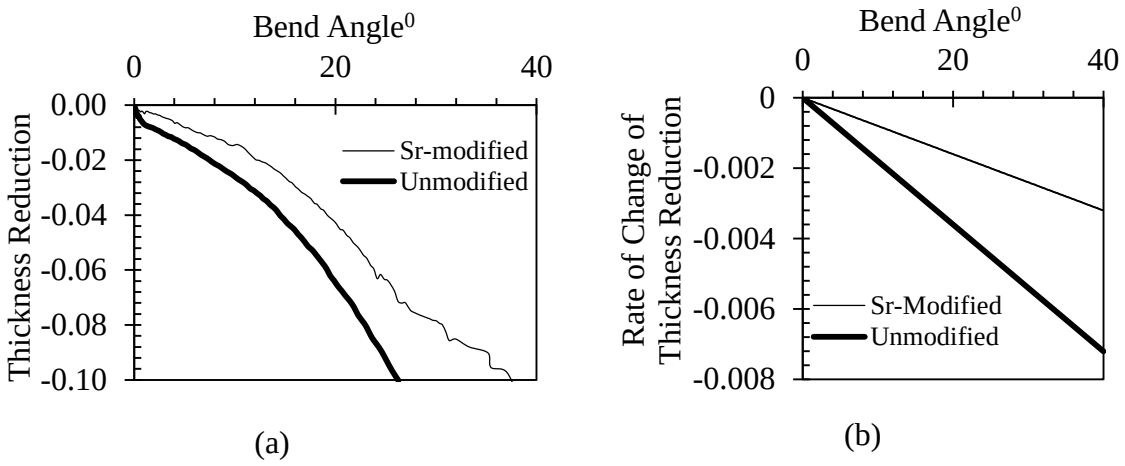


Figure 4-61. Effect of the bend angle on, (a) thickness reduction, and (b) thickness rate of change of thickness reduction for unmodified and Sr-modified Ti-0 alloys.

### 4.4.3 Damage Quantification

Figure 4-62 (a-f) shows several through-thickness micrographs from an unmodified Ti-0 bend specimen at a bend angle of $13.25^0$. Figure 4-62 (b) and (c) shows two regions on the tensile side of specimen were strain is localized and a crack has initiated. Also, shear bands are observed in Figure 4-62 (d). It is clear that the shear bands are intensified around the eutectic Si phase particles. Figure 4-62 (e) located in the mid-section of the specimen shows that in this region of low strains, the effect of strain localization and the development of shear bands are at its minimum. Figure 4-62 (f) located in the compressive side of the specimen also shows extensive strain localization and the development of intersecting shear bands.

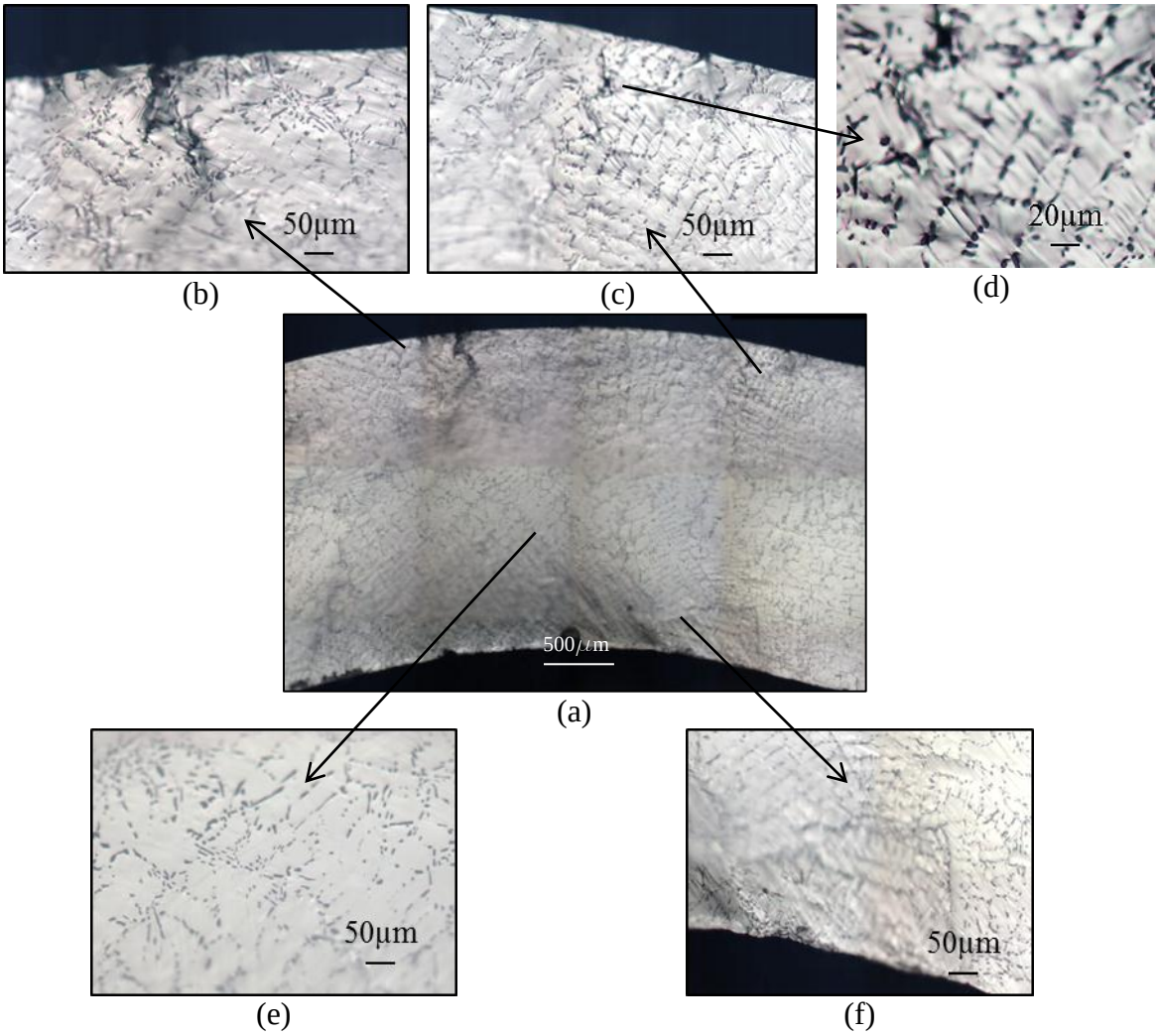


Figure 4-62. Optical micrographs from interrupted V-bend tests for an unmodified Ti-0 alloy specimen, test interrupted $13.25^0$ bend angle, (a) low magnification image, (b) and (c) high magnification images of two locations at the zero thickness (surface) of the sample where two cracks have independently initiated, (d) high magnification microstructure of the region pointed in (c) showing the existence of shear bands in the specimen, (e) high magnification microstructure at an area around the unaffected neutral axis of the specimen and (f) high magnification microstructure from the bottom of the specimen which is under compression.

Figure 4-63 (a-f) shows the through-thickness optical micrographs of the unmodified (a-c) and Sr-modified (d-f) Ti-0 alloys. Figure 4-63 (a) shows the a fractured unmodified alloy bend specimen thickness under the punch at lower magnification at a bend angle of $16^0$ whereas Figure 4-63 (b,c) are higher magnification micrographs of the tensile and compressive regions of the specimen, respectively. The particle cracking mainly occurs at

the elongated particles and the crack orientation is orthogonal to the loading direction. Figure 4-63 (b) reveals that the tensile region of the specimen has experienced extensive particle cracking that induced void growth and coalescence well ahead of the crack front. Even the compressive region of the specimen (Figure 4-63 (c)) has experienced particle cracking whereas hardly any particle cracking or failure was observed for the Sr-modified specimen at a bend angle of $40.75^0$ Figure 4-63 (d-f). The specimen exhibited no major cracking and only localized or isolated eutectic Si phase particle cracking. Figure 4-64 (a) and (b) shows magnified micrographs shown in Figure 4-63 (b) and (e), respectively revealing extensively cracked eutectic Si phase particles in the bent unmodified alloy and largely uncracked Sr-modified bend specimen.

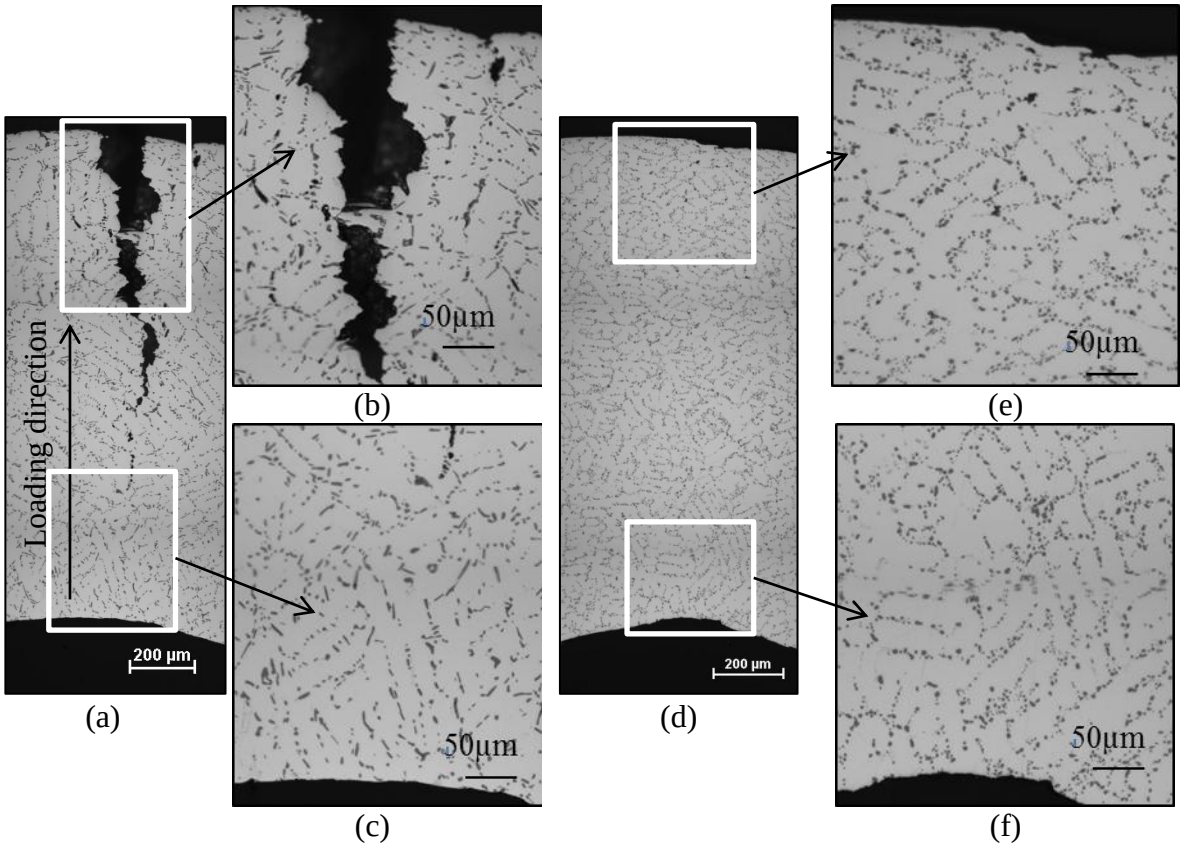


Figure 4-63. Through-thickness microstructure of deformed bend specimen. (a-c) Unmodified bend specimen at a $16^0$ bend angle (fractured) and (d-f) Sr-modified bend specimen at a $40.75^0$ bend angle (unfractured).

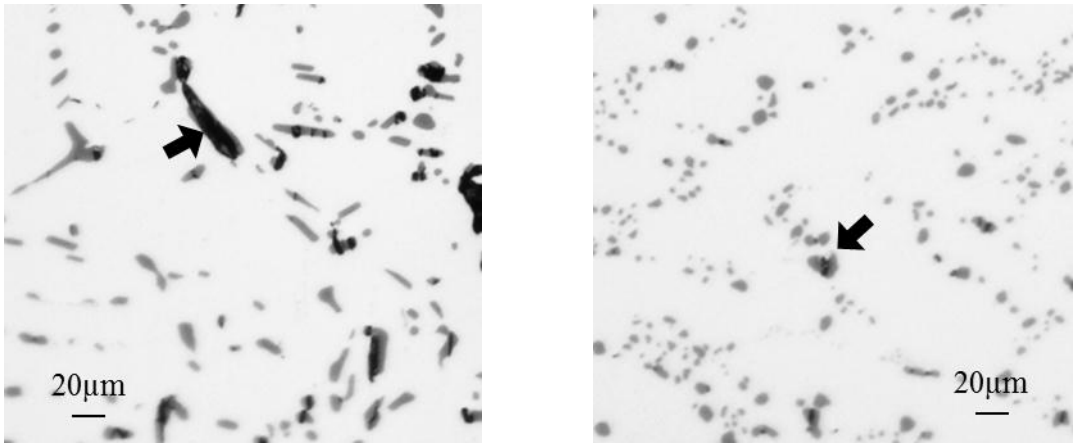


Figure 4-64. Particle cracking in bending, (a) unmodified and (b) Sr-modified alloys.

From the micrographs shown in Figure 4-63, the number of cracked particles was analyzed and the result shown in Table 4-3. Sr-modified alloy, at a larger bend angle,

exhibits a smaller number of cracked particles and lower number of cracked particles to total number of particles ratio compared to the unmodified alloy. Figure 4-65 and Figure 4-66 show the cracked and bulk particle size and aspect ratio of the unmodified and Sr-modified alloys, respectively. It is to be noted that the larger elongated particles are more susceptible to fracture as seen in tensile and compressive deformation modes.

Table 4-3. A comparison of number of cracked particles between unmodified and Sr-modified alloys.

| Alloy | Unmodified Ti-0 | Sr-modified Ti-0 |
|---|---|---|
| Bend Angle | 16 | 40.75 |
| Number of Particles within Field of View (under mandrel) | 3225 | 8144 |
| Number of Cracked Particles | 372 | 393 |
| No. of Cracked Particles/No. of Particles | 12.19% | 4.57% |
| Specimen | Fractured | Did not fracture |

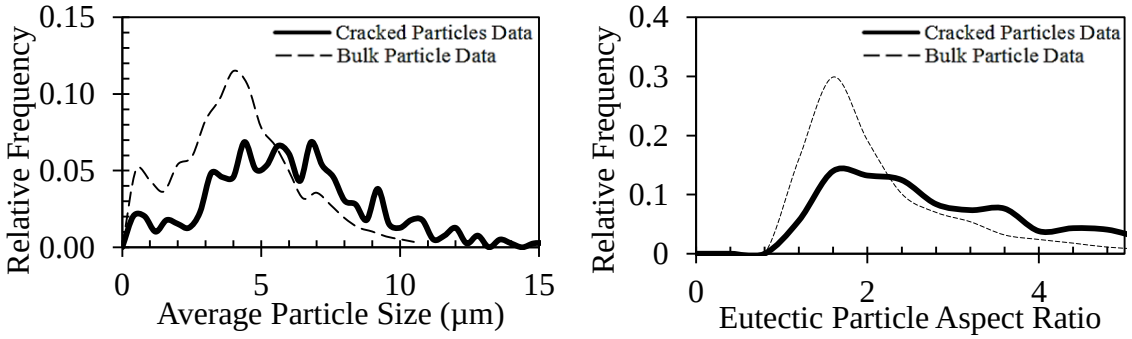


Figure 4-65. Histogram showing, (a) particle size distribution, and (b) aspect ratio of the cracked Si particles versus bulk Si particles in the unmodified Ti-0 alloy after bend loading at a bend angle of $16^0$.

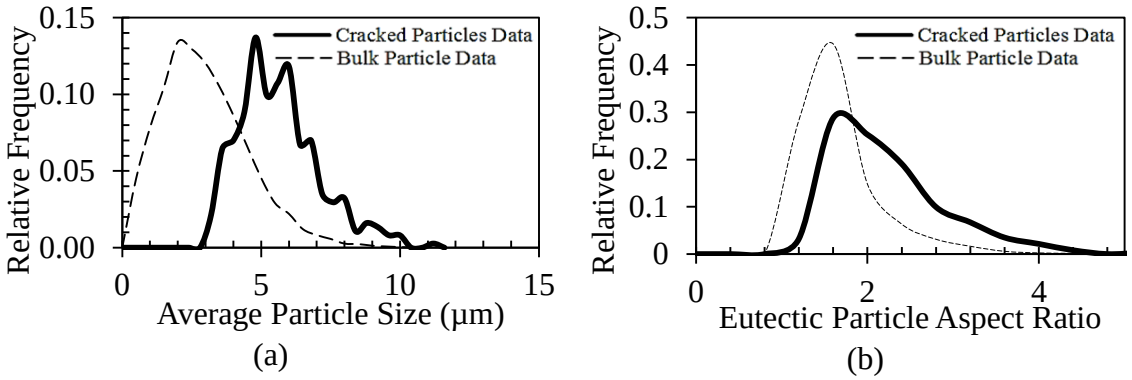


Figure 4-66. Histogram showing, (a) particle size distribution, and (b) aspect ratio of the cracked Si particles versus bulk Si particles in the Sr-modified Ti-0 alloy after bend loading at a bend angle of $40.75^0$.

### 4.4.4 Bendability

Figure 4-67 shows a plot of the inner radius to thickness ($R_I/t_0$) ratio versus the bend angle. The results show that the decrease in the ($R_I/t$) value for the Sr-modified alloy is more rapid compared to the unmodified alloy indicating that the bendability of the Sr-modified alloy is better. Figure 4-68 shows the results for the bendability ($R_{I,min}/t_0$) of the unmodified alloy and Sr-modified Ti-0 alloys. The overall results shows that by modifying the alloy using Sr, the bendability ($r_{i,min}/t_0$) is decreased by about 33% indicating the enhancement in bendability and that the allowable bend angle prior to macro-fracture is increased by about 200%. The enhanced bendability is due to the fact of that Sr-modified alloy exhibits a much lower fraction of damaged particles than the unmodified alloy (see earlier Table 4-3) particle cracking as discussed earlier, is attributed to larger-elongated particles that induce stress concentration and fracture more easily.

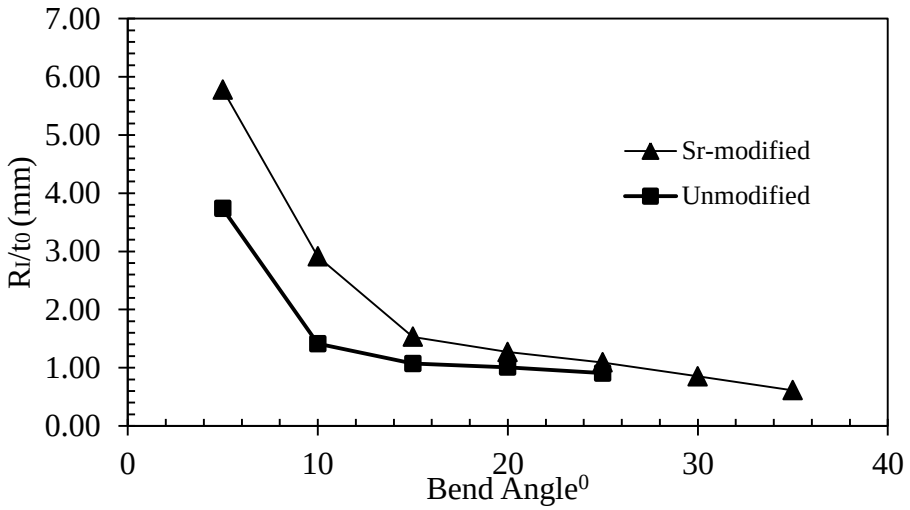


Figure 4-67. Comparison of bendability of unmodified and Sr-modified alloys in terms of ($R_I/t$) value versus bend angle, where $R_I$ is the inner radius of the bend specimen and t is the specimen thickness.

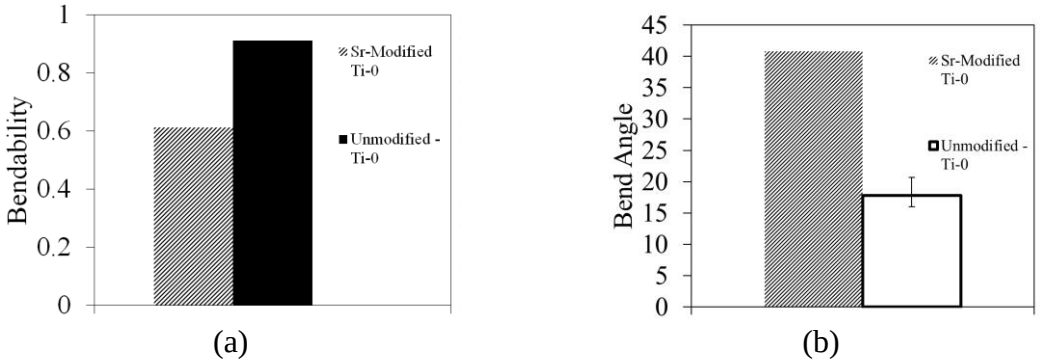


(a) (b)

Figure 4-68. Comparison of unmodified and Sr-modified alloys, (a) bendability and (b) bend angle at prior to crack initiation.

## 4.5 Summary

### 4.5.1 Alloys Behavior under Tensile, Compressive and Bend Loading

From results shown in previous sub-sections, it is evident that Sr-modified alloys exhibits enhanced mechanical properties when compared to the unmodified alloy. When tested under tensile and bend loading, the Sr-modified alloy shows more ductility and more bendability compared to the unmodified alloy. But when compressed, the alloys show

negligible differences. Figure 4-69 shows a comparison between tensile and compression stress-strain curves for unmodified and Sr-modified alloys.

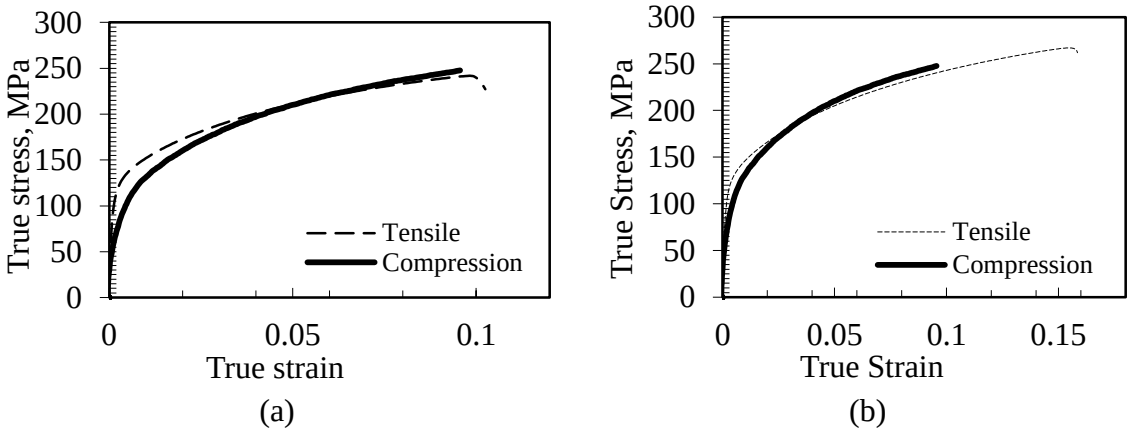


Figure 4-69. A comparison of stress-strain curves under tensile and compressive loading, (a) unmodified and (b) Sr-modified alloy.

### 4.5.2 Cracked Particle Comparison under Different Types of Loading

Figure 4-70 and Figure 4-71 show a comparison of the cracked particle, size and aspect ratio, for specimen subjected to different types of loading and the particles prior to deformation. The results show that for both unmodified and Sr-modified alloys that the average size and aspect ratio of the cracked particles are relatively equivalent for the different types of loads. The larger and elongated particles are more susceptible to fracture.

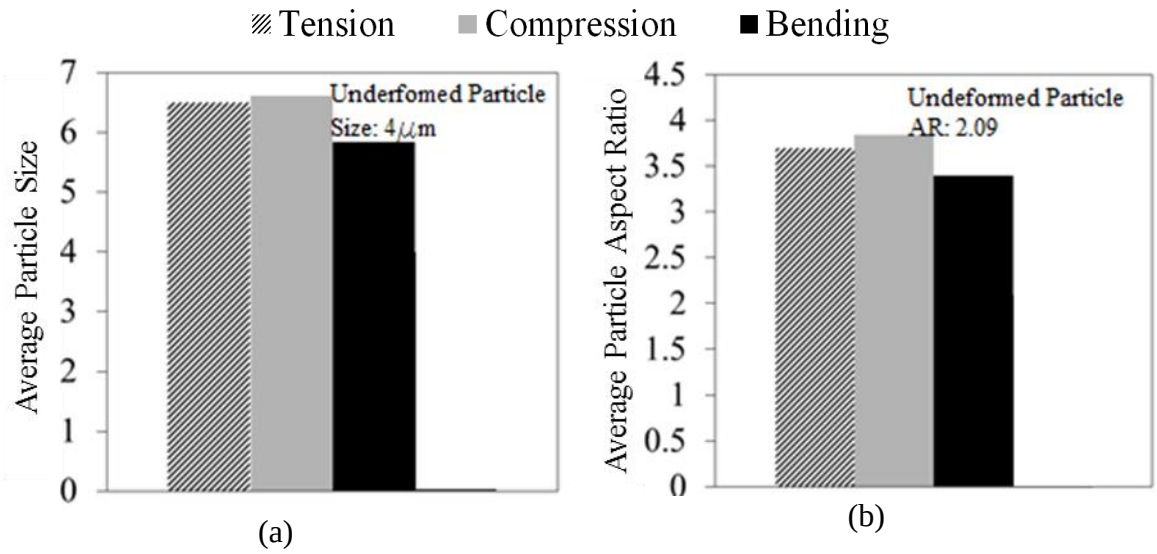


Figure 4-70. A comparison of particle characteristics under uniaxial tension, uniaxial compression and V-bending. The data is obtained from deformed specimens of the unmodified alloy as well as for undeformed alloy, (a) average particle size and (b) average aspect ratio.

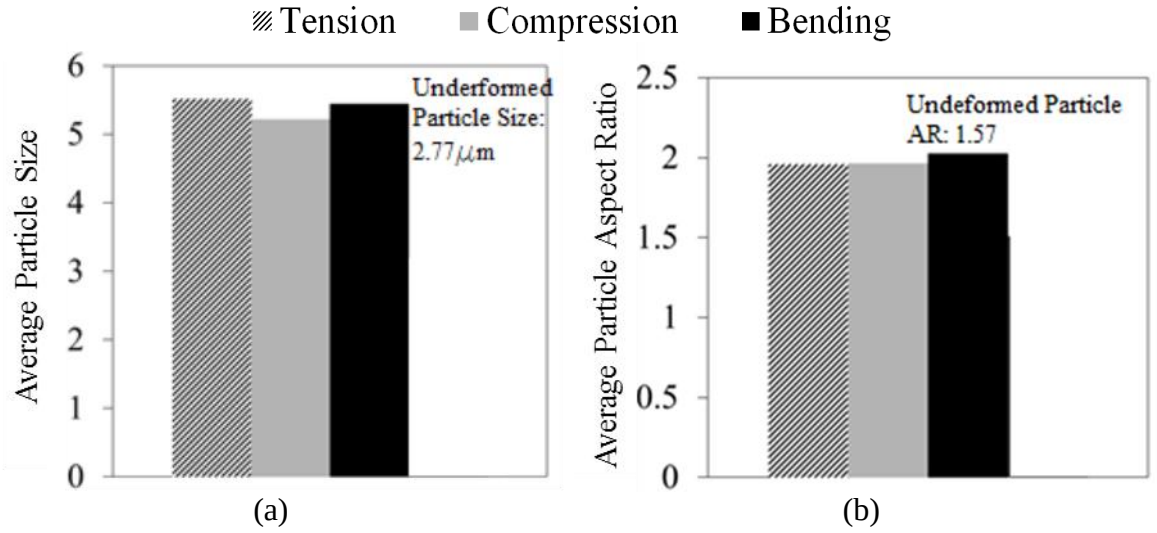


Figure 4-71. A comparison of particle characteristics under uniaxial tension, uniaxial compression and V-bending. The data is obtained from deformed specimens of the Sr-modified alloy as well as for undeformed alloy, (a) average particle size and (b) average aspect ratio.

Figure 4-72 shows the fraction of damaged eutectic Si phase particles for tensile, compressive and bend loadings for the unmodified and Sr-modified alloys. The results show that the unmodified alloy exhibits a higher fraction of damaged particles for all loading

conditions. It is also observed that compression has the least fraction of damaged particles for both alloys. Comparing the tensile results for the Sr-modified alloy with results found by Dighe et al. [4], it is to be noted that the fraction of the damaged particles is comparable in value. Dighe et al. [4] carried out his experiments of a Sr-modified A356 subjected to a T6 heat treatment. The authors reported fraction of damaged particles as 0.065 at 7.5% strain, whereas the results shown in Figure 4-72 (b) give a value of 0.07 at a 15.8% for tensile loading. This indicates that the for tensile loading, the vicinity of 0.07 fraction of damaged particles is the criterion for specimen fracture and the difference in stress and strain levels between the T4 and T6 specimen is accommodated by the Al matrix phase.

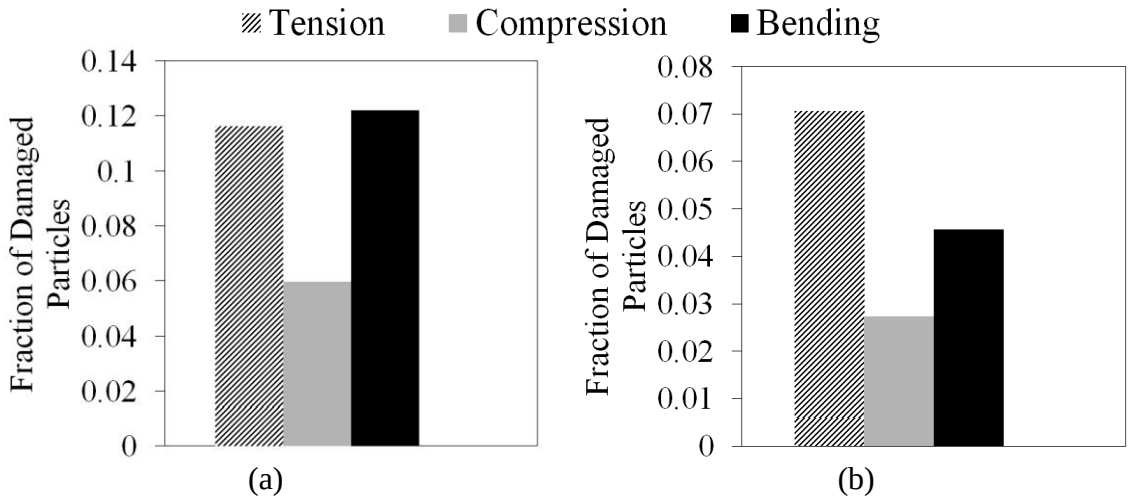


Figure 4-72. Fraction of damaged particles for tensile, compressive and bend loading from fractured specimens, (a) unmodified, and (b) Sr-modified alloys.

Figure 4-73 shows a comparison of the micro-hardness (Vickers Hardness) of the Al-matrix for the unmodified and Sr-modified alloy. The results show that the differences between the micro-hardness numbers of the two alloys are negligible. This observation suggests that any differences in mechanical properties or damage evolution are strongly related to the effect of eutectic Si phase particles.

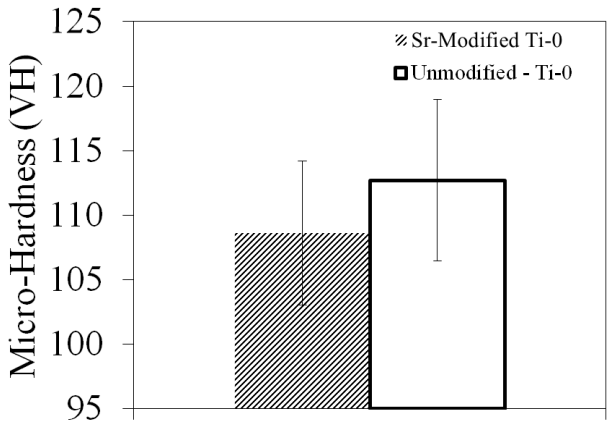


Figure 4-73. Micro-hardness measurements in the unmodified and Sr-modified Ti-0 alloys after 7.5% pre-strain.

# Chapter 5 Conclusions

The following conclusions are the attributed to the experimental results presented and discussed in the previous chapter.

- Titanium addition has no effect on the morphology of the second phase particles but has an adverse effect on the specimen porosity. Addition of Ti in alloy is seen in the refinement of the average grain size.
- Strontium refines both size and shape (morphology) of the eutectic Si phase particles, where the particles of the Sr-modified alloy are seen to have a finer average equivalent particle size, more uniform distribution and more round shaped particles, as opposed to the elongated larger particles seen in the unmodified alloy.
- Strontium addition has no effect on properties of the Al-phase, as observed by Vicker's hardness measurements.
- Titanium and strontium are found to have an adverse effect on the porosity content of the alloy where the addition of 0.02 wt% Sr to the Ti-free alloy increased the average size of the pores by 116% and the pore fraction area by 500%. And by adding 0.14 wt% Ti to the Sr-free alloy had no effect on the average pore size but increased the pore fraction area by 700%.
- The specimens with larger grains (unmodified and Sr-modified Ti-0) are found to experience severe strain localization and out-of-plane deformation when compared to the grain-refined alloy (unmodified Ti-3) in tensile mode of deformation.

- Sr modification enhances the elongation of the A356 alloy by 52% with a negligible compromise to the yield strength.
- Eutectic Si phase particles and grain structure are primary determinants of deformation behavior of A356 alloy and not the porosity.
- Adding Sr to the A356 alloy does not change the material response to uniaxial compression loading. The only difference in the unmodified and Sr-modified alloys during compression was the orientation of the cracks of the eutectic Si phase particles. The particles in the unmodified alloy favored to crack along the major axis of the particle, whereas the modified version of the alloy cracked along the axis of loading.
- Sr-modification resulted in a significant decrease in the bendability value ($r_{i,min}/t_0$) of the cast A356 alloy by about 33% and increasing the allowable bend angle by 128%. Indicating that Sr-modification enhances the bending behavior of the A356 alloy.
- Comparing the average sizes and aspect ratios of cracked particles, uniaxial tension, compression and V-bending behavior were consistent for each alloy where a certain particle size and particle aspect ratio was favored to crack.
- The main conclusion is that the shape and size of second phase particles plays a major role in the deformation behavior of cast A356 alloy. The refinement of these particles in the A356 alloy or possible in other cast Al alloys with second phase particles is crucial to the improvement of the mechanical properties.

# Chapter 6 Future Work and Recommendations

The following are future work and recommendations suggested in order to achieve a better understanding of the role of grains and eutectic Si phase particles in the strain localization and damage process in the A356 alloy.

- The effect of Ti and Sr on the porosity content of the alloy should be further investigated to verify that these constituents adversely affect the porosity content within the alloy. It is recommended to use a wide spectrum of Ti additions to the unmodified and Sr-modified A356 alloy and perform quantitative porosity analysis. As well as using different levels of Sr in the Sr-modified alloy. A plot of the pore average size and pore fraction area versus the Ti and Sr content would give an understanding of their effect on porosity development during the solidification process.
- The material used for the study presented in this thesis would be great candidate to validate polycrystalline models to study the interaction between deformation and grains. To perform this task, Electron Back Scattered Diffraction (ESBD) analysis should be carried out on the specimen the ESBD data provides (such as grain orientations) and is used as an input for the polycrystalline models. The results from the model could be compared to experimental strain mapping results that utilize the DIC method.
- Using a CCD camera with a higher resolution in the Aramis system would be beneficial in spotting out strain inhomogeneity in the small grained specimens and

would enhance the quality of the strain maps developed for the larger grained specimens.

- It is highly recommended that with this kind of material, testing in-situ microscope not to be done under a regular optical microscope or stereoscope as the material experiences large out of plane deformation. It is recommended to utilize the SEM with a large depth of focus which would help solve the problem faced while testing under a regular optical microscope or stereoscope. With a proper surface etching technique, micrographs from the SEM could be uploaded to Aramis system supplying a full field strain maps at a sub-grain level. These strain maps when correlated with the micrographs should help build a better understanding of the strain localization process leading to specimen rupture.
- The use of smaller tensile specimens for the unmodified and Sr-modified alloys to be tested using in-situ SEM equipment is suggested. The idea of the smaller specimens would aid in facilitating the quantification of the damage progression around second phase particles. Cracked particles or particles that experiences decohesion from the matrix would be easily identified and quantified. These numbers could be used as a comparison basis for the elongated and equiaxed particle damage mechanisms.
- The development of an etching/testing technique to attempt to plot the full field strain maps around the second phase particles for the unmodified and Sr-modified alloys would be useful tool to compare the effect of different shapes of second phase particles on the deformation process and strain localization.

- A comparison of the full field surface strain maps during compression loading and tensile loading. This was not possible throughout this thesis as the number of the prepared compression specimens was limited and a modification to the compression testing setup was needed to be adaptable with the CCD cameras for surface strain mapping results.
- Interrupted V-bend tests for the unmodified and Sr-modified alloy should be carried out to analyze the specimen through-thickness surface for cracked particles at each interruption. A plot of number of cracked particle versus the bend angle or mandrel displacement would be beneficial for a better understanding of damage progression in the unmodified and Sr-modified alloys.

## References

[1] August 2011. [Online]. Available: http://www.precisionenginetech.com.

[2] August 2011. [Online]. Available: http://www.dealernews.com.

[3] August 2011. [Online]. Available: http://www.delkron-mfg.com.

[4] M. D. Dighe, A. M. Gokhale and M. F. Horstemeyer, "Effect of Loading Condition and Stress State on Damage Evolution of Silicon Particles in an Al-Si-Mg-Base Cast Alloy," vol. 33A, 2002.

[5] D. Stefanescu, ASM Handbook: Volume 15: Casting, ASM, pp. 1622-1696, 1988.

[6] H. Xu, X. Jian, T. T. Meek and Q. Han, "Degassing of Molten Aluminum A356 Alloy using Ultrasonic Vibration," *Mater. Lett.,* vol. 58, pp. 3669-3673, 2004.

[7] J. Wang, S. He, B. Sun, Q. Guo and M. Nishio, "Grain Refinement of Al-Si Alloy (A356) by Melt Thermal Treatment," *J. Mater. Process. Technol.,* vol. 141, pp. 29-34, 2003.

[8] J. E. Gruzleski and B. Closset, "Structure and Properties of Hypoeutectic Al-Si-Mg Alloys Modified with Pure Strontium," *Metall. Trans.,* vol. 13, no. A, pp. 945-951, 1982.

[9] M. Dash and M. Makhlouf, "Effect of Key Alloys Elements on the Feeding Characteristics of Aluminum-Silicon Casting Alloys," *J. Light Met.,* vol. 1, pp. 251-265, 2001.

[10] Y. Z. Lu, Q. D. Wang, X. Q. Zeng, W. J. Ding and Y. P. Zhu, "Effects of Silicon on Microstructure, Fluidity, Mechanical Properties, and Fracture Behavior of Mg-6Al Alloy," *Mater. Sci. Technol.,* vol. 17, pp. 207-214, 2001.

[11] J. L. Murray and A. J. McAlister, "The Al-Si (Aluminum-Silicon) System," *J. Phase Equilib.,* vol. 5, no. 1, pp. 74-84, 1984.

[12] S. A. Kori, B. S. Murty and M. Chakraborty, "Development of an Efficient Grain Refiner for Al-7Si Alloy," *Mater. Sci. Eng.,* vol. 280, no. A, pp. 58-61, 2000.

[13] P. S. Mohanty and J. E. Gruzleski, "Grain Refinement Mechanism of Hypoeutectic Al-Si Alloys," *Acta. Mater.,* vol. 44, no. 9, pp. 3749-3760, 1996.

[14] D. G. McCartney, "Grain Refining of Aluminum and its Alloys using Inoculants," *Int. Mater. Rev.,* vol. 34, no. 5, pp. 247-260, 1989.

[15] H. T. Lu and L. C. Wang, "Grain Refining in A356 Alloys," *J. Chin Foundryman's Assoc.*, vol. 29, pp. 10-18, 1981.

[16] A. Pacz, "AWGOY". United Stated Patent US1387900, 16 Aug. pp. 1-2, 1921 .

[17] S. Nafisi and R. Ghomashchi, "Effects of Modifiication during Conventional and Semi-Solid Metal Processiong of A356 Al-Si Alloy," *Mater. Sci. Eng.*, vol. A, no. 415, pp. 273-285, 2006.

[18] D. Emadi, J. E. Gruzleski and J. M. Toguri, "The Effect of Na and Sr Modification on Surface Tension and Volumetric Shrinkage of A356 Alloy and Their Influence on Porosity Formation," *Metall. Trans. B*, vol. 24, pp. 1055-1063, December 1995.

[19] L. Liu, A. M. Samuel and F. H. Samuel, "Influence of Oxides on Porosity Formation in Sr-Treated Al-Si Casting Alloys," *J. Mater. Sci.*, vol. 38, pp. 1255-1267, 2003.

[20] S. A. Kori, M. S. Prabhudev and T. M. Chandrashekharaiah, "Studies on the Microstructure and Mechanical Properties of A356 Alloy with Minor Additions of Copper and Magnesium," *Trans. Indian Inst. Met.*, vol. 62, no. 4-5, pp. 353-356, 2009.

[21] G. Birsan, "Controlled Diffusion Solidification for Tilt Pouring Casting Process," Hamilton, McMaster University - MASc. Thesis, pp. 21-36, 2009.

[22] J. G. Conley, J. Huang, J. Asada and K. Akiba, "Modeling the Effects of Cooling Rate, Hydrogen Content, Grain Refiner and Modifier on Microporosity Formation in Al A356 Alloys," *Mater. Sci. Eng.*, vol. 285, no. A, pp. 49-55, 2000.

[23] L. Y. Zhang, Y. Jiang, Z. Ma, S. F. Shan, Y. Z. Jia, C. Z. Fan and W. K. Wang, "Effect of Cooling Rate on Solidified Microstructure and Mechanical Properties of Aluminum A356 Alloy," *J. Mater. Process. Technol*, vol. 207, pp. 107-111, 2008.

[24] Q. G. Wang, "Plastic Deformation Behavior of Aluminum Casting Alloys A356/357," *Metall. Mater. Trans. ,* vol. 35, no. A, pp. 2707-2718, 2004.

[25] D. Emadi, L. V. Whiting, M. Sahoo, J. H. Sokolowski, P. Burke and M. Hart, "Optimal Heat Treatment of A356.2 Alloy," in *Light Metals - TMS (The Minerals, Metals & Materials Society)*, 2003.

[26] J. F. H. Paz, "Heat Treatment and Precipitation in A356 Aluminum Alloy," McGill University - Ph.D Thesis - pp. 4-21, 2003 .

[27] L. Pedersen and L. Arnberg, "The Effect of Solution Heat Treatment and Quenching Rates on Mechanical Properties and Microstructures in Al Si Mg Foundry Alloys,"

*Metall. Mater. Trans.*, vol. 32, no. A, pp. 525-532, 2001.

[28] C. J. Davidson, J. R. Griffiths and A. S. Machin, "The Effect of Solution Heat-Treatment Time on the Fatigue Properties of an AL-Si-Mg Casting Alloy," *Fatigue Fract. Eng. Mater. Struct.*, vol. 25, pp. 223-230, 2002.

[29] "Standard Practice for Heat Treatment of Aluminum-Alloy Castings from All Processes," ASTM Standards - ASTM B917/B917M-08, 2008.

[30] S. Shivkumar, S. Ricci, C. Keller and D. Apelian, "Effect of Solution Treatment Parameters on Tensile Properties of Cast Aluminum Alloys," *J. Heat. Treat.*, vol. 8, pp. 63-70, 1990.

[31] M. H. Mülazımoğlu, "Electrical Conductivity Studies of Cast Al-Si and Al-Si-Mg Alloys," McGill University - Ph.D Thesis, pp. 163-201, 1988 .

[32] D. S. Thompson, B. S. Subramanya and S. A. Levy, "Quench Rate Effects in Al-Zn-Mg-Cu Alloys," *Metall. Trans.*, vol. 2, pp. 1149-1160, 1971.

[33] J. T. Staley, "Quench Factor Analysis of Aluminum Alloys," *Mater. Sci. Technol.*, vol. 3, pp. 923-935, 1987.

[34] J. Manickaraj, G. Liu and S. Shankar, "Effect of Incubation Coupled with Artifical Aging in T6 Heat Treatment of A356.2 Aluminum Casting Alloy," *Int. J. Metalcast.*, vol. 5, no. 4, pp. 17-36, 2011.

[35] W. F. Miao and D. E. Laughlin, "A Differential Scanning Calorimetry Study of Aluminum Alloy 6111 with Different Pre-Aging Treatments," *J. Mater. Sci. Lett.*, vol. 19, pp. 201-203, 2000.

[36] Hernandez-Paz, F. Paray, J. E. Gruzleski and D. Emadi, "Natural Aging and Heat Treatment of A356 Aluminum Alloy," in *Metalcasting Congress*, Rosemont, 2004.

[37] M. F. Horstemeyer, "Damage Influence on Baushinger Effect of a Cast A356 Aluminum Alloy," *Scr. Mater.*, vol. 39, no. 11, pp. 1491-1495, 1998.

[38] S. G. Shabestari and F. Shahri, "Influence of Modification, Solidification Conditions and Heat Treatment on the Microstructure and Mechanical Properties on A356 Aluminum Alloy," *J. Mater. Sci*, vol. 39, pp. 2023-2032, 2004.

[39] A. M. Gokhale and S. Yang, "Application of Image Processing for Simulation of Mechanical Response of Multi-Length Scale Microstructures of Engineering Alloys," *Metall. Mater. Trans.* , vol. 30, no. A, pp. 2369-2381, 1999.

[40] P. A. Friedman and S. G. Luckey, "Failure of Al-Mg-Si Alloys in Bending," *Pract. Fail. Anal.*, vol. 2, no. 1, pp. 33-42, 2002.

[41] Z. Sun, J. S. Lyons and S. McNeil, "Measuring Microscopic Deformations with Digital Image Correlation," *Opt. Lasers Eng.*, vol. 27, pp. 409-428, 1997.

[42] M. Sutton, S. McNeil, J. Helm, Y. Chao and P. Rastogi, "Advances in Two-Dimesional and Three-Dimensional Computer Vision," in *Photomechanics*, Springer, 2000, pp. 323-372.

[43] J. Quinta Da Fonseca, P. M. Mummery and P. J. Withers, "Full-Field Strain Mapping by Optical Correlation of Micrographs Acquired during Deformation," *J. Microsc. Sci.*, vol. 218, no. 1, pp. 9-21, 2005.

[44] X. Duan, M. Jain, M. Bruhis and D. S. Wilkinson, "Experimental and Numerical Study of Intense Shear Banding for Al-Alloy under Uniaxial Tension," *Adv. Mater. Res.*, vol. 6, pp. 737-744, 2005.

[45] B. Han, D. Post and P. Ifju, "Moire Interferometry for Engineering Mechanics: Current Practices and Future Developments," *J. Strain Anal. Eng. Des.*, vol. 36, no. 1, pp. 101-117, 2001.

[46] A. McDonach, J. McKelvie, P. MacKenzie and C. A. Walker, "Improved Moire Interferometry and Applications in Fracture Mechanics, Residual Stress and Damaged Composites," *Exp. Tech.*, vol. 7, no. 6, pp. 20-24, 1983.

[47] D. Post, "The Moire Grid-Analyzer Method for Strain Analysis," *Exp. Mech.*, pp. 368-377, 1965.

[48] B. Han and Y. Guo, "Photomechanics Tools as Applied to Electronic Packaging Product Development," *Exp./Numer. Mech. Electron. Packag.*, vol. 1, pp. 11-15, 1997.

[49] B. Han, "Deformation Mechanism of Two-Phase Solder Column Interconnections under Highly Accelerated Thermal Cycling Condition: An Experimental Study," *Trans. ASME, Electronic Packaging*, vol. 119, pp. 189-196, 1997.

[50] B. Schroeter and D. McDowell, "Measurement of Deformation Felds in Polycrystalline OFHC Copper," *International Journal of Plasticity*, vol. 19, pp. 1355-1376, 2003.

[51] V. Sedlacek and V. Kafka, "The Inhomogeneity of Plastic Deformation," *Czech. J. Phys*, vol. 35, pp. 346-350, 1985.

[52] I. Czinege and T. Reti, "Determination of Local Deformation in Cold Formed Products by a Measurement of teh Geometric Characteristics of the Crystallites," in *Int. Mach. Tool Design and Research Conference*, 1977.

[53] S. Zaefferer, J. C. Kuo, Z. Zhao, M. Winning and D. Raabe, "On the Influence of the Grain Boundary Misorientation of the Plastic Deformation of Aluminum Bicrystals," *Acta Mater.*, vol. 51, pp. 4719-4735, 2003.

[54] C. Efstathiou, H. Sehitoglu and J. Lambros, "Multiscale Strain Measurements of Plastically Deforming Polycrstalline Titanium: Role of Deformation Heterogeneities," *Int. J. Plast.*, vol. 26, pp. 93-106, 2010.

[55] N. Zhang and W. Tong, "An Experimental Study on Grain Deformation and Interactions in an Al-0.5%Mg Multicrystal," *Int. J. Plast.*, vol. 20, pp. 523-542, 2004.

[56] D. Raabe, M. Sachtleber, Z. Zhao, F. Roters and S. Zaefferer, "Micromechanical and Macromechanical Effects in Grain Scale Polycrystal Plasticity Experimentation and Simulation," *Acta. Mater.*, vol. 49, pp. 3433-3441, 2001.

[57] M. Sachtelber, Z. Zhao and D. Raabe, "Experimental Investigation of Plastic Grain Interaction," *Mater. Sci. Eng.*, vol. 336, no. A, pp. 81-87, 2002.

[58] T. Pardoen and J. W. Hutchinson, "An Extended Model for Void Growth and Coalescence," *J. Mech. Phys. Solids*, vol. 48, pp. 2467-2512, 2000.

[59] J. Gurland and J. Plateau, "The Mechanism of Ductile Rupture of Metals Containing Inclusions," *ASM Quarterly Transactions*, vol. 56, no. 3, pp. 442-454, 1963.

[60] D. Dispinar, S. Akhtar, A. Nordmark, M. D. Siabatino and L. Arnberg, "Degassing, Hydrogen and Porosity Phenomena in A356," *Mater. Sci. Eng.*, vol. 527, no. A, pp. 3719-3725, 2010.

[61] "Standard Test Methods for Tension Testing of Metallic Materials," ASTM Standards - ASTM E8/E8M, 2009.

[62] R. K. Roy and S. Das, "New Combination of Polishing and Etching Technique for Revealing Grain Structure of an Annealed Aluminum (AA1235) Alloy," *J. Mater. Sci. Eng*, vol. 41, pp. 289-292, 2006.

[63] December 2011. [Online]. Available: http://rsbweb.nih.gov/ij/.

[64] G. O. M. Techniques, March 2012. [Online]. Available: http://www.gom.com/3d-software/argus-software.html.

[65] G. O. M. Techniques, March 2012. [Online]. Available: http://www.gom.com/3d-software/aramis-software.html.

[66] J. Lemaitre and R. Desmorat, Engineering Damage Mechanics: Ductile, Creep, Fatigue and Brittle Failures, Springer, 2005.

[67] J. Lemaitre, "How to Use Damage Mechanics," *Nucl. Eng. Des.*, vol. 80, pp. 233-245, 1980.

[68] C. Wang, G. Kinzel and T. Altan, "Mathematical Modeling of Plane-Strain Bending of Sheet and Plate," *J. Mater. Process. Technol.*, vol. 39, pp. 279-304, 1993.

[69] S. Shivkumar, L. Wang and D. Apelian , "Molten Metal Processing of Advanced Casting Aluminum Alloys," *J. Met.*, vol. 43, no. 1, pp. 26-32, 1991.

[70] H. R. Lashgari, M. Emamy, A. Razaghian and A. A. Najimi, "The Effect of Strontium on the Microstructure, Porosity and Tensile Properties of A356-10%B4C Cast Composite," *Mater. Sci. Eng., A*, vol. 517, pp. 170-179, 2009.

[71] C. M. Dinnis, M. O. Otte, A. K. Dahle and J. A. Taylor, "The Influence of Strontium on Porosity Formation in Al-Si Alloys," *Metall. Mater. Trans. A*, vol. 35, pp. 3531-3541, 2004.

[72] D. L. Lloyd, "Aspects of Fracture in Particulate Reinforced Metal Matrix Composites," *Acta. Metall. Mater.*, vol. 39, no. 1, pp. 59-71, 1991.